ROMA TRE
UNIVERSITÀ DEGLI STUDI

Dipartimento di Fisica "E. Amaldi"

Università degli Studi Roma Tre

Dottorato di Ricerca in Fisica - XVIII ciclo

MICROWAVE COMPLEX RESPONSE IN SUPERCONDUCTING THIN FILMS IN MAGNETIC FIELDS

Nicola Pompeo

Chairperson of the Ph.D. School

prof. Orlando Ragnisco

Supervisor

prof. Enrico Silva

A.A. 2004 - 2005

The most beautiful and deepest experience a man can have is the sense of the mysterious. It is the underlying principle of religion as well as of all serious endeavour in art and science.

"A. Einstein" [1]

Acknowledgements

I would like to warmly record my obligation to all those who contributed to this study by providing the samples investigated in this thesis: A. M. Cucolo and M. Boffa for $SmBa_2Cu_3O_{7-\delta}$ and $Bi_2Sr_2CaCu_2O_{8+x}$ samples, C. Camerlingo, G. Celentano and L. Méchin for $YBa_2Cu_3O_{7-\delta}$ samples, H. Schneidewind for $Tl_2Ba_2CaCu_2O_{8+x}$ samples. In addition, I thank F. Marinilli for his help in the mechanical design and for the careful making of the resonator, M. Ausloos and R. Cloots for their warm hospitality in the Liège University, L. Muzzi for his constant assistance, M. Antonioli for his kind help, A. Alegi for her kind and careful work. Stimulating discussions with R. Fastampa, M. Giura, R. Marcon and S. Sarti are sincerely acknowledged. I am profoundly grateful to E. Silva for his constant and precious guidance, including the helpful discussions concerning both experimental and theoretical issues.

Last but not least, I do thank with love my parents and my friends for their support and encouragement.

Work of chapter 4 has been partially supported by Italian MIUR under the FIRB project "Strutture semiconduttore/superconduttore per l'elettronica integrata".

Contents

List of Figures

List of Tables

List of Symbols

Bold letters denote vector quantities.

Δ	superconducting gap
e	electron charge
em	electromagnetic
ε	electrical permittivity
η	vortex viscosity
Φ_0	magnetic flux quantum
G	geometric factor
H_{c1}	lower critical field
H_{c2}	upper critical field
$\hbar$	Planck constant
$\Im$	imaginary part
k_B	Boltzmann constant
k_p	pinning coefficient (Labusch parameter)
κ	Ginzburg-Landau parameter
λ	(London) penetration depth
m	electron mass
μ	magnetic permeability
ν_0	resonant frequency
ν_p	(de)pinning frequency
ψ	superconductor order parameter
Q_L	loaded quality factor
Q_U	unloaded quality factor
QP	quasiparticle
$\tilde{\rho}$	complex resistivity
ρ_v	vortex resistivity
R	surface resistance
R'	effective surface resistance
$\Re$	real part

$\tilde{\sigma}$	complex conductivity
σ_n	normal fluid conductivity
σ_s	superfluid conductivity
τ	(quasiparticle) relaxation time
T_c	critical temperature
t_s	superconducting film thickness
ξ	coherence length
X	surface reactance
X'	effective surface reactance
x_n	normal fluid fraction
x_s	superfluid fraction
Z	surface impedance
Z'	effective surface impedance

Introduction

The microwave response of High-T_c superconductors (HTCS) provides important information about both fundamental physics and technological issues. The time-varying nature of the stimulus allows for the simultaneous probing of both the types of charge carriers existing in a superconducting system: quasiparticles (low energy excitations) and Cooper pairs, the former being not detectable with continuous current measurements. Moreover, in the microwave frequency range these two contributions can be comparable, while at the same time the excitation energy scale is usually well below the superconducting gap, thus avoiding the disruption of the superfluid condensate. An additional experimental degree of freedom is obtained by applying a static magnetic field: in this way the phenomenology is enriched by the pair-breaking effect on the Cooper pairs and by the appearance (in the mixed state) of the fluxon system with the corresponding dynamics. The fluxon dynamics, in principle extraordinarily complex, can be often simplified and reduced to intrinsic properties by resorting to sufficiently high microwave frequencies.

This thesis summarizes a three-year experimental research consisting in the measurement and study of the microwave electrodynamic response of various HTCS materials having different degrees of anisotropy: $SmBa_2Cu_3O_{7-\delta}$, $YBa_2Cu_3O_{7-\delta}$, $Bi_2Sr_2CaCu_2O_{8+x}$ and $Tl_2Ba_2CaCu_2O_{8+x}$. All the samples were epitaxial thin films grown on suitable substrates. In this situation the electromagnetic field penetration covers an essential role, interacting both with the bulk of the superconducting film and with the underlying substrate. The resulting electrodynamics has been studied both theoretically and experimentally.

One of the most sensitive experimental techniques at microwave frequencies involves the use of resonators. During this thesis an high frequency dielectric resonator has been designed, developed and put in operation. Part of the measurements here presented have been taken with the new setup.

The main experimental results deal with the response of the materials under investigation to a moderate applied magnetic field ($\mu_0 H \leq 0.8$ T). For all of them it is found that a description in terms of fluxon dynamic models

only is insufficient. The "123" compounds find an excellent description within mean field models incorporating both fluxon dynamics (with no evidence for flux creep) and the essential contribution of low lying excitations. Fundamental parameters, such as the quasiparticle scattering time below T_c, the temperature-dependent fluxon viscosity and extrinsic parameters, such as the depinning frequency, are estimated. On the other hand, in $Tl_2Ba_2CaCu_2O_{8+x}$ the data exhibit clear scaling behaviour, indicating a leading role of an underlying vortex matter transformation in the vortex dynamics. Lastly, in the very low field region, the high sensitivity of the dielectric resonator allowed to detect effects of Josephson junctions dynamics.

The outline of this thesis is as follows. Chapter 1 presents a brief summary of the main phenomenology of superconductivity, with particular attention to electrodynamic models in the microwave range. Chapter 2 is devoted to the mixed state. Main issues of the fluxon dynamics in the Abrikosov state and in other fluxon configurations are depicted. In particular, the interaction between fluxons and quasiparticles is recalled and a general mean field model is described. Chapter 3 describes the technique used for the measurement of the microwave response of superconductors and deals with the technical part of the work carried on during this thesis: the design, development and setup of a dielectric resonator. Chapter 4 focuses on substrate contribution to the electromagnetic field penetration into superconducting thin films. Lastly, in chapter 5 we present and discuss the results in the measurements of the response to the applied magnetic field of the various cuprates investigated.

Chapter 1

Superconductivity

In the first part of this chapter conventional superconductivity will be introduced, with its main phenomena and interpretative theories, in order to give a basic background for the subsequent discussion. In particular I will focus on electrodynamic models in the microwave range, useful for the interpretation of the measurements performed in this thesis. Afterwards high critical temperature superconductors will be introduced, firstly by briefly mentioning their main open issues and secondly by highlighting a few peculiar properties, related to the existence of nodal quasiparticles, relevant for my microwave study. The effects of a static magnetic field will be considered in chapter 2.

1.1 Main phenomenology

The phenomenon of superconductivity was discovered in 1911 by Kamerling Onnes [2], who measured a zero dc electrical resistivity in mercury below a characteristic temperature (figure 1.1), the so called critical temperature T_c.
Afterwards, many other metals and metallic alloys were found to show an analogous behavior, with Nb_3Ge having the highest T_c=23 K until the discovery of the so called high T_c superconductors (HTCS) (see section 1.5), having typical T_c greater than the liquid nitrogen temperature (figure 1.2).
The other fundamental property of superconductors is the perfect (in the bulk case) diamagnetism, discovered by Meissner and Ochsenfeld [3] in 1933. The Meissner effect, giving $\mathbf{B} = \mathbf{0}$ inside the superconductor volume (figure 1.3), distinguishes a superconductor from a perfect conductor, in which $\dot{\mathbf{B}} = \mathbf{0}$ (the dot represents the time-derivative).
In ideal superconductors, the condition $\mathbf{B} = \mathbf{0}$ is independent from the magnetic and thermal history: this insures that the superconducting state is a true thermodynamic phase. Therefore one can define the so-called condensation en-

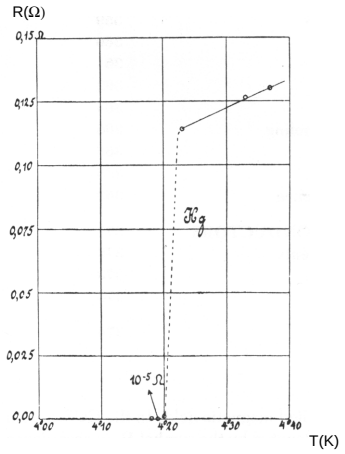

Figure 1.1: Resistive transition of mercury, taken from [2].

ergy as the Gibbs free energy gain (per unit volume) of the superconducting state with respect to the normal state at zero field, $\Delta g = g_n - g_s > 0$. By applying an external magnetic field H, the Meissner effect builds up and the superconductor energy density increases by an amount $\frac{1}{2}\mu_0 \mathbf{H} \cdot \mathbf{M}$, where $\mathbf{M}$ is the magnetization of the sample. It therefore exists a threshold field, the so called thermodynamical critical field H_c, above which the material minimizes the total energy by reverting to the normal state. The temperature dependence of H_c is empirically described as $H_c(T) = H_c(0)(1 - (T/T_c))^2$, allowing to represent a phase diagram in the plane (T, H) as in the left panel of figure 1.4. Analogously, the ability of a superconductor to carry resistanceless continuous supercurrents is limited to current densities $J < J_{dp}$, where the so called depairing current density J_{dp} correspond to a density of the kinetic energy of charge carriers equal to the condensation term Δg.

With respect to the above description, the so-called type-II superconductors present a more complex behavior in magnetic field. They are characterized by the existence of two (lower and upper) critical fields $H_{c1} < H_{c2}$. In these materials, the Meissner state exists only for $H < H_{c1}$, while the transition to the normal state occurs for $H > H_{c2}$[1]. In the interval $H_{c1} < H < H_{c2}$ the material is in the so called mixed state (subject of chapter 2), in which there is a partial penetration of B in the sample in the form of quantized flux tubes (also called fluxons). Phase diagrams in the H-T plane and magnetization curves for type I and II superconductivity are represented in figure 1.4.
From now on I will consider only type II superconductors, since all the materials studied in this thesis belong to this category.

[1]Not considering other critical fields such as the surface critical field H_{c3}.

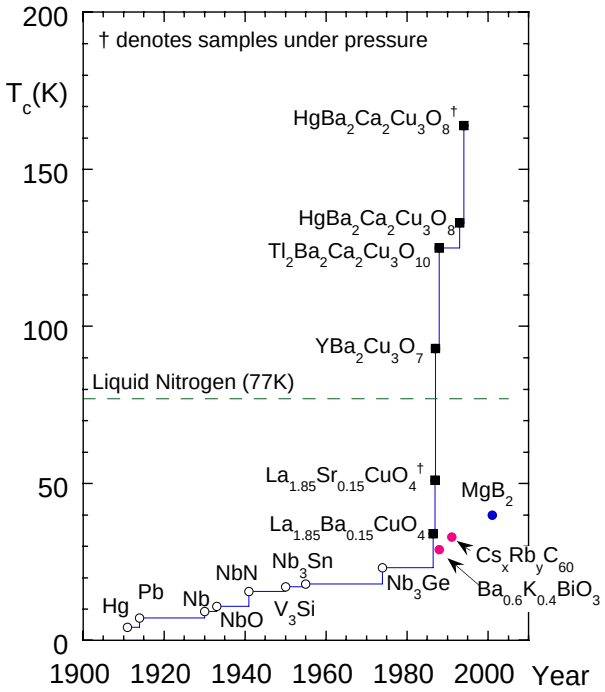

Figure 1.2: "Evolution" of critical temperatures in time. Circles: non oxide superconductors; squares: oxide superconductors.

The experimental physics of superconductors has brought through time to the proposal of various interpretative theories. In the following a very partial survey of such theories is presented in order to introduce essential concepts useful for this thesis.

1.2 Ginzburg-Landau theory

The superconductor-normal thermodynamic phase transition is a second order transition, as suggested by thermal measurements across T_c (in zero-field), which yield zero latent heat and a discontinuous specific heat. This allowed Ginzburg and Landau (GL) to extend the Landau theory for second order phase transitions [4] to the superconductor transition. The GL theory [5] describes the normal-superconducting transition by expressing the Gibbs free energy density g as a function of a complex order parameter ψ. The thermodynamical equilibrium state is found by minimizing the energy G with respect

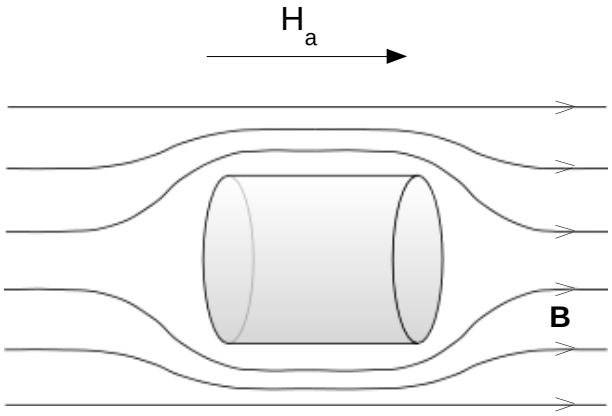

Figure 1.3: Meissner effect: flux expulsion in a superconductor. Flux lines represent **B**.

to ψ (neglecting any thermal fluctuation contribution with respect to mean values): this gives

$$\begin{cases} \psi = 0, & T > T_c \\ \psi \neq 0, & T < T_c \end{cases}$$

By following a phenomenological approach, including the effects of an externally applied magnetic field $\mathbf{H_0}$, allowing a spatially varying $\psi(\mathbf{r})$ and including the energy term related to $|\nabla\psi|$ (written in order to ensure gauge invariance), g is expanded as a function of ψ so that, retaining the low order terms, one has [6, 7, 8]:

$$g = g_n + \frac{1}{V}\int_V d^3\mathbf{r}\left\{\alpha|\psi(\mathbf{r})|^2 + \frac{\beta}{2}|\psi(\mathbf{r})|^4 + \right.$$
$$\left. + \frac{\hbar^2}{2m^*}\left|\left(\nabla - \frac{ie^*}{\hbar}\mathbf{A}(\mathbf{r})\right)\psi(\mathbf{r})\right|^2 + \left(\frac{B^2(\mathbf{r})}{2\mu_0} - \mu_0\mathbf{M}(\mathbf{r})\cdot\mathbf{H_0}\right)\right\} \qquad (1.2.1)$$

where e^* and m^* can be set respectively equal to $2e$ and $2m$ (with e and m electron charge and mass), V is the sample volume, $\mathbf{B} = \nabla \times \mathbf{A}$ is the microscopic induction field, $\mathbf{M}$ the magnetization and $\mathbf{A}$ the vector potential. α and β are phenomenological terms for which, in the vicinity of T_c, one has $\alpha = -\alpha_0(1 - T/T_c)$ and $\beta(T) = \beta_0$ (with $\alpha_0 > 0$, $\beta_0 > 0$). By minimizing the energy per unit volume g with respect to $\psi(\mathbf{r}) = |\psi(\mathbf{r})|e^{i\phi(\mathbf{r})}$ and $\mathbf{A}(\mathbf{r})$, the so called GL differential equations are obtained:

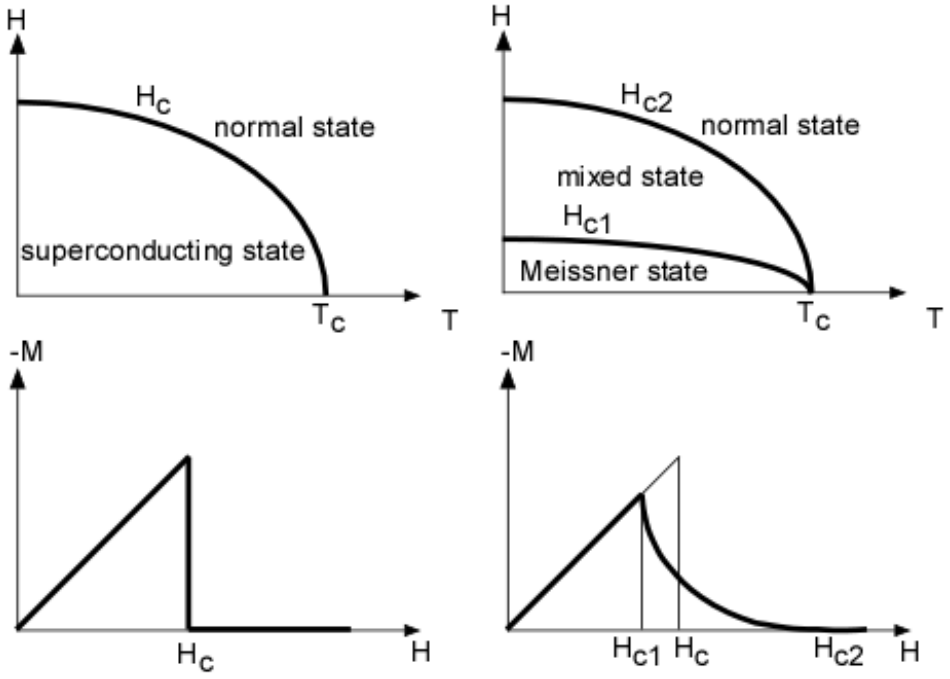

Figure 1.4: Phase diagrams (*upper panels*) and magnetization curves (*lower panels*) for type I (*left panels*) and II (*right panels*) superconductivity.

$$\psi(\mathbf{r})(\alpha + \beta|\psi(\mathbf{r})|^2) + \frac{\hbar^2}{2m^*}\left|\left(\nabla - \frac{ie^*}{\hbar}\mathbf{A}\right)\psi(\mathbf{r})\right|^2 = 0 \tag{1.2.2}$$

$$\mathbf{J_s}(\mathbf{r}) = \frac{e^*}{m^*}\left[\hbar\nabla\phi(\mathbf{r}) - e^*\mathbf{A}(\mathbf{r})\right]|\psi(\mathbf{r})|^2 \tag{1.2.3}$$

having used $\mathbf{J_s} = \nabla \times \mathbf{B}/\mu_0$ for the supercurrent $\mathbf{J}_s$. By considering specific sample geometries, the above GL differential equations can be solved and the equilibrium $\psi(\mathbf{r})$ and $\mathbf{B}(\mathbf{r})$ simultaneously determined.

I now introduce two fundamental characteristic lengths: the GL coherence length ξ_{GL} and the GL penetration depth λ_{GL}, which define the length scales for the space variations of $\psi(\mathbf{r})$ and $\mathbf{B}(\mathbf{r})$, respectively. Their expression can be derived considering a simple unidimensional geometry with a planar interface separating two semi-infinite spaces, occupied by a normal material and a superconductor. One obtains [6, 8]:

$$\xi_{GL}(T) = \sqrt{\frac{\hbar^2}{2m^*|\alpha(T)|}} \tag{1.2.4}$$

$$\lambda_{GL}(T) = \sqrt{\frac{m^*}{\mu_0 e^{*2}|\psi_\infty(T)|^2}} \tag{1.2.5}$$

where $\psi_\infty = \sqrt{|\alpha|/\beta}$ represents the bulk limit value of $\psi(\mathbf{r})$.

Once defined these quantities, one can comment on the GL limits of validity resorting to Gor'kov work [9], who derived the GL theory as a limiting case of the BCS microscopic theory (outlined in section 1.4). It is required the local electrodynamic limit, with slowly varying $\psi(\mathbf{r})$ and $\mathbf{B}(\mathbf{r})$ with respect to the microscopic coherence length ξ_0. Since it can be shown that $\xi_{GL} \cong \xi_0/\sqrt{1-T/T_c}$ (in the clean limit $\xi_0 \ll l$, being l the electronic mean free path), these requirements imply $T \lesssim T_c$ and $\lambda_{GL} > \xi_0$. When these conditions are met, it can be shown that $|\psi|^2$ can be interpreted as the density of superconducting Cooper pairs (see section 1.4) having mass m^* and charge e^*.

Being interested in electrodynamic quantities, one now derives, within the London gauge $\nabla\phi = 0$, the expressions for the electric field $\mathbf{E} = -d\mathbf{A}/dt$ and the magnetic induction $\mathbf{B} = \nabla \times \mathbf{A}$. One first isolates in the second member of equation (1.2.3) the vector potential $\mathbf{A}$. By applying to both members the time derivative d/dt or the curl operator $(\nabla\times)$, one obtains the well-known London equations:

$$\mathbf{E} = \frac{d}{dt}\left(\frac{e^{*2}}{m^*|\psi|^2}\mathbf{J_s}\right) \tag{1.2.6}$$

$$\mathbf{B} = -\nabla\left(\frac{e^{*2}}{m^*|\psi|^2}\mathbf{J_s}\right) \tag{1.2.7}$$

The first equation is readily recognized as a free accelerating current under the effect of an electric field, corresponding to the idea of charge carriers free from scattering processes. Moreover, by setting a constant $\psi = \psi_\infty$ and using the Maxwell equation $\nabla \times \mathbf{B} = \mu_0 \mathbf{J}_s$ in the second equation, one easily obtains $\nabla^2\mathbf{B} = \mathbf{B}/\lambda_{GL}^2$. This equation gives a magnetic induction $\mathbf{B}$ exponentially screened along a length scale λ_{GL}, giving zero intensity in the bulk, as the Meissner effect requires. An identical space variation holds for the supercurrent $\mathbf{J}_s$, meaning that these diamagnetic currents flow in a surface sheet of the thickness of the order of λ_{GL}.

1.3 Two fluid model

It should be noted that, historically, equations (1.2.6) and (1.2.7) were proposed by the London brothers [10] by considering a resistanceless flowing superfluid of charge carriers having charge e, mass m and density n_s, and imposing $\mathbf{B} = \mathbf{0}$ in the bulk, as indicated by the experimental Meissner effect. They obtained the field penetration length given by the so-called "London penetration depth":

$$\lambda_L = \sqrt{\frac{m}{\mu_0 e^2 n_s^2}} \tag{1.3.1}$$

Indeed, it can be seen that $\lambda_{GL} = \lambda_L$, paying attention to the meaning of the two sets of quantities for the density, mass and charge of the charge-carriers: $\{n_s,\ m,\ e\}$ and $\{|\psi_\infty|^2,\ m^*,\ e^*\}$. The former set relates to single "superelectrons", while the latter considers Cooper pairs with doubled masses and charges, but with a density $|\psi_\infty|^2$ halved by definition with respect to n_s. The expression of the penetration depth is therefore identical using either of the two sets.

Coming back to the first London equation (1.2.6), it is seen that in a static regime superconducting currents $\mathbf{J}_s$ can flow in absence of an electric field $\mathbf{E}$, which in effect corresponds to zero dc resistance. On the other hand, this picture requires an additional component whenever alternating $\mathbf{E}$ fields are considered, since in this case a dissipation contribution is always experimentally detected. The simple two-fluid model proposed by Gorter and Casimir [11] assumes that, beside the superfluid, a second "normal" fluid takes part to the electrical conduction process, experimenting usual scattering processes. The normal fluid, within a Drude model and using $e^{\mathrm{i}\omega t}$ time varying quantities, has the following conductivity:

$$\sigma_n = \frac{n_n e^2 \tau_n}{m} \frac{1}{1 + \mathrm{i}\omega\tau_n} \tag{1.3.2}$$

where n_n, τ are the normal fluid volume density and relaxation time, respectively. On the other hand, the superfluid conductivity σ_s is:

$$\sigma_s = \frac{\pi}{2} \frac{n_s e_s^2}{m} \delta(\omega) - \mathrm{i} \frac{n_s e_s^2}{\omega m} \tag{1.3.3}$$

where the imaginary component corresponds to the first London equation while the delta function in the real part accounts for the infinite dc conductivity and can be obtained from spectral weight conservation [6]. Since in the two-fluid approach the total current density is given by $\mathbf{J} = \mathbf{J}_n + \mathbf{J}_s$, being $\mathbf{J}_n = \sigma_n \mathbf{E}$

the current density due to the normal fluid, the total complex conductivity for finite frequencies is then:

$$\tilde{\sigma}(\omega) = \sigma_n(\omega) + \sigma_s(\omega) = \frac{ne^2}{m\omega}\left(x_n \frac{\omega\tau}{1+\mathrm{i}\omega\tau} - \mathrm{i}x_s\right) \tag{1.3.4}$$

where $x_n = n_n/n$ and $x_s = n_s/n$ are the fractional fluid densities, being n the electron density in the normal state. For the sum rule argument, the normalization $x_n(T)+x_s(T) = 1$ holds. In most conventional superconductors an expression of the form $x_s(T) = 1 - (T/T_c)^\alpha$ describes quite well the data, with $\alpha > 1$. In HTCS in many cases one can describe reasonably well the data with $\alpha = 2$, at least for temperatures not too close to T_c [12].

Two points are worth being stressed. First, equation (1.3.4) contains an essential feature of the electrodynamics of superconductors: the resistanceless regime is confined to dc regimes only, while alternating fields give always dissipation. Second, the two-fluid model is valid in the local limit (the applicability of which, for the superfluid, characterizes the so-called London superconductors).

In the next section it will be shown how the two-fluid model can be derived within the framework of the BCS microscopic theory. This fact, together with its simplicity, makes it widely used in the interpretation and modelling of the experimental data.

1.4 The BCS microscopic theory

The theory developed by Bardeen, Cooper and Schrieffer (BCS) in 1957 [13] was the first capable of giving a microscopic explanation of how superconductivity emerged in traditional superconductors. Its great success in explaining experimental results, the insight gained by its study in time and its ease to incorporate significant generalizations led to its application to many categories of superconducting materials including high temperature superconductors, in spite of the objections of both theoretical and experimental nature which arises when these materials are considered. The founding concept is that bound pairs of electrons (the so called Cooper pairs) [14], having a coherence length from now on indicated with ξ_0, can form over a ground Fermi liquid state if an attractive interaction between them exists, regardless its weakness, in addition to the regular screened Coulomb repulsion. Taking into account zero net momentum (for minimal energy) and the antisymmetry of the overall paired wave function, electron pairs are expected to have (momentum, spin) values equal to ($\mathbf{k}$,$\uparrow$) and ($-\mathbf{k}$,$\downarrow$) in the singlet case (with $\mathbf{k}$ the momentum of a plane wave (ideal case) and $\uparrow/\downarrow$ denoting the two possible states of fermion spins ς). In

traditional superconductors the origin of the attractive interaction was found in electron-phonon coupling: the local polarization of the crystal lattice due to the vicinity of an electron lasts beyond the transit of the electron (retarded interaction), giving rise to a local positive charge capable of attracting a second electron. This idea was suggested and confirmed by the observation of the isotope effect, consisting in the proportionality of T_c and H_c to $M^{-1/2}$ for mass-M isotopes of the same element [15, 16]. It is worth mentioning that the BCS theory is not linked to the specific nature of the electron-boson mechanism originating the electron effective attraction, thus being applicable with different "glueing" bosons.

For this thesis the study of the excited states above the superconducting ground state are of specific interest. One therefore proceeds by recalling the study of the relevant hamiltonian. Within the second quantization formalism and denoting $c^*_{\mathbf{k}\varsigma}$ and $c_{\mathbf{k}\varsigma}$ the fermion creation and annihilation operators for a fermion quasiparticle of crystal momentum $\mathbf{k}$ and spin ς, respectively, the hamiltonian can be written [6] as follows:

$$H = \sum_{\mathbf{k}\varsigma} (\xi_{\mathbf{k}} + \mu) n_{\mathbf{k}\varsigma} + \sum_{\mathbf{kl}} V_{\mathbf{kl}} c^*_{\mathbf{k}\uparrow} c^*_{-\mathbf{k}\downarrow} c_{-\mathbf{l}\downarrow} c_{\mathbf{l}\uparrow} \tag{1.4.1}$$

where $n_{\mathbf{k}\varsigma} = c^*_{\mathbf{k}\varsigma} c_{\mathbf{k}\varsigma}$ is the number operator, $\xi_{\mathbf{k}}$ is the kinetic energy with respect to the chemical potential μ, $V_{\mathbf{kl}}$ are the matrix elements of the interaction potential. One looks for a ground state of the above pairing hamiltonian having the BCS form:

$$|\psi_{BCS}\rangle = \prod_{\mathbf{k}} \left(u_{\mathbf{k}} + v_{\mathbf{k}} c^*_{\mathbf{k}\uparrow} c^*_{-\mathbf{k}\downarrow}\right) |\psi_0\rangle \tag{1.4.2}$$

where $|\psi_0\rangle$ represents the vacuum state, and with $u_{\mathbf{k}}$ and $v_{\mathbf{k}}$, normalized to $|v_{\mathbf{k}}|^2 + |u_{\mathbf{k}}|^2 = 1$, to be determined. To do so, one can solve the above hamiltonian following a mean-field approach, by writing $c_{-\mathbf{k}\downarrow} c_{\mathbf{k}\uparrow} = \langle c_{-\mathbf{k}\downarrow} c_{\mathbf{k}\uparrow} \rangle + (c_{-\mathbf{k}\downarrow} c_{\mathbf{k}\uparrow} - \langle c_{-\mathbf{k}\downarrow} c_{\mathbf{k}\uparrow} \rangle)$ (where $\langle\rangle$ means expectation value) and afterwards neglecting higher order terms in the fluctuation contribution written in round brackets. The obtained hamiltonian can be diagonalized with the following transformation

$$\begin{aligned} c_{\mathbf{k}\uparrow} &= u^*_{\mathbf{k}} \gamma_{\mathbf{k}0} + v_{\mathbf{k}} \gamma^*_{\mathbf{k}1} \\ c^*_{-\mathbf{k}\downarrow} &= -v^*_{\mathbf{k}} \gamma_{\mathbf{k}0} + u_{\mathbf{k}} \gamma^*_{\mathbf{k}1} \end{aligned} \tag{1.4.3}$$

by properly choosing $u_{\mathbf{k}}$ and $v_{\mathbf{k}}$. One gets:

$$|v_{\mathbf{k}}|^2 = 1 - |u_{\mathbf{k}}|^2 = \frac{1}{2}\left(1 - \frac{\xi_{\mathbf{k}}}{E_{\mathbf{k}}}\right) \tag{1.4.4}$$

being $E_{\mathbf{k}}$ defined as

$$E_{\mathbf{k}} = (\xi_{\mathbf{k}}^2 + \Delta_{\mathbf{k}}^2)^{1/2} \tag{1.4.5}$$

and $\Delta_{\mathbf{k}}$, yielding a real $\Delta_{\mathbf{k}}^* v_{\mathbf{k}}/u_{\mathbf{k}}$, to be derived self-consistently as:

$$\Delta_{\mathbf{k}} = -\sum_{\mathbf{l}} V_{\mathbf{kl}} \langle c_{-\mathbf{l}\downarrow} c_{\mathbf{l}\uparrow} \rangle = -\sum_{\mathbf{l}} V_{\mathbf{kl}} u_{\mathbf{l}}^* v_{\mathbf{l}} \langle 1 - \gamma_{\mathbf{l}0}^* \gamma_{\mathbf{l}0} - \gamma_{\mathbf{l}1}^* \gamma_{\mathbf{l}1} \rangle \tag{1.4.6}$$

The diagonalized hamiltonian is:

$$H_d = \sum_{\mathbf{k}} (\xi_{\mathbf{k}} - E_{\mathbf{k}} + \Delta_{\mathbf{k}} \langle c_{\mathbf{k}\downarrow}^* c_{-\mathbf{k}\uparrow}^* \rangle) + \sum_{\mathbf{k}} E_{\mathbf{k}} (\gamma_{\mathbf{k}0}^* \gamma_{\mathbf{k}0} + \gamma_{\mathbf{k}1}^* \gamma_{\mathbf{k}1}) \tag{1.4.7}$$

It is now worth commenting briefly on the result. For simplicity, the BCS isotropic approximation for $V_{\mathbf{kl}}$ is assumed:

$$V_{\mathbf{kl}} = \begin{cases} -V & \text{if } |\xi_{\mathbf{k}}|,\ |\xi_{\mathbf{l}}| \leq \hbar\omega_c \\ 0 & \text{otherwise} \end{cases} \tag{1.4.8}$$

where ω_c is a proper cutoff energy. Therefore at $T = 0$ (1.4.6) yields an isotropic (*s-wave*) $\Delta_{\mathbf{k}}$ real function:

$$\Delta_{\mathbf{k}} = \begin{cases} \Delta & \text{for } |\xi_{\mathbf{k}}| < \hbar\omega_c \\ 0 & \text{for } |\xi_{\mathbf{k}}| > \hbar\omega_c \end{cases} \tag{1.4.9}$$

which allows to evaluate $v_{\mathbf{k}}$ and $u_{\mathbf{k}}$ yielding:

$$v_{\mathbf{k}}^2 = 1 - u_{\mathbf{k}}^2 = \frac{1}{2}\left[1 - \frac{\xi_{\mathbf{k}}}{(\Delta^2 + \xi_{\mathbf{k}}^2)^{1/2}}\right] \tag{1.4.10}$$

The quantity $v_{\mathbf{k}}^2$, giving the fractional occupation number of the state of energy $\xi_{\mathbf{k}}$ in the $\mathbf{k}$ space, is plotted in figure 1.5: it is seen that, with respect to the normal state, in which all the states with energy $\xi_{\mathbf{k}} < 0$ are occupied and the states $\xi_{\mathbf{k}} > 0$ are empty, there is a redistribution of the occupation of the single-electron states, therefore giving an increase of the overall kinetic energy. Indeed, the total energy variation can be determined evaluating in the BCS ground state the first term of the hamiltonian H_d (1.4.7): going to the continuum approximation for the summation, denoting with N_F the (normal state) density of states at Fermi level and considering (weak-coupling limit) $N_F V \ll 1$ one obtains the difference between the total energy $U_s(0)$ of the

superconducting state and the corresponding energy in the normal state $U_n(0)$ ($U_n(0)$ comes from (1.4.7) setting $\Delta = 0$ and $E_{\mathbf{k}} = |\xi_{\mathbf{k}}|$). The result reads:

$$U_s(0) - U_n(0) = -\frac{1}{2} N_F V \tag{1.4.11}$$

which gives a net gain of energy (i.e. the condensation energy) as expected.

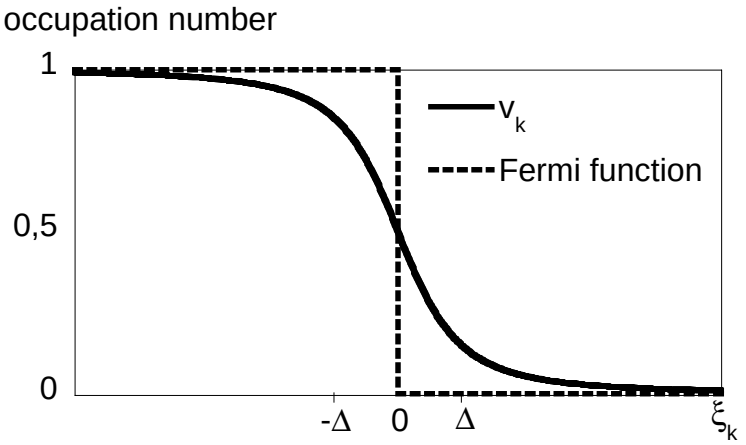

Figure 1.5: Energy $\xi_{\mathbf{k}}$ dependence of the fractional occupation number $v_{\mathbf{k}}$, compared with the Fermi function at T=0 K which would give full occupation only for $\xi_{\mathbf{k}} < 0$.

The second summation of equation (1.4.7) describes the increment of energy from the BCS ground state linked to the appearance of quasiparticle (QP) excitations, described by the number operators $\gamma^*_{\mathbf{k}}\gamma_{\mathbf{k}}$ and by the energy spectrum given by $E_{\mathbf{k}}$. Thus $\Delta_{\mathbf{k}}$ gives the energy gap to be exceeded in order to create an excitation[2]. For finite temperatures, since $\gamma_{\mathbf{k}}$ are fermion operators, the Fermi function $f(E_{\mathbf{k}}) = \left(e^{E_{\mathbf{k}}/k_B T} + 1\right)^{-1}$ describes QP state occupation, which can be used to solve $\Delta_{\mathbf{k}}$ from equation (1.4.6) for any temperature, allowing to obtain the T-dependent gap and T_c. For example, in the simple isotropic case above mentioned, equation (1.4.6) in the continuum notation gives:

$$\frac{1}{N(0)V} = \int_0^{\hbar\omega_c} \frac{\tanh\left[(\xi^2 + \Delta^2)^{1/2} \big/ (2k_B T)\right]}{(\xi^2 + \Delta^2)^{1/2}} \tag{1.4.12}$$

from which the temperature dependence for $\Delta(T)$ can be evaluated. The above expression gives $\Delta(T) \sim e^{-\Delta/k_B T}$ as $T \to 0$, which is a typical activated

[2]Note that, for particle number conservation, in isolated systems QP can be excited only in pairs, thus giving the spectroscopic gap equal to 2Δ in the simple case of isotropic $\Delta_{\mathbf{k}} = \Delta$.

behavior. On the other hand, when evaluated for $T = T_c$ where $\Delta(T_c) = 0$ and $E_{\mathbf{k}} = \xi_{\mathbf{k}}$, it gives the celebrated result:

$$\frac{\Delta(0)}{k_B T_c} \approx 1.764 \tag{1.4.13}$$

which was found to be in satisfying agreement with the experiment in many conventional superconductors.

As far as the QP density of states (DOS) is concerned, given the one-to-one correspondence between the $c_{\mathbf{k}}$ and the $\gamma_{\mathbf{k}}$ fermion operators, the density of states must be conserved giving: $N(E)dE = N_n(\xi)d\xi$, where N_n represents the density of states (DOS) in the normal state. In the usual s-wave case, and considering energies near the Fermi surface so that $N_n(\xi) \simeq N_F$, one obtains:

$$\bar{N}(E) = \frac{N(E)}{N_F} = \frac{d\xi}{dE} = \begin{cases} \frac{E}{(E^2-\Delta^2)^{1/2}} & \text{for } E > \Delta \\ 0 & \text{for } E < \Delta \end{cases} \tag{1.4.14}$$

which is plotted in figure 1.6.

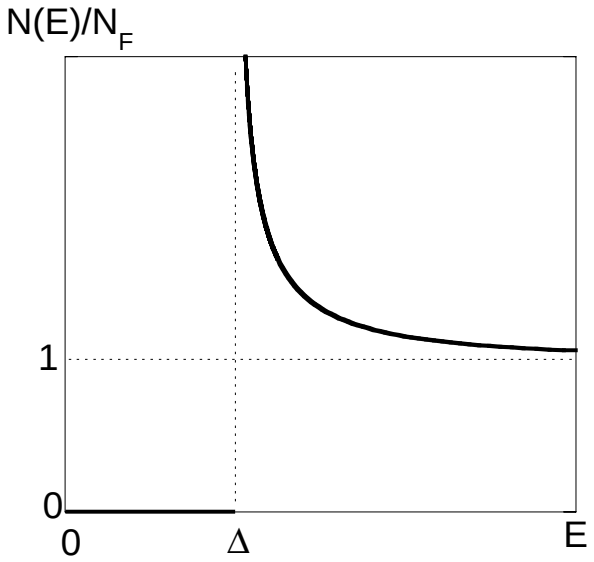

Figure 1.6: QP density of states in a s-wave superconductor in the superconducting state.

It is apparent that the QP spectrum has a gap Δ, as already noted: the presence of the gap means that any low temperature property which requires QP mediation (among the others: the specific heat, the variation of the penetration depth, the real part of the microwave conductivity) presents an activated behavior proportional to $\sim e^{-\Delta/k_B T}$. Moreover it is seen that starting from

$E = \Delta$ there is a square root diverging peak while for $E \gg \Delta$ the density of states converges to the normal state behavior.

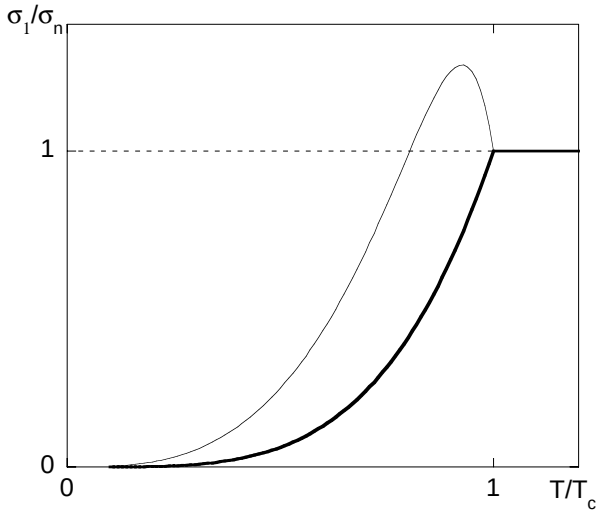

Figure 1.7: Temperature dependence of the low-frequency real part of $\tilde{\sigma}$ with coherence effects (thick line) compared with two-fluid model result (thin line).

The electrodynamic model in the BCS framework was originally developed by Mattis and Bardeen (MB) in their seminal paper [17]. Their clean local limit ($\xi_0 \ll l \ll \lambda$) computation, at low frequencies $\hbar\omega \ll \Delta$ and for a s-wave superconductor, gives a complex conductivity $\tilde{\sigma}$ that can be expressed [18] as a sum of superfluid and QP contributions, $\sigma_s + \sigma_n$, being

$$\sigma_s = \frac{ne^2}{\mathrm{i}m\omega}\left[1 - \int_\infty^\infty \left(-\frac{\partial f(E)}{\partial E}\right)\bar{N}(E)dE\right] \tag{1.4.15}$$

and

$$\sigma_n = \frac{ne^2}{m}\int_\infty^\infty \left(-\frac{\partial f(E)}{\partial E}\right)\bar{N}(E)\frac{1}{1/\tau_s(E) + \mathrm{i}\omega}dE \tag{1.4.16}$$

where τ_s is the energy dependent QP relaxation time in the superconducting state and where the energy interval E and relevant functions of E are specularly extended in the negative range. By comparison with the two-fluid expressions given in (1.3.2)–(1.3.4), it derives that within the requirements of this MB clean limit calculation, the two-fluid model holds if:

- the normal fluid fraction is defined as:

$$x_n = \int_\infty^\infty \left(-\frac{\partial f(E)}{\partial E}\right)\bar{N}(E)dE \tag{1.4.17}$$

- the relaxation time τ is defined as an average of $\tau_s(E)$ over the states:

$$\tau = \frac{\int_\infty^\infty \left(-\frac{\partial f(E)}{\partial E}\right) \bar{N}(E) \frac{\tau_s(E)}{1+\mathrm{i}\omega\tau_s(E)} dE}{\int_\infty^\infty \left(-\frac{\partial f(E)}{\partial E}\right) \bar{N}(E) \frac{1}{1+\mathrm{i}\omega\tau_s(E)} dE} \tag{1.4.18}$$

In the dirty limit, on the other hand, the two-fluid model (requiring the $x_n + x_s = 1$ condition) no longer holds. It is violated by the existence of the so-called coherence peak in the temperature dependence of the real part of $\tilde{\sigma}$, which is provided for by the MB theory in the dirty limit. In the BCS theory, coherence effects arise whenever interference effects among QP excitations are relevant, thus preventing their modelling as uncorrelated charge carriers implicit in two-fluid approaches. As an example, in figure 1.7 $\Re(\tilde{\sigma})/\sigma_n$ is qualitatively sketched in the case of coherence effects and as expected in the two-fluid case, having chosen a τ_s constant and equal to its normal state value. High temperature superconductors, studied throughout this thesis, have many properties which distinguish them from the simple isotropic s-wave superconductors considered here for illustrative purposes. In the following sections, therefore, a few of the peculiar features of HTCS will be described together with the effects that they have in defining their electrodynamics.

1.5 High temperature superconductors

The first representative of a new class of superconductors — $La_{2-x}Ba_xCuO_2$ with $T_c \simeq 35K$— was discovered in 1986 by Bednorz and Müller [19] (Nobel prize in 1987). Soon afterwards another cuprate, $YBa_2Cu_3O_{7-\delta}$ (YBCO) was synthesized [20], showing T_c ∼90 K above the liquid nitrogen temperature. Since then many other high-T_c materials have been discovered. Among the others, one can mentions the "BSCCO" (Bi-Sr-Ca-Cu-O) and "TBCCO" (Tl-Ba-Ca-Cu-O) families, having critical temperatures at atmospheric pressure as high as 130 K (see figure 1.2).

All these compounds have a layered structure, strongly anisotropic, in which CuO_2 planes are intercalated between insulating planes (see figure 1.9).

The perfectly stoichiometric compound is, in effect, a Mott insulator [21]: differently from a conventional band insulator, in which charge conduction is blocked due to double occupancy of sites, single electron occupancy prevents the creation of doubly occupied sites because of the strong Coulombian repulsion, therefore blocking charge conduction. Only upon doping, thus varying the charge carrier concentration, this situation changes and the material can acquire superconducting properties. In fact, doping plays a very relevant role

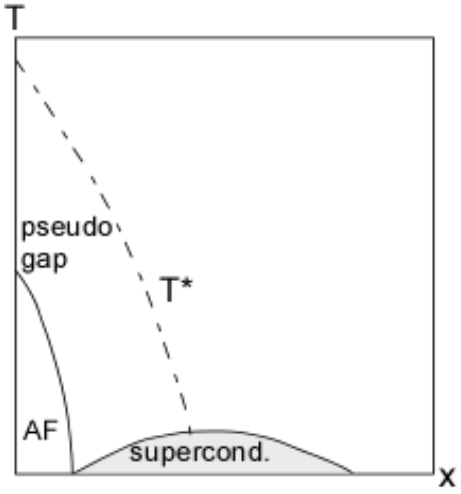

Figure 1.8: Qualitative temperature vs doping phase diagram for hole-doped HTCS (adapted from [22]).

in the determination of most of the properties of HTCS. Many temperature-doping phase diagrams have been proposed, on the basis of the experimental features as well as theoretical predictions. One [22] of those many diagrams is reported in figure 1.8, in order to exemplify a few relevant points[3]:

- the superconducting region (sometimes referred to as "superconducting dome") exists for a limited interval of doping values and temperatures. The maximum T_c occurs at the so called "optimum doping", while above and below this value there are the underdoped and overdoped superconducting regions, respectively;
- below the underdoped limit the material is in the Mott insulator phase with antiferromagnetic (AF) ordering, while above the overdoped limit the material behaves similarly to a Fermi liquid conductor;
- depending on doping, also the normal state of superconducting compounds presents different behaviors. In the underdoped case, the electronic DOS presents a suppression above the Fermi energy level which is usually referred to as a pseudogap [23]. This pseudogap effect holds up to a given temperature T^*, above which it disappears. It is believed that T^* represents a separate energy scale determining the physics of HTCS.

All those features, and many others, together with possible interpretations related to the role of the pseudogap are extensively treated in many reviews

[3]Here a phase diagram relative to the more common hole-doped HTCS is reported. All the materials studied in this thesis belong to this category.

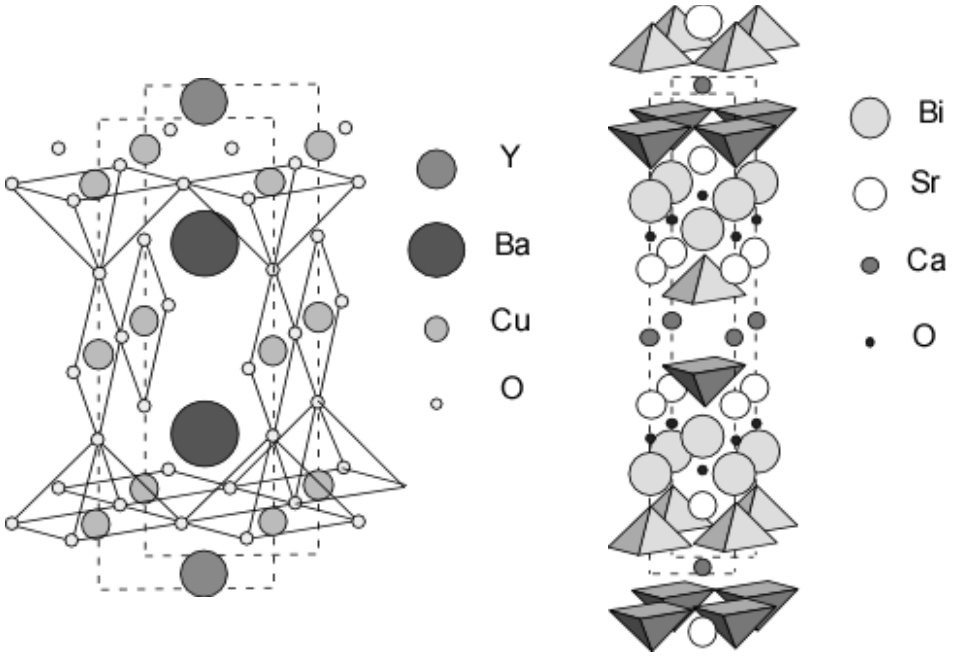

Figure 1.9: Elementary cell of YBCO (*left panel*) and BSCCO (*right panel*).

[23, 24, 25, 26, 27]. However, without going into details, one recalls here that they give indications that standard BCS could be inadequate in explaining the HTCS phenomena. Moreover, anisotropy, high T_c values, the small coherence lengths of these materials, all can enhance fluctuation effects casting doubts to the solidity of a mean field approach as the BCS one. Indeed, the origin of superconductivity in HTCS is still hotly debated and a comprehensive, widely accepted theory does not exist so far. On the other hand, the BCS theory, "extended" with a pairing mechanism based on boson mediators different from the phonons and by incorporating gap symmetries other than s-wave (see the next section), allows for the interpretation of electrical transport results [28, 29] and other properties [30, 31]. Therefore I will study HTCS within the BCS framework, leaving the debate to theoreticians.

1.5.1 Anisotropy and typical parameters

A common feature of cuprates is the layered structure in which conducting CuO_2 planes alternate with "insulating" layers. The resulting structural anisotropy, exemplified by the unit cells of $YBa_2Cu_3O_{7-\delta}$ and $Bi_2Sr_2CaCuO_{2+x}$ reported in figure 1.9 (which contextually defines the crystallographic axes used), reflects itself in a significant anisotropy of the physical properties, including penetration depths λ, coherence lengths ξ, critical currents and crit-

ical fields. The crystal structure determines a strong anisotropy mainly between c-axis and a, b properties (usually referred as "in-plane"), so that differences between a and b axes properties can be usually neglected. As a consequence, usually a, b averaged quantities are compared to c-axis quantities and the anisotropy parameter in the superconducting state is defined as $\gamma = \xi_{ab}/\xi_c = \lambda_c/\lambda_{ab}$.

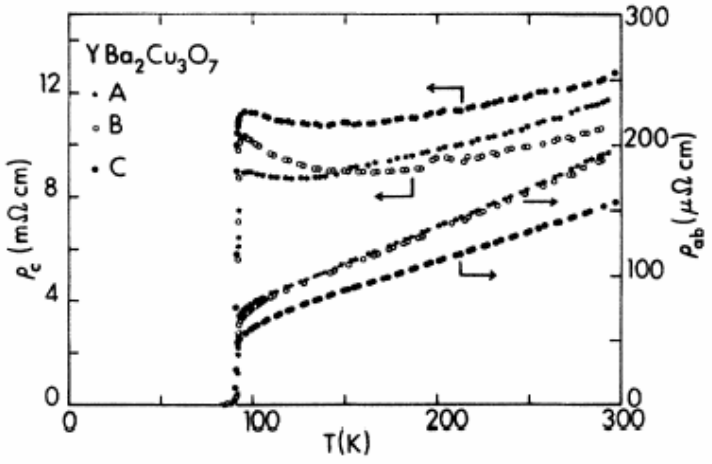

Figure 1.10: dc resistivity in an YBCO crystal for in-plane direction ρ_{ab} and c-axis direction ρ_c [32].

As an example, electrical transport properties differ profoundly passing from in plane to c-axis direction, as figure 1.10 shows in the case of dc resistivity of YBCO (taken from [32]): c-axis current, forced to flow through insulating planes separating CuO_2 conducting planes, can show a "semiconducting" behavior near T_c absent in the ab component.

The materials investigated in this thesis, i.e. YBCO, SmBCO (a Samarium-substituted version of YBCO), TBCCO and BSCCO, present various degrees of anisotropy, as reported in table 1.1. Since this thesis deals with in-plane quantities, from now on I will mainly refer to them, dropping the ab subscripts whenever possible.

1.5.2 Gap symmetry

The shape in the momentum space of the superconducting gap $\Delta_{\mathbf{k}}$ arises from the specific pairing mechanism and heavily influences the physical properties of the superconductor. In conventional superconductors the experiments showed an isotropic (s-wave) gap symmetry which is naturally explained within BCS

	YBCO	BSCCO	TBCCO
$T_c(K)$	89–93	83–89	101-105
$\lambda_{ab}(0)$ (Å)	1500	2500	2000–2900
$\xi_{ab}(0)$ (Å)	10–15	15-25	130
γ	5–9	15–600	19
$\mu_0 H_{c2}(0)$ (T)	200	150	180
reference	[8, 33]	[8]	[34, 35]

Table 1.1: Characteristic parameters of a few HTCS compounds.

phonon coupling. On the other hand, in HTCS the experimental results point to an anisotropic gap for which the most widely accepted form is the $d_{x^2-y^2}$, described in momentum space by the function [36]:

$$\Delta_{\mathbf{k}} = \Delta_0 \cos(2\phi) \tag{1.5.1}$$

where the constant $\Delta_0 > 0$ is the maximum gap amplitude and ϕ is the angle that the vector $\mathbf{k}$ in the momentum k_x-k_y plane makes with the k_x axis. A plot of equation (1.5.1) in the k_x-k_y plane is provided in figure 1.11 and compared to the isotropic s-wave (fully gapped) gap and to the so-called "extended s-wave", which will be commented on below.

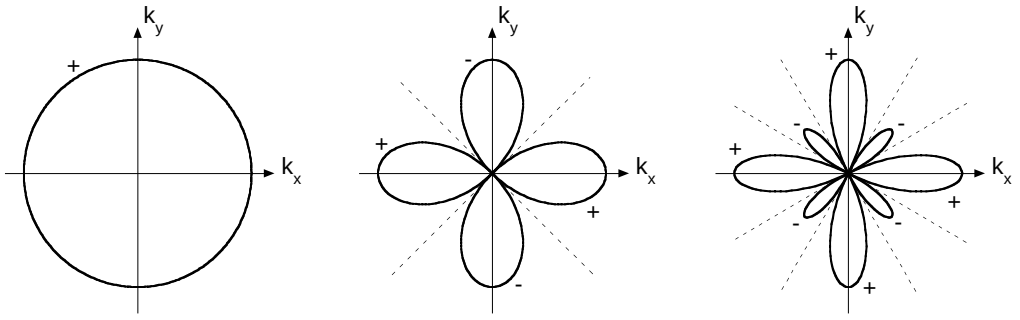

Figure 1.11: Isotropic s-wave, $d_{x^2-y^2}$ and extended s-wave gap symmetries in momentum space.

A key feature of the $d_{x^2-y^2}$ gap amplitude, besides its in-plane anisotropy, is the presence of zeroes (*nodes*) in specific regions of the Fermi surface. This fact can be appreciated by computing the density of states $\bar{N}(E)$ averaged over the Fermi surface, which is the quantity that enters effectively in defining many physical properties. It can be shown that [24]:

$$\begin{aligned}\bar{N}(E) &= \frac{1}{2\pi}\int_0^{2\pi}\bar{N}(E,\phi)d\phi = \frac{1}{2\pi}\int_0^{2\pi}\frac{E}{[E^2-\Delta_0^2\cos^2(2\phi)]^{1/2}}d\phi = \\ &= \begin{cases}\frac{2}{\pi}\frac{E}{\Delta_0}K\left(\frac{E}{\Delta_0}\right) & \text{for } 0 \le E < \Delta_0 \\ \frac{2}{\pi}K\left(\frac{\Delta_0}{E}\right) & \text{for } E > \Delta_0\end{cases}\end{aligned} \tag{1.5.2}$$

where K is the complete elliptic integral function of the first kind.

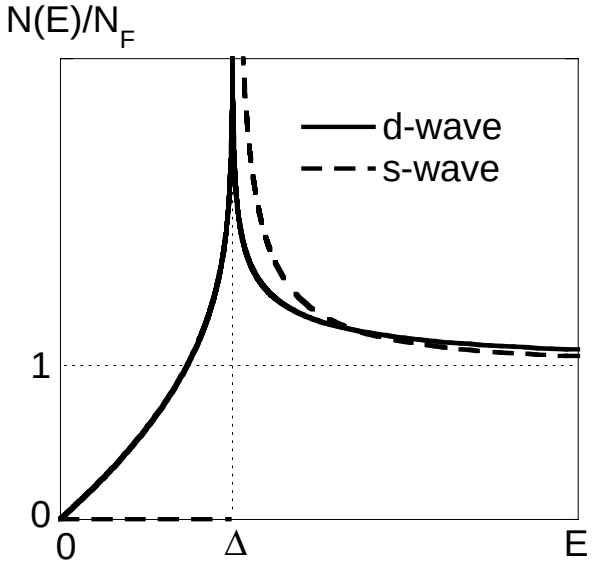

Figure 1.12: Normalized DOS of a d-wave superconductor, with isotropic s-wave DOS given for comparison.

The above equation is plotted in figure 1.12 together with the already seen result for the isotropic s-wave gap. The presence of nodes in the gap has a dramatic impact on the physics of d-wave superconductors. Besides the different type of the divergence at $E = \Delta_0$ (logarithmic and square root for d- and s-wave, respectively), the main fundamental feature is the presence of a non-zero DOS down to the Fermi level, which varies linearly as $\frac{E}{\Delta_0}$ for $E \ll \Delta_0$. These states allow for the existence of zero-energy excitations with respect to the superconducting ground state. These excitations, the so-called nodal quasiparticles (QP), can therefore be created by any energy perturbation of the superconducting system, whichever its smallness may be. As a consequence they determine non-activated behavior at low T of many thermal and electrodynamic properties, which exhibit power law behavior in striking contrast with fully gapped superconductors. The existence of nodes in the gap can be then

inferred from various types of measurements, a small sample of which is listed in table 1.2. Among the others, angular resolved photoemission spectroscopy (ARPES) (for a review see [37]) deserves a separate comment, since it allows for a complete scan on the momentum space of the gap amplitude function: its results are commonly taken as strong evidence for a nodal fourfold gap, consistent with d-wave, although a few inherent features of the technique do not always allow for a univocal interpretation of data.

It is worth mentioning, anticipating the more detailed discussion of the next chapter, that circulating supercurrents in the vortex state can excite nodal QP as well.

It should be emphasized that nodal QP with a DOS given by equation 1.12 are common to many gap symmetries, provided the existence of nodal lines [24]. In order to effectively discern $d_{x^2-y^2}$ gap from other nodal functions it is important to explore its phase behavior. A few phase sensitive techniques (for a review see for example [36, 38]), which use Josephson tunnelling in order to sense the gap π phase shift caused by a 90° rotation around the c-axis, indeed seem to support the $d_{x^2-y^2}$ scenario [39]. For completeness one recalls a few works [40] in which alternative nodal gap symmetries (sometimes referred to as "extended s-wave", see figure 1.11), are suggested to be compatible with the whole experimental evidence, while in [41] measurements on BSCCO are interpreted as pointing to dominantly isotropic s-wave symmetry [42] .

physical quantity	s-wave	d-wave	HTCS
penetration depth λ	$\sim e^{-\Delta/k_BT}$	$\sim T$	$\sim T$
real conductivity σ_1	$\sim e^{-\Delta/k_BT}$	$\sim T^2$	$\sim T$
electronic specific heat	$\sim e^{-\Delta/k_BT}$	$\sim T^2$	$\sim T$
phase shift over 90^o	0	π	π

Table 1.2: A few gap-symmetry related properties, theoretically expected for s-wave and d-wave symmetries in the low-T regime, compared to HTCS experimental results.

Summarizing, being the $d_{x^2-y^2}$ function the most widely —although not yet universally— accepted form, from now on I will refer to the "d-wave" or "nodal" nature of the HTCS gap, keeping in mind that for us the relevant feature is the existence of nodal QP, irrespective of the actual symmetry of the nodal gap.

1.5.3 Microwave electrodynamics

Microwave electrodynamic response in HTCS can be conveniently interpreted by resorting to the two-fluid model. Indeed, its validity is supported by a series

of results, hereby briefly recalled.

First, the characteristic lengths satisfy the clean local condition $\xi_0 \ll l \ll \lambda_L$ so that HTCS electrodynamics is in the local limit for both the superfluid and the normal fluid. Locality for both components is not always straightforward, since QP and superfluid can separately undergo the locality condition [18].

Second, starting from the earlier measurements of Nuss et al. [43] in the millimeter range, followed by other measurements (e.g. [29, 44]), no coherence peak below T_c is observed. A peak shows up at lower temperatures, but it is usually interpreted as caused by a strong temperature variation of the QP scattering time, compatible with the two-fluid picture. This point will be considered again later.

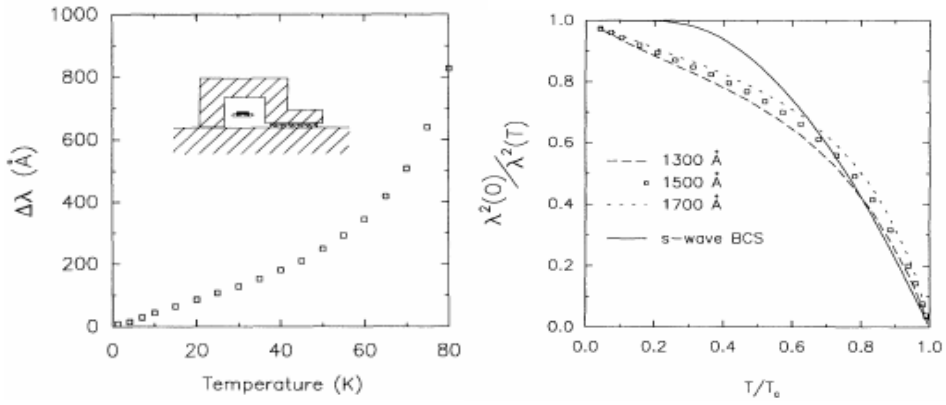

Figure 1.13: *Left panel*: temperature dependence of $\Delta\lambda$ in pure YBCO crystal. *Right panel*: temperature dependence of the ratio $[\lambda^2(0)/\lambda^2(T)] \propto n_s$, showing the linear T-dependence at low T, as expected for a d-wave superconductor, compared to the s-wave activated behavior. (taken from [33]).

No coherence peak was observed either in nuclear magnetic relaxation measurements [45] (in contrast to its observation in conventional superconductors [46]). It is thought [45] that the d-wave gap of HTCS, with the smearing of the DOS peak at $E = \Delta_0$ increased by scattering processes, can explain its absence.

It appears then that a two-fluid model can be safely applied for the interpretation of the data. Various authors (e.g. [28, 47]) derived a two-fluid model for the d-wave symmetry case, giving [18, 28] same equations as (1.4.15)–(1.4.18), provided that the density of states $\bar{N}(E)$ is the Fermi surface averaged quantity shown in equation (1.5.2). This picture can change for temperatures very close to 0 K, depending on impurity concentration, since an extra density of states introduced by impurities near the Fermi surface can determine a different regime.

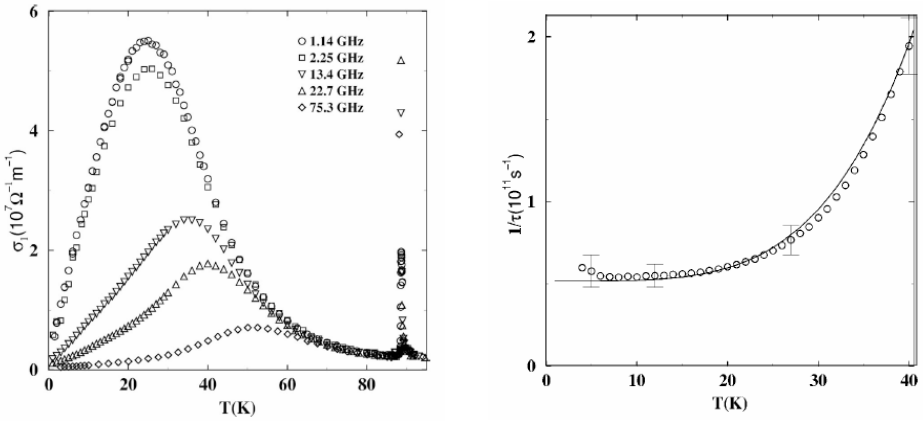

Figure 1.14: *Left panel*: real conductivity σ_1 in YBCO for various frequencies, showing a peak at low temperatures. *Right panel*: extracted scattering rate (taken from [29]).

A few relevant experimental results in HTCS are now reviewed.

One of the most convincing arguments in favour of the d-wave picture is the low-T dependence of the in-plane penetration depth $\lambda(T)$: while initial measurements showed a quadratic behavior, a linear dependence was measured by the Vancouver group [33] in pure YBCO crystal (see figure 1.13). The latter result is consistent with the theoretical expectations [48] for intrinsic materials, while the former $\sim T^2$ result can be ascribed to strong impurity scattering contributions present in less pure samples, as suggested in [28, 49].

A second peculiar feature of some HTCS is the presence of a giant peak in $\sigma_1(T)$, as reported in figure 1.14 (left panel) for different measuring frequencies [29]. The same behavior was found by other authors [50]. This peak was interpreted as the result of the competition, as the temperature is lowered, between the normal fluid depletion and a strong increase of the QP relaxation time τ (right panel of figure 1.14), proportional in this temperature range to $\approx T^4$. This strong τ variation, in turn, can be interpreted [28, 50] as a fast disappearance of an inelastic contribution to τ, important at higher temperatures.

The temperature dependence of σ_1 is not in perfect agreement with theoretical expectations for a d-wave superconductor: in fact, in pure YBCO crystals $\sigma_1 \sim T$ [29], at odds with theoretical predictions $\sigma_1 \sim T^2$. This discrepancy is tentatively ascribed [51] to residual scattering phenomena having origin from order-parameter spatial inhomogeneities.

Chapter 2

The mixed state

In this chapter the behavior of type II superconductors in the mixed state is described with particular attention to electrical transport properties. The ideal Abrikosov state will be firstly described, followed by a brief survey of the so-called vortex matter in HTCS when thermal effects, disorder and layer decoupling effects are taken into account. The basic vortex dynamics and the main forces acting on vortices will be then considered. Afterwards the relation between vortices and quasiparticle excitations will be recalled. At the end a model allowing to capture the whole mixed state electrodynamic response in the microwave range will be described.

2.1 The Abrikosov state

Type II superconductors, identified by values of the Ginzburg-Landau parameter $\kappa = \lambda/\xi > 1/\sqrt{2}$[1], have a magnetic susceptibility $\chi > -1$ when the applied magnetic field H is $H_{c1} < H < H_{c2}$, with H_{c1} and H_{c2} the lower and upper critical fields, respectively. The flux of the magnetic induction $\phi(\mathbf{B})$ partially penetrates in the superconductor volume along flux "tubes", called *fluxons*. This behavior can be explained in the framework of the GL theory: it can be shown that a normal/superconducting interface has a net energy arising from the difference between magnetic and condensation energies. These energies vary spatially on the different scales λ and ξ, respectively, so that in type II superconductors with $\lambda > \xi/\sqrt{2}$ their net difference is negative. Abrikosov [52] showed that in the mixed state a regular distribution of cylindrical "normal" regions with $\psi = 0$ on the axis, each one carrying a flux quantum $\Phi_0 = h/(2e) = 2.07 \cdot 10^{-15}$ T m^2, allows indeed an overall reduction

[1]The GL theory, strictly valid near T_c, gives a κ independent from temperature. Indeed, considered in the whole temperature range κ acquires a slight temperature variation.

of free energy with respect to the fully diamagnetic Meissner state. In the ideal isotropic material, fluxons are round cylinders with the axis parallel to the externally applied magnetic field and are surrounded by circular supercurrents, which have brought fluxons to be alternatively named *vortices*.

Working in the GL framework, the order parameter ψ and the magnetic induction B around a vortex can be determined. Considering an isolated vortex, given cylindrical coordinate frame (r, θ, z) having the z-axis coincident with the fluxon axis, the ψ profile is $\psi(\mathbf{r}) = \psi_\infty f(r) e^{i\theta}$, being ψ_∞ the bulk value of the order parameter and $f(r) \approx \tanh(r/\xi)$ [6]. The main points to catch here are the null value $\psi(0) = 0$ along the fluxon axis and the order parameter phase which varies by 2π around the vortex (consistently with the requirement of being one-valued while in the same time being not uniform). From the latter property, by integrating the second GL differential equation (1.2.3) along a circle sufficiently far away from the fluxon (so that the vortex supercurrent density J_s is negligible) one obtains the quantization of the flux quantum Φ_0 associated to the vortex. For $\kappa \gg 1$ and for $r > \xi$ the field profile is [7]:

$$\mathbf{B}(\mathbf{r}) = \frac{\Phi_0}{2\pi\lambda^2} K_0 \left(\frac{r}{\lambda}\right) \hat{\mathbf{z}} \tag{2.1.1}$$

being K_0 the zeroth order Hankel function of imaginary argument. For $r \gg \lambda$ one has $B \sim e^{-r/\lambda}$. These profiles are plotted in figure 2.1.

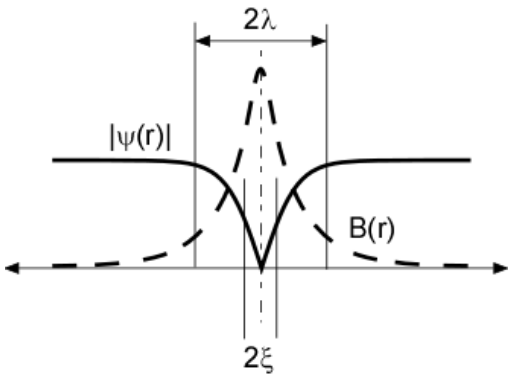

Figure 2.1: Structure of a single vortex centered in $r = 0$: $\psi(r)$ and $B(r)$ profiles, with length scales ξ and λ, respectively.

The free energy per unit length ϵ_{fl}, which is the vortex line tension, can be determined considering the kinetic contribution of the vortex supercurrents and the field energy, and neglecting the condensation energy which involves

only the small area of radius $\propto \xi$:

$$\epsilon_{fl} = \frac{\mu_0}{2} \int \left[B(r)^2 + \lambda |\nabla \times \mathbf{B}(r)|^2 \right] dS \tag{2.1.2}$$

Using expression (2.1.1) for the field profile, the above equation yields [7]:

$$\epsilon_{fl} = \frac{\Phi_0^2}{4\pi\mu_0\lambda^2} \ln \kappa \tag{2.1.3}$$

The neglected contribution due to the condensation energy lost in the vortex core changes only slightly the result. One has [7]:

$$\epsilon_{fl} = \frac{\Phi_0^2}{4\pi\mu_0\lambda^2} (\ln \kappa + o(0.1)) \tag{2.1.4}$$

where $o(0.1)$ represents a constant of the order of 0.1. Within this framework the lower critical field H_{c1} can be easily determined by equating the energy cost (per unit lenght) of a fluxon, using ϵ_{fl} from (2.1.3), with the energy gained by the appearance of a single vortex at a magnetic field $H = H_{c1}$ [6], equal to $H_{c1}\Phi_0$, yielding:

$$H_{c1} = \frac{\Phi_0}{4\pi\mu_0\lambda^2} \ln(\kappa) = H_c \frac{\ln(\kappa)}{\sqrt{2}\kappa} \tag{2.1.5}$$

being H_c the thermodynamic critical field which has been defined by the condensation energy.

The application of field $H > H_{c1}$ determines the creation of many vortices that arrange on regular patterns. Abrikosov identified the possible regular patterns as having square and hexagonal basic unit cells (see figure 2.2), with nearest neighbor distance a_{FL} equal to [6]:

$$a_{FL} = a_0 \sqrt{\frac{\Phi_0}{B}}, \quad a_0 = \begin{cases} 1 & \text{for square cell} \\ \sqrt[4]{4/3} & \text{for hexagonal cell} \end{cases} \tag{2.1.6}$$

The latter, giving a triangular lattice, has the lowest energy and gives a stable configuration confirmed by experiments (see figure 2.3). Depending on the temperature range, magnetic field orientation, disorder contributions and material anisotropy (as for HTCS), the square lattice can be also observed [53]. The lattice is found to be stable against perturbations ("elasticity of the vortex lattice"). One now considers two fluxons with z-parallel axes positioned in $\mathbf{r}_1$ and $\mathbf{r}_2$. The overall energy can be computed through (2.1.2) using the overall

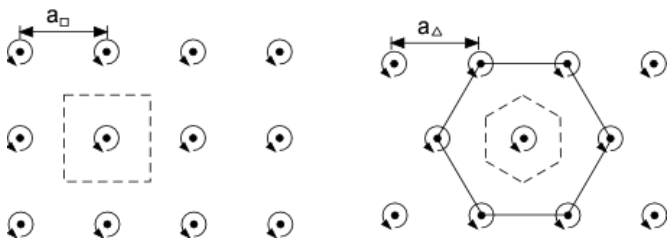

Figure 2.2: Square (*left panel*) and hexagonal (*right panel*) fluxon lattice, viewed along a section normal to vortices lattices. Vortex supercurrents are sketched by round arrows.

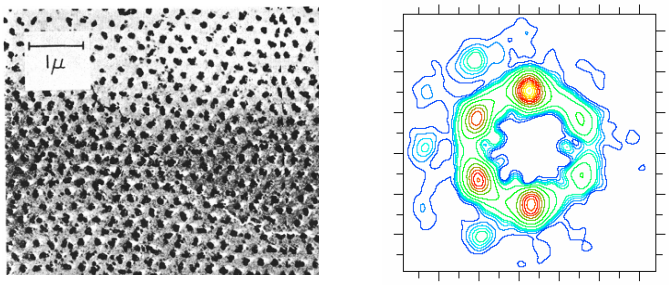

Figure 2.3: *Left panel*: photograph of a sample in the mixed state, in which the decoration technique reveals the positions of the fluxons through locally settled ferromagnetic microparticles (taken from [54]). *Right panel:* typical diffraction pattern in a YBCO sample in the mixed state, obtained through Small Angle Neutron Spectroscopy (SANS) (taken from [55]). The hexagonal geometry is the one expected (by spatial Fourier transformation) for a triangular fluxon lattice.

field $\mathbf{B}(\mathbf{r}-\mathbf{r}_1)+\mathbf{B}(\mathbf{r}-\mathbf{r}_2)$, with $\mathbf{B}(r)$ as in (2.1.1). The result consists in two self-energy terms ϵ_{fl} as (2.1.3) plus the following interaction term:

$$\epsilon_{int} = \frac{\Phi_0^2}{2\pi\mu_0\lambda^2} K_0\left(\frac{|\mathbf{r}-\mathbf{r}_1|}{\lambda}\right) \tag{2.1.7}$$

which corresponds to a repulsive interaction[2]. The force per unit length exerted by fluxon 2 on fluxon 1 can be obtained taking the derivative of ϵ_{int} which, put in vector form, yields [6]:

$$\mathbf{f}_{L,21} = \mathbf{J_2}(\mathbf{r_1}) \times \mathbf{\Phi}_0 \tag{2.1.8}$$

where the vector $\mathbf{\Phi}_0$ is along the vortex axis and has Φ_0 modulus while $\mathbf{J}$ is the current density of the fluxon 2. For an arbitrary distribution of vortices,

[2]One mentions that, under particular circumstances, there can be a coexistence of fluxons and antifluxons (with antiparallel orientation of the trapped flux) which experience attractive interaction.

the total force on any vortex results from the sum of all the current densities (which give a total **J** on the vortex site):

$$\mathbf{f}_L = \mathbf{J} \times \mathbf{\Phi}_0 \tag{2.1.9}$$

The symmetry of the Abrikosov fluxon lattice assures that the overall **J** is zero, thus allowing fluxons to remain motionless. In addition, any vortex displacement from its equilibrium position is countered by this intervortex interaction giving elastic properties to the Abrikosov lattice. The magnetic induction profile in the vortex state deserves a short discussion. When the applied field is $H_{c1} \ll H$, many vortices are present: when λ is large and $\kappa = \lambda/\xi \gg 1$ as in HTCS, their field profiles strongly overlap while their cores are still well separated. The resulting magnetic induction (qualitatively depicted in figure 2.4) is then $\mathbf{B}(\mathbf{r}) \approx \mu_0 \mathbf{H}(\mathbf{r})$, apart a small ripple: this is the so-called London limit. As an important consequence, demagnetization effects are not relevant in this case since they are confined to H values comparable to H_{c1}.

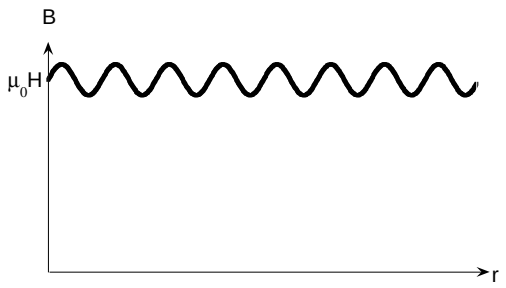

Figure 2.4: B(r) resulting from overlapping vortices.

In HTCS, because of their high κ values, the London approximation is valid in the great part of the mixed state region (see magnetization curves in figure 2.5).

By still increasing the applied field, vortex cores eventually overlap and the sample switches to the normal state. An estimate of the upper critical field $H_{c2} \approx \Phi_0/(2\pi\xi^2\mu_0)$ can be obtained considering vortex cores of section $\approx \pi\xi^2$ which cover the whole superconductor and give the uniform induction $\Phi_0/(2\pi\xi^2) = \mu_0 H_{c2}$. An exact calculation gives for H_{c2} the following expression [6]:

$$H_{c2} = \frac{\Phi_0}{2\pi\mu_0\xi^2} = H_c\sqrt{2}\kappa \tag{2.1.10}$$

Till now an ideal fluxon lattice has been considered, neglecting many factors

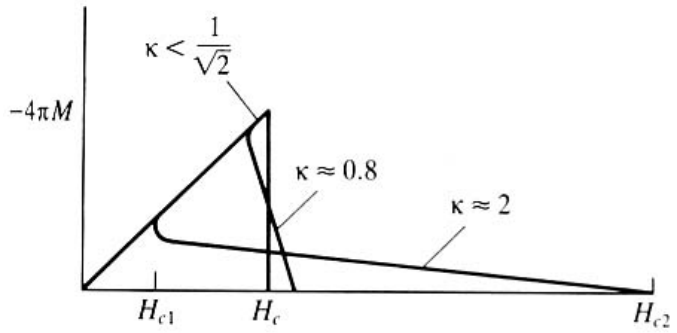

Figure 2.5: Magnetization curve for type II superconductors, compared with type I superconductors (from [6]).

that can modify its regular configuration. In the following section a brief discussion on the complexity of real vortex systems will be presented.

2.2 Vortex matter in HTCS

In HTCS vortices can attain such a variety of configurations that it is customary to refer to them as "vortex matter". This term emphasizes the analogy in variety and complexity between the possible arrangements of fluxons and the arrangements of ordinary particles (atoms or molecules) in conventional matter. With respect to the simple Abrikosov lattice, the complexity is enormously increased due to the competition between many factors:

- high values of the penetration depth λ result in low flux lattice elasticity and line tensions (equations (2.1.3) and (2.1.7));
- material anisotropy further favors flux line distortion. In more anisotropic HTCS the layered structure can determine the decomposition of the flux lines into weakly interacting bidimensional vortices (pancakes);
- in addition to the above mentioned intrinsic properties, disorder plays an important role: pinning centers are effective when their spatial dimensions are $\sim \xi$, yielding an interaction energy $\sim \xi^3$ (see section 2.5). In HTCS the small values of ξ make even defects of atomic size important and give small values of the pinning energy. The large number of such defects can exceed the number of flux lines and thus a disordered phase can arise;

- high temperatures make the thermal energy of the same scale of the small energy scales related to the above phenomena. Thus thermal effects can easily assist flux lines bending and decoupling, flux lattice distortion and depinning.

As a result of the combined action of the above mentioned effects, many vortex phases can arise (see, for example, the reviews [56, 57]). Two possible general phase diagrams are presented in figure 2.6 (from [58]) and 2.7 (from [59]).

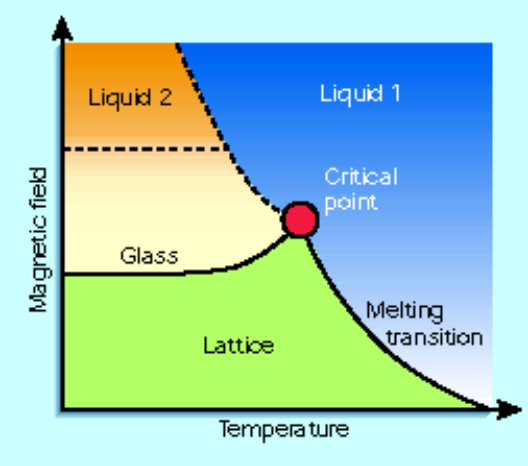

Figure 2.6: A general vortex phase diagram from [58].

As depicted in figure 2.6, the standard Abrikosov "solid" lattice is limited to the region of lower H and T values[3]: in this case the flux system has long range order, flux lines are straight and mutually interacting. By increasing the temperature this system undergoes a first order melting transition accompanied by very abrupt changes in physical properties. In the liquid phase the thermal energy is high enough to let fluxons move freely, regardless of one another. Disorder favors the loss of long range order: by increasing the field, the solid Abrikosov phase can become a vortex glass [60] having still pinned vortices. In this case by increasing the temperature the melting to a liquid phase occurs giving a second order phase transition. Moreover, several liquid phases can exist as sketched in figure 2.6. A few of the possible liquid phases are pictorially represented in figure 2.7. By increasing the field one can pass firstly from slightly bent flux lines at lower fields to entangled lines (corresponding to a

[3]Due to small values of H_{c1}, the Meissner state is not visible on this scale.

phase which can be described as a polymeric glass [61]) at intermediate fields and lastly to decoupled lines (bidimensional pancakes) at higher fields.

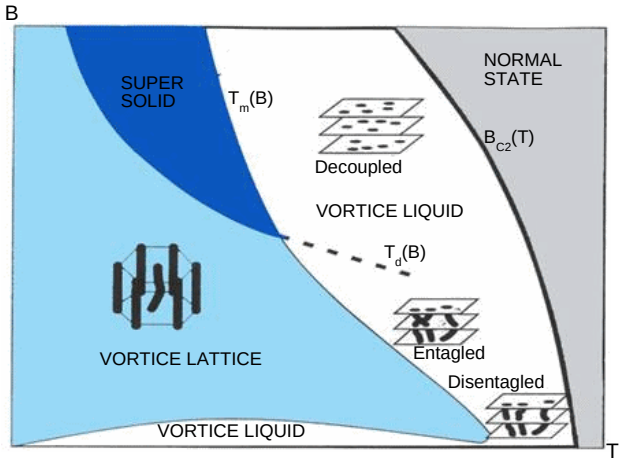

Figure 2.7: A general vortex phase diagram with pictorial representation of vortex phases (from [59]).

As it can be seen, many vortex phases are possible in HTCS. It is important to note that each phase of the vortex matter can have different fluxon mobility, determining different electrodynamic response: these effects will be qualitatively described in the next section, devoted to the description of the basic concepts of vortex dynamics.

2.3 Moving vortices: basics of dynamics

Among the possible causes of vortex motion (electrical, thermal, magnetic), the application of an external transport current density $\mathbf{J}$ exerts on a vortex a net Lorentz force per unit length $\mathbf{f}_L = \mathbf{J} \times \mathbf{\Phi}_0$ (equation (2.1.9)). As a consequence, vortices can start to move with velocity $\mathbf{v}_L$. Vortices motion has a strong impact on the conducting properties of superconductors in the mixed state, since a moving fluxon determines an electric field. This can be shown as follows (see reference [62]): a general relation for superfluids states that the difference of chemical potential μ between two points is related to the time derivative of the phase difference of the order parameter according to:

$$\Delta\mu = \hbar \frac{d}{dt} \Delta\phi \tag{2.3.1}$$

which for the charged superfluid of superconductors translates to[4]:

$$\Delta V = \frac{\hbar}{2e}\frac{d}{dt}\Delta\phi \tag{2.3.2}$$

Considering the phase distribution around a vortex depicted on the upper panel of figure 2.8, the points P_1 and P_2 experiment a variation of their difference in phase $\Delta\phi$ equal to 2π for each fluxon passing between them (see lower panels of figure 2.8).

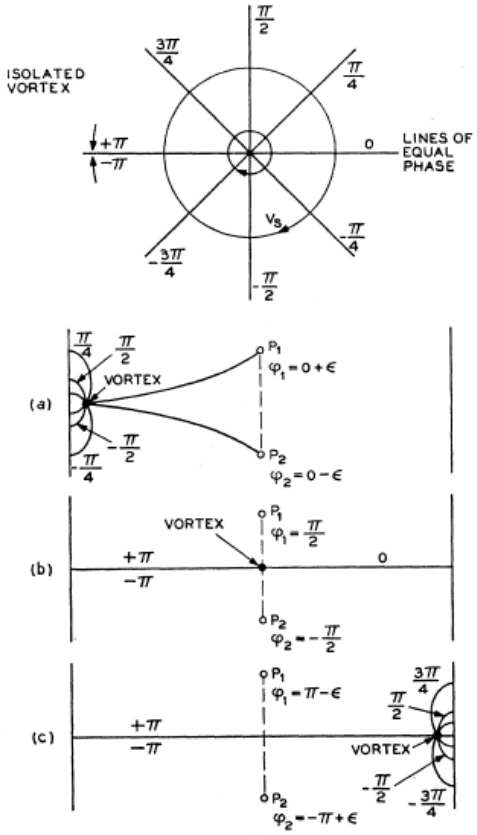

Figure 2.8: *Upper panel*: phase distribution around a vortex. *Lower panels*: phase slip determined by a moving vortex (from [62]).

Given a fluxon density $n_{fl} = B/\Phi_0$, if fluxons move perpendicularly to the segment $\overline{P_1P_2}$ of length l with velocity v_L, the average number of phase slips 2π in the time interval dt is $n_{fl}lv_Ldt$, yielding:

$$d(\Delta\phi) = 2\pi\frac{B}{\Phi_0}lv_Ldt \tag{2.3.3}$$

[4]Indeed, this equation is the same describing the ac Josephson effect.

so that the electric field is:

$$E = \frac{\Delta V}{l} = \frac{\hbar}{2e}\frac{d}{dt}(\Delta\phi) = Bv_L \tag{2.3.4}$$

In vector form:

$$\mathbf{E} = \mathbf{B} \times \mathbf{v}_L \tag{2.3.5}$$

which yields the local electric field $\mathbf{E}$ "induced" by a fluxon moving with velocity $\mathbf{v}_L$ in a magnetic induction $\mathbf{B}$. For a more complete derivation of the above equation see [63] and references therein. Thus, when vortex motion arises, an electrical field $\mathbf{E}$ takes place inside the superconductor. In turn, $\mathbf{E}$ puts in motion quasiparticles which transfer energy to the superconductor subtracting it from the kinetic energy of the vortex, which is then slowed down. This process can be phenomenologically described through a force per unit length f_{env} acting from the environment on moving vortices and opposing to their motion.

In real materials fluxon motion is prevented by pinning: pinning sites exert a pinning force per unit length f_p which attracts fluxons opposing to their motion and in general reducing the resulting vortex velocity $\mathbf{v}_L$. With dc currents and pinning, resistance appears only for current densities J greater than a given critical value J_c capable of giving $\mathrm{f}_L > \mathrm{f}_p$.

Finite temperature determines thermal motion of fluxons around their equilibrium positions, possibly allowing them to jump between different sites (*flux creep*).

Various phases of the vortex matter can differently affect the vortex dynamics. For example, the elasticity of the Abrikosov lattice makes few pinning centers very effective in blocking the motion of the whole lattice, while in the liquid phase vortices can only be individually pinned, thus leaving the majority of them more free to move and more subject to flux creep effects. The pinning effectiveness is also influenced by the flux line tension: rigid flux line can be pinned by a single pinning center, but pancake vortices require to be individually pinned on each distinct layer. Clusters of entangled flux lines, on the other hand, would present lower mobilities with respect to independent flux lines or pancakes.

The extreme complexity of vortex matter in HTCS does not allow a comprehensive description of the vortex dynamic. In most cases, however, this complexity can be "hidden" into the field and temperature dependencies of appropriate parameters. Following this line, from now on I will present mainly single vortex models, relying on the possibility to incorporate collective effects into suitably redefined lumped parameters.

Within this framework, the next three sections will be devoted to the modelling of simple vortex dynamics from the point of view of electrical transport.

2.4 Vortex viscosity

In general, the equation of steady motion for a vortex in absence of pinning is $\mathbf{f}_L + \mathbf{f}_{env} = 0$ where $\mathbf{f}_{env}$ represents the force per unit length that the environment exerts on the vortex. This force can be written as a viscous drag [6][5]:

$$\mathbf{f}_{env} = -\eta \mathbf{v}_L \tag{2.4.1}$$

where η is the so-called vortex viscosity. The microscopic origin[6] of the viscosity η was addressed by Bardeen and Stephen (BS) [67] for s-wave conventional superconductors. The power dissipated per vortex unit length, $W = \mathbf{f}_{env} \cdot \mathbf{v}_L = \eta v_L^2$, is transferred to normal currents, flowing inside vortex cores (modelled as fully normal cylinders with radius $\sim \xi$) and closing outside them. These currents give a Joule dissipated power $(v_L^2 \Phi_0^2)/(2\pi\xi^2\rho_n)$ (being ρ_n the resistivity in the normal state) which, equated to W, gives the following BS expression for the viscosity:

$$\eta = \frac{\Phi_0 B_{c2}}{\rho_n} \tag{2.4.2}$$

The BS model is valid for dirty s-wave superconductors ($\xi_0 \gg l$, with l mean free path of normal electrons). In the clean limit the relations are more complex. In fact Caroli, de Gennes and Matricon [68] have computed the bound states accessible to QP in the fluxon cores. Among these states, the dominant contribution arises from the so-called anomalous branch, in which there is a quantization of the energy levels having a spacing equal to $\Delta^2/E_F = \hbar\omega_0$, being the *minigap* $\omega_0 = e\mu_0 H_{c2}/m$ computed as the cyclotron angular frequency at H_{c2} [64]. Blatter et al [56, 64] computed η in the general s-wave case obtaining:

$$\eta = \pi\hbar n \frac{\omega_0\tau}{1 + (\omega_0\tau)^2} \tag{2.4.3}$$

where τ is the QP relaxation time. The BS value (2.4.2) is recovered if $\omega_0\tau \ll 1$ using $\rho_n = m/(ne^2\tau)$: in this case the bound states spacing $\sim \omega_0$ is smaller than the relaxation broadening $\sim \tau^{-1}$, giving a continuous spectrum of levels essentially equal to the one existing in the normal state. In the opposite

[5] Hall components are not considered. In any case it can be shown [64] that for low enough frequencies the Hall component can be included inside an effective viscosity parameter.

[6] The microscopic models that from now on will be recalled are all considered in the low frequency limit. As far as I know, no experiments in the microwave range have shown any frequency dependence of η, thus justifying this choice. In particular, multifrequency measurements on YBCO [65] have shown a frequency-independent η. High frequency models for η can be found in [66].

superclean limit $\omega_0\tau \gg 1$, bound levels are well resolved and viscosity reduces to $\eta \approx \pi\hbar n/(\omega_0\tau)$ (see figure 2.9).

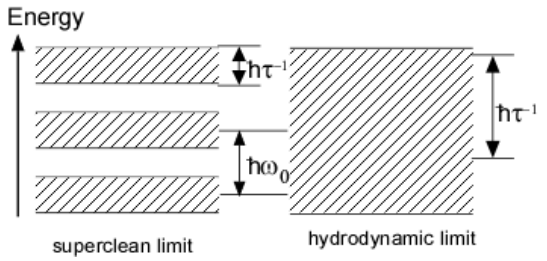

Figure 2.9: Bound levels energy spacings in the vortex cores of s-wave superconductors in the superclean limit $\omega_0\tau \gg 1$ (*left panel*), and hydrodynamic limit $\omega_0\tau \ll 1$ (*right panel*).

In HTCS, because of their d-wave gap and small values of ξ, the picture can change as shown in [63, 69, 70]. First of all, HTCS are always in the clean/superclean regimes since $l \gg \xi_0$. In addition, the minigap ω_0 now acquires the momentum $\mathbf{k}$ dependence of the d-wave gap $\Delta_{\mathbf{k}}$, thus becoming vanishingly small along the nodal directions. Only very low-energy QP remain localized in the vortex core, while QP along nodal directions escape from it acquiring a delocalization of the order of the intervortex distance a_{FL}. This gives an additional level quantization $\propto a_{FL}^{-1} \propto B^{1/2}$ valid for delocalized QP. Therefore there are two relevant energy scales in the d-wave case: the quantity analogous to the s-wave minigap, $\tilde{\omega}_0 \sim \Delta_0^2/E_F$, and the true interlevel gap $\Omega_0 \sim \tilde{\omega}_0\sqrt{B/B_{c2}}$. In this situation essentially three regimes can be recognized (see figure 2.10): the first one is the moderately clean regime $\tilde{\omega}_0\tau \ll 1$ in which local QP contribution dominates, giving results similar to the s-wave case (equation (2.4.3) with $\tilde{\omega}_0$ in place of ω_0). The two remaining regimes are subcases of the superclean regime $\tilde{\omega}_0\tau \gg 1$, in which delocalized QP give an important contribution. One is the intermediate regime $\Omega_0\tau \ll 1$, in which energy levels are resolved on average but with the true interlevel gap Ω_0 still obscured by the relaxation time broadening corresponding to significant dissipation, and the other is the extreme superclean regime $\Omega_0\tau \gg 1$ in which all levels are well separated and the dissipation is small. Depending on the energy scales explored in terms of temperatures and applied fields, these systems can potentially show very different behaviors for the T, H and τ dependencies of η [63, 69, 70].

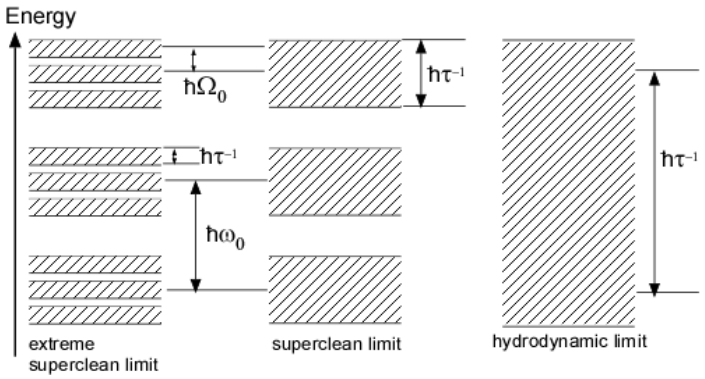

Figure 2.10: Bound levels energy spacings in the vortex cores of s-wave superconductors in the extreme superclean limit $\Omega_0\tau \gg 1$ (*left panel*), superclean limit $\Omega_0\tau \ll 1$ (*center panel*) and hydrodynamic limit $\tilde{\omega}_0\tau \ll 1$ (*right panel*).

2.5 Vortex pinning

In real superconductors material inhomogeneities can locally modify the spatial distribution of the magnetic field or of the order parameter ψ, in such a way that they become preferential sites for fluxons. Electromagnetic pinning can appear when the supercurrent distribution is disturbed by non-conducting defects or vacuum/superconductor boundaries: usually these interactions are small in HTCS and disappear soon by increasing the field [71]. Core pinning is usually more effective: it arises whenever a local depression of ψ —caused by impurities, lattice defects (point like or extended), or thickness non uniformities along the fluxon axes— entails a loss of condensation energy which can be partially restored if a fluxon sticks to it. Considering the whole fluxon system, it is important to recognize that if it were perfectly periodic and rigid the average effects of random pinning centers would be vanishingly small. Pinning forces therefore arise from both the fluxon elasticity and from the interaction between fluxons and pinning sites [6, 64]. In general, vortex phases, direction and intensity of $\mathbf{B}$, kind and distribution of pinning sites are all features affecting pinning forces and energies.

The overall pinning effect can be described in terms of a local pinning potential $U(\mathbf{r}, B)$. Fluxons prefer to occupy the pinning potential minima of U (see panel (a) of figure 2.11): any displacement from these equilibrium positions gives rise to a restoring force on the fluxon. The B-dependence of the pinning potential U can be appreciated by resorting to the distinction between individual and collective pinning, following [64]. The former is present at low fields, giving low fluxon concentrations: in this case there are more

pinning sites than fluxons so that the pinning potential do not depend on fluxon concentration, i.e. on field. The latter case, related to higher fields, arises when many close-packed fluxons collectively interact with the same pinning site: in this case the intensity of the interaction depends on their number thus acquiring a field dependence.

By applying an external current density J, the pinning potential tilts in the direction of the current, thus asymmetrically lowering the potential barriers experienced by the fluxon (panel (b) of figure 2.11). When J approaches J_c the potential is so tilted that fluxons can freely flow in the current direction, reaching the flux flow regime (panel (c) of figure 2.11).

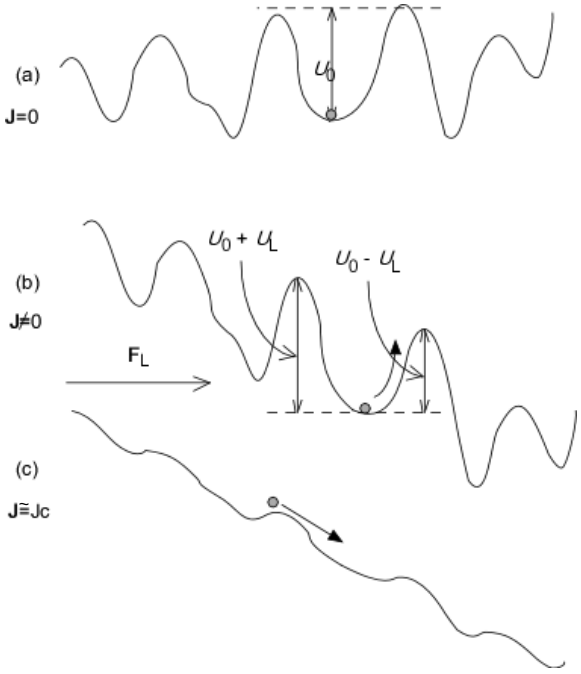

Figure 2.11: (a): fluxon in a minimum of the pinning potential U in absence of external currents.(b): pinning potential U tilting due to external current density J. (c): pinning potential U unidirectionally levelled by $J \sim J_c$.

In addition to the Lorentz force f_L due to an external current, also thermal fluctuations can induce fluxon movement over the pinning potential background, potentially allowing for fluxon jumps between energy minima. The Anderson and Kim model for *flux creep* [72] describes this effect in terms of a thermally activated jump rate:

$$\nu = \nu_0 e^{-U_0/(k_B T)} \tag{2.5.1}$$

where ν_0 is the process characteristic frequency and U_0 is the height of the energy barrier. An estimate for the energy scale of U_0 is the loss of condensation energy $\frac{1}{2}\mu_0 H_c^2 d^3$ due to point-like defects of linear dimension d. Their effectiveness in pinning a fluxon core of radius $\sim \xi$ is maximum if $d \approx \xi$, since $d < \xi$ would give smaller energy gains while $d > \xi$ would give a residual movement freedom to the fluxon. Therefore, $U_0 \sim \frac{1}{2}\mu_0 H_c^2 \xi^3$. In absence of any external driving current, the jump rate is isotropic giving a zero net fluxon movement. The application of a current density J, on the other hand, determines an asymmetrization of the energy barrier by a term $U_L \propto J$ so that the net jump rate in the current direction is:

$$\nu = \nu_0 e^{-(U_0 - U_L)/(k_B T)} - \nu_0 e^{-(U_0 + U_L)/(k_B T)} = 2\nu_0 e^{-U_0/(k_B T)} \sinh \frac{U_L}{k_B T} \quad (2.5.2)$$

which reduces to $\nu_0 e^{-(U_0 - U_L)/(k_B T)}$ if $U_0 \simeq U_L$. In traditional superconductors, having higher ξ and lower T_c, the ratio $U_0/(k_B T)$ is usually large: flux creep can appear only if the Lorentz force is sufficiently high to nearly overcome the barrier, i.e. for $J \sim J_c$. In HTCS, on the other hand, $U_0/(k_B T)$ can be quite small: flux jumps giving thermal activated flux flow (TAFF) can arise also for currents $J \ll J_c$, giving an activated resistivity $\rho \sim e^{-U_0/(k_B T)}$ as obtainable from last member of equation (2.5.2) for $U_L \ll k_B T$ and considering the fluxon velocity $v_L \propto \nu$.

It is worth concluding with a remark concerning the concept of "irreversibility line", involved in electrical transport experiments. The two main regimes above mentioned, flux creep and flux flow, roughly correspond to lower and higher electrical transport dissipation regimes. Indeed, in HTCS in dc measurements one sharply passes from one to another by changing the field H or the temperature T. In particular, the resistivity ρ rather sharply changes from $\rho \simeq 0$ to $\rho \neq 0$ by increasing H or T. The abrupt change allows to identify a precise line in the (T, H) plane which is usually referred to as "irreversibility line". Its name comes from magnetization experiments, in which it divides irreversible magnetization regions, where pinned vortices give residual trapped flux, from reversible magnetization regions (see figure 2.12). This line is usually interpreted as separating different phases of the vortex matter. In measurements at finite frequencies, on the other hand, crossing between different vortex mobility regimes is less marked, so that the irreversibility line, or the underlying vortex phase transitions invoked in its interpretation, can be less visible.

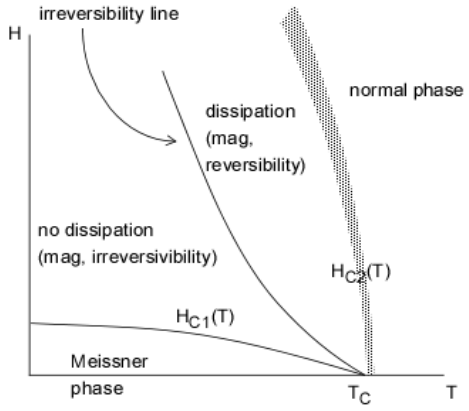

Figure 2.12: (T,H) phase diagram for HTCS showing the irreversibility line.

2.6 Simple model for vortex resistivity

A simple model for the vortex electrodynamic response at finite frequency is hereby presented in order to introduce a few important quantities. Many of the effects previously described (current driven fluxon movement, fluxon viscosity and pinning potential) are taken into account. QP and superfluid contributions and creep phenomena are neglected. Independently pinned vortices are considered and the equation of motion for the displacement $\mathbf{u}$ from the equilibrium position is written in the elastic approximation[7]:

$$\eta\dot{\mathbf{u}} + k_p\mathbf{u} = \mathbf{f_L} \tag{2.6.1}$$

where k_p is the *pinning constant* (per vortex unit length), also called *Labusch parameter*. The term $k_p\mathbf{u}$ represents the pinning force written in the limit for small displacements: $k_p = d^2U(u)/du^2|_{u=0}$. At microwave frequencies this limit is well justified since the vortex maximum displacement caused by microwave fields is typically ~ 1 Å[80]. Considering an alternating current density $\mathbf{J}e^{\mathrm{i}\omega t}$, with frequency $\nu = \omega/(2\pi)$, perpendicular to the static magnetic induction $\mathbf{B}$, the above equation can be rewritten as:

$$\left(\eta + \frac{k_p}{\mathrm{i}\omega}\right)\dot{\mathbf{u}} = \mathbf{J}\times\mathbf{\Phi}_0 \tag{2.6.2}$$

By right-multiplying both terms by $(\mathbf{B}\times)$ and recalling that $\mathbf{E} = \mathbf{B}\times\dot{\mathbf{u}}$ (2.3.5), one obtains $(\eta + k_p/(\mathrm{i}\omega))\mathbf{E} = \mathbf{J}B\Phi_0$ and then, by rearranging and projecting

[7]The vortex mass is usually neglected [75, 76], although this is still a debated topic [77, 78, 79].

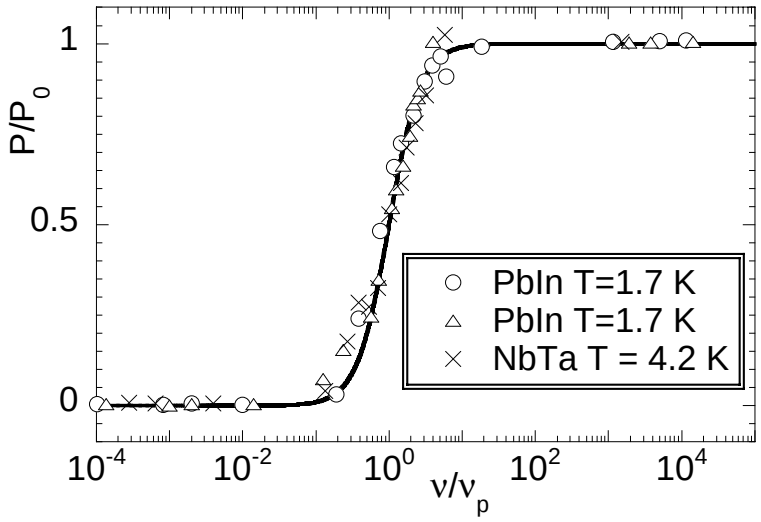

Figure 2.13: Normalized dissipated power in type-II superconductors at $H = \frac{1}{2}H_{c2}$ as a function of the measuring angular frequency normalized to ν_p (replotted from [81]) and fit by equation (2.6.3). $\nu_p = 3.9$, 5.1, 15 MHz [81].

it in scalar form, the Gittleman and Rosemblum (GR) [81] expression for the complex vortex resistivity is obtained:

$$\rho_{vGR} = \frac{\Phi_0 B}{\eta} \frac{1}{1 - \mathrm{i}\frac{k_p}{\eta\omega}} = \rho_{ff} \frac{1}{1 - \mathrm{i}\frac{\omega_p}{\omega}} \tag{2.6.3}$$

where the last equality defines the so-called *flux-flow resistivity*, $\rho_{ff} = \frac{\Phi_0 B}{\eta}$, and the *depinning frequency* (sometimes called "pinning frequency") $\nu_p = \omega_p/(2\pi)$, with $\omega_p = k_p/\eta$. As far as the B field dependence is concerned, it is immediately seen that in the hypothesis of B-independent η and k_p, the obtained fluxon resistivity is *linear* in B, in both its real and imaginary components. The frequency dependence is depicted in figure 2.13 along with the fitted data for the dissipated power ($\propto \Re(\rho_{vGR})$) in thin superconducting films as presented in the seminal paper by Gittleman and Rosenblum [81].

This simple model was then very successful in the interpretation of the data in low-T_c superconductors. Nevertheless, neglected terms correspond exactly to those phenomena that are enhanced in HTCS: flux creep and QP excitations. It is then useful to consider also those contributions.

2.7 Quasiparticles in nodal superconductors

The contribution of the charge carriers, QPs and Cooper pairs, to the electrodynamic response can be particularly important in nodal superconductors,

since zero-energy QPs are more easily excited by the energy perturbation due to vortices. In fact, Cooper pair breaking determined by the external magnetic field modifies the normal and superfluid concentrations to be considered in the two fluid model. For my purposes, being interested in small energy excitations, it is sufficient to determine how the DOS at the Fermi level (E=0), $N(0)$, is modified, computing its spatial average across the vortex system (supposed to be motionless). The evaluation can be easily performed for s-wave superconductors in the dirty limit: roughly speaking, the local DOS is zero outside vortex cores and N_F (DOS of the normal state at the Fermi level) inside the cores. The DOS averaged over the fluxon unit cell $\propto a_{FL}^2$ is simply:

$$N(0) = N_F \frac{2\pi\xi^2}{a_{FL}^2} \cong N_F \frac{B}{B_{c2}} \propto B \tag{2.7.1}$$

where ξ is expressed in terms of B_{c2} using (2.1.10) and $a_{FL} \cong \sqrt{\Phi_0/B}$.

In d-wave superconductors the DOS of both the localized QPs inside vortex cores, arising from the anomalous branch, and of the delocalized nodal QP have to be considered. Volovik [82] showed that these two contributions, summed over the whole vortex unit cell and respectively indicated with N_{loc} and N_{deloc}, can be written as:

$$N_{loc} \sim N_F \xi \min(a_{FL}, \lambda) / \ln \frac{\min(a_{FL}, \lambda)}{\xi} \tag{2.7.2}$$

$$N_{deloc} \sim N_F \xi \min(a_{FL}, \lambda) \tag{2.7.3}$$

N_{deloc} gives the dominant contribution to the overall DOS. The averaged DOS over the vortex cell can therefore be computed. Considering $\lambda \gg a_{FL}$ (justified in HTCS for the most part of the mixed state) one has:

$$N(0) = \frac{N_{deloc}}{a_{FL}^2} = c N_F \sqrt{\frac{B}{B_{c2}}} \propto B^{1/2} \tag{2.7.4}$$

with c being a factor of the order of unity. In [83] the $\sqrt{B}$ dependence against varying temperature was confirmed for clean HTCS. The inclusion of impurity effects [84] gave a generalized B^α dependence with $\alpha \sim 0.5$. Introducing a reduced field $b = B/B_{pb}$, where B_{pb} is a pairbreaking field that absorbs all the numerical factors, I then propose to extend the two fluid model for nodal superconductors by including the above presented field dependence in charge carriers concentrations. Therefore, the fractional fluid concentrations x_n and x_s can incorporate both the reduced field b and reduced temperature t dependencies as follows:

$$x_n = b^\alpha(1-t^k) + t^k \qquad (2.7.5)$$
$$x_s = 1 - x_n = (1-b^\alpha)(1-t^k)$$

where α is exactly or approximately equal to 0.5 depending on the impurity concentration.

Having obtained separately the vortex and charge carriers responses in the mixed state, I now complete the modelling of the electrodynamics of HTCS by introducing a general model capable to take into account both responses.

2.8 Ac electrodynamics in the mixed state

Considering an electromagnetic field incident on a flat interface between a generic medium and a (super)conductor, the response to the field is given by the *surface impedance* [85, 97] (see chapters 3 and 4). In the case of a bulk sample (thick with respect to the fields penetration depth) in the local limit, this quantity can be written in the two equivalents forms:

$$Z_s = \mathrm{i}\omega\mu_0\tilde{\lambda} = \sqrt{\mathrm{i}\omega\mu_0\widetilde{\rho}} \qquad (2.8.1)$$

where $\tilde{\lambda}$ is an appropriate complex screening length and the complex resistivity $\widetilde{\rho} = \mathrm{i}\omega\mu_0\tilde{\lambda}^2$. The complex resistivity $\widetilde{\rho}$ (or equivalently $\tilde{\lambda}$ or Z_s) of a superconductor in the mixed state includes contributions from the moving vortex lattice and from the two types of charge carriers, normal and super. Many models have been developed in order to capture the overall dynamics, having various degrees of complexity [86, 87, 88, 89, 90, 91, 92, 93]. A widely used model was proposed [89] and later extended [94, 95, 96] for various geometries and different reciprocal orientations of the ac and dc fields by Coffey and Clem (CC). The main points in their treatment are hereby recalled:

- all the electromagnetic quantities are exponentially damped in going inside the superconductor according to the complex characteristic length $\tilde{\lambda}$;
- the local two fluid model is used, so that the total current density $\mathbf{J} = \mathbf{J}_n + \mathbf{J}_s$, where $\mathbf{J}_n$ and $\mathbf{J}_s$ represent respectively the normal and superfluid components;
- the supercurrent $\mathbf{J}_s$ is coupled with the oscillating fluxon system through the London equation:

$$\nabla \times \mathbf{J}_s = -(1/\mu_0\lambda^2)\,[\mathbf{B} - \mathbf{B}_\mathbf{v}] \qquad (2.8.2)$$

being $\mathbf{B}$ the total magnetic induction field and $\mathbf{B_v} = \mathbf{\Phi}_0 n_f$ the contribution of the fluxon lattice having a fluxon density $n_f(x,t)$. The above equation is derived by applying the curl operator to the second GL equation (1.2.3) and by averaging it over some intervortex spacings, so that the averaged $\nabla \times \nabla\phi$ term is expressed in terms of the flux quanta Φ_0 carried by the fluxon density n_f. This equation, relating the supercurrents to the fluxon system movements, allows to account for the nonlocal effects arising from this interaction;

- vortices displacement is assumed to be a *linear* function of the *whole* current density $\mathbf{J}$, as given by the equation for the single vortex dynamic (2.6.2) but not limited to that specific model. This assumption, justified by the small vortices displacements at microwave frequencies, implies also a pinning potential independent from the driving current intensity, thus excluding flux creep which arises for $J \lesssim J_c$ (but not linear creep regimes such as TAFF);

- the normal current is $\mathbf{J}_n = \sigma_{nf}\mathbf{E}$, with the electric field $\mathbf{E}$ including the usual vortex induced contribution $\mathbf{B} \times \dot{\mathbf{u}}$.

The system of equations written in this framework is self-consistently solved yielding in the frequency domain (for time dependence $e^{\mathrm{i}\omega t}$):

$$\tilde{\lambda} = \left(\frac{\lambda^2 - (\mathrm{i}/2)\delta_v^2}{1 + 2\mathrm{i}\lambda^2/\delta_{nf}^2} \right)^{1/2} \tag{2.8.3}$$

where, in addition to the usual London penetration depth λ, other two characteristic lengths are introduced: the normal fluid skin depth $\delta_{nf} = (2/\mu_0\omega\sigma_{nf})^{1/2}$ and the vortex penetration depth defined as $\delta_v = (2\rho_v/\mu_0\omega)^{1/2}$. The vortex complex resistivity ρ_v is the response associated with the local vortex-motion induced electric field ($\mathbf{B} \times \dot{\mathbf{u}} = \rho_v \mathbf{J}$) [89].

It is important to note that equation (2.8.3) plays the role of a master equation, since various models can be invoked for the quantities λ, σ_n and ρ_v, thus allowing it to be applied in very wide ranges of magnetic induction B, temperatures T and angular frequencies ω.

For example, λ and σ_n can depend in different ways on the temperature T and field B according to the order parameter symmetry. On the other hand, ρ_v depends on the viscosity and pinning models. In particular, the latter requires choice of the collective or individual pinning (resulting in a field dependent or independent k_p, respectively), of the pinning potential periodicity and of the specific flux creep model. For example, in [89, 90] they considered a model of vortex dynamics including a sinusoidal pinning potential with peak to peak

value $U_0(T)$ and a specific stochastic thermal force —with Gaussian white noise, δ-function correlation and zero average— added to equation (2.6.2). The resulting ρ_v was:

$$\begin{aligned} \Re[\rho_v] &= \rho_{ff}\frac{\epsilon+(\nu/\nu_{vc})^2}{1+(\nu/\nu_{vc})^2} \\ \Im[\rho_v] &= \rho_{ff}\frac{1-\epsilon}{1+(\nu/\nu_{vc})^2}\frac{\nu}{\nu_{vc}} \end{aligned} \tag{2.8.4}$$

where $\epsilon = 1/I_0^2(\bar{u})$ is a creep factor, $\nu_{vc} = \nu_p \frac{1}{1-\epsilon}\frac{I_1(\bar{u})}{I_0(\bar{u})}$ is a characteristic frequency related to the pinning frequency $\nu_p = \omega_p/(2\pi)$, $\bar{u} = U_0(T)/(k_B T)$, $I_0(\bar{u})$ and $I_1(\bar{u})$ are modified Bessel functions. The creep factor, whichever the pinning strength, ranges from $\epsilon = 0$, which corresponds to no flux creep, to $\epsilon = 1$. In the $\epsilon = 0$ limit $\nu_{vc} = \nu_p$ and equation (2.8.4) gives the GR result (2.6.3). For $\epsilon = 1$, $\rho_v = \rho_{ff}$, that is thermal energy is so high that the flux lines do not sense the pinning potential and are free to move. Focusing on the frequency dependence, it is readily seen that for $\nu \ll \nu_p$ the imaginary part of ρ_v dominates over the real part (vortex response mainly reactive), with wider fluxon oscillations in the pinning potential minima (left panel of figure 2.14). For $\nu \gg \nu_p$, on the other hand, the response is mainly dissipative with smaller vortex oscillations (right panel of figure 2.14).

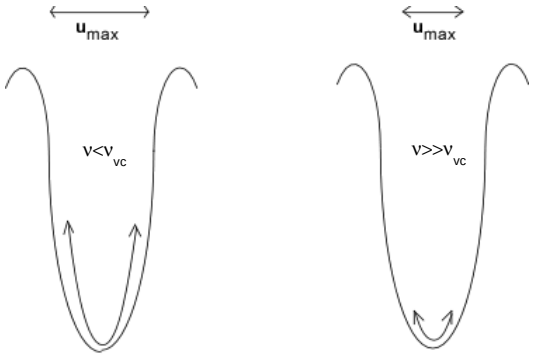

Figure 2.14: Fluxon oscillations inside pinning potential minimum. *Left panel*: low frequency case with wide oscillations; *right panel*: high frequency case with small oscillations.

With the aid of this simple model for the vortex motion contribution ρ_v and by further assuming $\omega\tau_{QP} \ll 1$ so that σ_n is real, the master equation (2.8.3) can be cast in a form in which all the quantities are explicitly accounted for, giving

a useful overview of all the contributions to the real and imaginary components of the complex resistivity:

$$\begin{aligned}
\rho_1 &= \frac{1}{1+(\nu/\nu_s)^2}\left[\rho_{ff}\frac{\epsilon+(\nu/\nu_{vc})^2}{1+(\nu/\nu_{vc})^2}+\frac{\nu}{\nu_s}\left(\frac{\nu}{\nu_s\sigma_{nf}}+\rho_{ff}\frac{1-\epsilon}{1+(\nu/\nu_{vc})^2}\frac{\nu}{\nu_{vc}}\right)\right] \\
\rho_2 &= \frac{1}{1+(\nu/\nu_s)^2}\left[\frac{\nu}{\nu_s\sigma_{nf}}+\rho_{ff}\frac{1-\epsilon}{1+(\nu/\nu_{vc})^2}\frac{\nu}{\nu_{vc}}-\frac{\nu}{\nu_s}\left(\rho_{ff}\frac{\epsilon+(\nu/\nu_{vc})^2}{1+(\nu/\nu_{vc})^2}\right)\right]
\end{aligned} \tag{2.8.5}$$

in which it is used $(\lambda/\delta_{nf})^2 = \nu/\nu_s$, with $\nu_s = 1/2\pi\mu_0\sigma_{nf}\lambda^2$.

A particularly interesting limiting form of these expressions is the high frequency limit $\nu \gg \nu_{vc}$:

$$\begin{aligned}
\rho_1 &\simeq \frac{1}{1+(\nu/\nu_s)^2}\left[\rho_{ff}+\frac{1}{\sigma_{nf}}\left(\frac{\nu}{\nu_s}\right)^2\right] \\
\rho_2 &\simeq \frac{\nu/\nu_s}{1+(\nu/\nu_s)^2}\left(\frac{1}{\sigma_{nf}}-\rho_{ff}\right)
\end{aligned} \tag{2.8.6}$$

In this limit vortices make very short displacements from their equilibrium positions. Despite the possibly finite pinning, the vortex response is equivalent to free flux flow motion. Specific pinning properties represented by the pinning constant k_p, which does not appear, are therefore unimportant and the response depends only on ν_s, ρ_{ff} and σ_{nf} (with ρ_{ff} containing the η), which are quantities related to the intrinsic properties of the superconductor.

2.9 Summary

In this brief survey it was shown how the microwave mixed state electrodynamics can be particularly complex. The effects which concur in defining it can be of both intrinsic (material-related) and extrinsic (sample-related) origin.

Concerning intrinsic effects, QP dynamics and vortices dissipation, respectively described in terms of normal fluid conductivity σ_n and viscosity η, give important information on the QP density of states, including both localized (inside vortices cores) and delocalized contributions. In particular, concerning delocalized QP, I have proposed an extension of the two fluid model which includes the field pairbreaking effect for nodal superconductor.

Extrinsic effects are mainly represented by pinning phenomena, described when possible with the pinning constant k_p. They are determined by the

specific type and distribution of material defects in the sample. However, by resorting to sufficiently high frequencies in the microwave range, vortex motion becomes a pure flux flow motion: in this case only intrinsic properties are observed, thus allowing to concentrate on the fundamental physics of the HTCS.

The above considerations justify the use of microwave measurements for the study of HTCS presented in this thesis. The following chapter is devoted to the description of the experimental technique used.

Chapter 3

Measurement techniques and experimental setup

This chapter is devoted to the description of the technique used for the measurement of the microwave surface impedance of superconductors. After a brief survey of various techniques commonly used, I focus on the principles of the resonant technique used in this thesis giving emphasis on the derivation of the physical quantities from measured data. I will then describe the existing metallic cavities (operating at 24 and 48 GHz). Lastly, section 3.6 deals with the technical part of the work carried on in this thesis: the design, development and setup of a dielectric resonator. Comparison between the performances of the dielectric resonator and the pre-existing cavities concludes this chapter.

3.1 Introduction

The portion of the electromagnetic spectrum in the range 1–100 GHz is broadly referred to as "microwave radiation". In this frequency range the electromagnetic response is naturally given by complex response functions. The main physical quantity directly measurable in microwave experiments is the *effective surface impedance* Z_s. Considering an electromagnetic field incident on a flat interface between a generic medium and the superconductor, the effective surface impedance is defined as $Z_s = E_{//}/H_{//}$, where $E_{//}$ and $H_{//}$ are the components of the electric and magnetic field parallel to the surface, respectively. In the case of semi-infinite (super)conducting materials Z_s is given in the local limit by the well known expression [85, 97]:

$$Z_s = R_s + \mathrm{i}X_s = \sqrt{\frac{\mathrm{i}\omega\mu_0}{\tilde{\sigma}_s}} \tag{3.1.1}$$

where ω is the angular frequency of the electromagnetic field, $\tilde{\sigma_s}$ is the (super)conductor complex conductivity, R_s and X_s are the surface resistance and reactance which account for dissipation and energy storage, respectively. In thin films the electromagnetic field propagates through the film reaching the underlying substrate and any other supporting layer. In this case, both the finite thickness of the film and the effect of the substrate have to be considered, giving a more complicate expression of the effective surface impedance (extensively discussed in chapter 4). Later on in this chapter I will refer to Z_s as the effective surface impedance, leaving to the next chapter the discussion of the relation between Z_s and the conductivity.

Various approaches are possible for the measurement of Z_s. Resonant techniques, by definition, force to work at fixed frequencies. The main advantage of these methods is given by the high achievable sensitivity. Wide band techniques, such as Corbino disk and bolometric methods, allow to perform measurements over a wide and nearly continuous frequency range, but with intrinsically lower sensitivity. In the following paragraphs I present a short review of resonant and wideband methods in order to highlight their main advantages, disadvantages and technical issues (see also [98]).

3.2 Microwave measurements

In electromagnetic resonators, whichever their structure, the resonant condition is achieved for fixed frequencies only, at which (quasi)stable field configurations exist. These configurations are indicated as modes and are given by the solution of the Helmholtz equation with proper boundary condition given by the resonator geometry (see, for example, [97]). At a given resonant frequency ν_0, the electromagnetic fields of the corresponding mode filling the volume of the structure can be orders of magnitude stronger than those excited in the same structure, out of resonance, by the same external source. Part of this energy is lost, by internal dissipation or external losses, in every oscillation cycle: at dynamic equilibrium the coupling with an external power source grants a constant power level. Resonators are treated in detail in appendix A. Here one only introduces the unloaded quality factor Q_U (where "unloaded" means that external losses are not taken into account) as a measure of this process:

$$Q_U = \frac{2\pi\nu_0 W}{P} \tag{3.2.1}$$

where W is the total stored energy and P is the dissipated power (both averaged over time). Including also the external losses P_E, a loaded quality factor

Q_L can be defined as follows:

$$Q_L = \frac{2\pi\nu_0 W}{P + P_E} \tag{3.2.2}$$

Resonators can be operated in reflection or transmission modes. In the reflection mode the resonator is coupled to the external system through one port only: impinging and reflected microwaves are measured from the same line giving ν_0, Q_L and the coupling coefficient β [97] which allows to compute $Q_U = Q_L/(1+\beta)$. In the transmission mode the resonator is fed through an input port (with coupling coefficient β_1) and a transmitted signal is picked off from a distinct output port (with coupling coefficient β_2), so that $Q_U = Q_L/(1+\beta_1+\beta_2)$. Various methods for the determination of Q_L and β are used (see [99] and references therein). The transmission method usually can achieve higher signal-to-noise ratios, but it usually requires more sophisticate measurement procedures (based on vector network analyzer) in order to take into account all system error contributions (including coupling asymmetries and crosstalks). Reflection operated resonators are more compact (since they require a single coupling mechanism) and more suitable to scalar measurements, although they are potentially more affected by line calibration issues.

The quality factor Q_U and the resonant frequency ν_0 give respectively the real and imaginary parts of the surface impedance of the (super)conducting elements inserted in or making part of the resonator. In general, for a superconducting sample of surface impedance Z_s, the following relation holds:

$$\Delta R_s + \mathrm{i}\Delta X_s = G_s\left(\Delta\frac{1}{Q_U} - 2\mathrm{i}\frac{\Delta\nu_0}{\nu_0}\right) - background \tag{3.2.3}$$

where $\Delta A = A(x) - A(x_{ref})$ represents the variation of the generic physical quantity A with respect to the reference value $A(x_{ref})$ caused by the variation of the operating parameter x (which can be the temperature, the externally applied magnetic field or the intensity of the microwave fields excited in the resonator). G_s is a geometrical factor and represents the contribution of the sample to the total losses and reactive energy storage. By suitable calibration of the background, Z_s of the superconductor can be determined. In sections 3.2.1–3.2.3 some of the resonators used for the measurement of Z_s in superconductors are described.

Non-resonant techniques allow for the determination of the complex conductivity in a wide range of frequencies. A typical method is based on the propagation of microwaves through a thin HTCS film and on the measurement of the corresponding fractional transmitted and reflected power (i.e. the

transmission and reflection coefficients, respectively). The impinging electromagnetic wave can propagate in free-space [100] or in waveguides [101] or coaxial cables [102]. Another wide band method is bolometry, which allows to measure microwave losses, therefore being limited to the real part of Z_s. Generally, these techniques are characterized by a smaller sensitivity with respect to resonant approaches, which makes critical a proper calibration of the system.

3.2.1 Cavities

Cavities are commonly used resonators. As the name itself indicates, they are enclosures delimited by conducting walls. Modes are classified as TE or TM if, respectively, the electric or magnetic field are purely transverse with respect to the axis of the structure. Geometries with a multiple connected transversal section are able to sustain also TEM modes in which both fields are purely transverse.

Cavities usually have simple geometries: cylindrical, often used because of their higher Q_U, elliptical [103], a version of the cylindrical type allowing a superior spurious mode rejection, rectangular [104], having low Q_U but able to sustain unidirectional microwave currents, and coaxial, which sustain TEM modes allowing easier frequency tuning and the exploration of the low frequency range [105]. Metallic cavities can work in a wide range of frequencies, between 3 and 150 GHz [29, 65, 106, 107, 108, 109, 110].

The main source of power losses in cavities is the ohmic dissipation of the microwave currents induced on the metallic walls. Any filling dielectric gives an additional contribution due to dielectric polarization losses. The simplicity of these systems allows for a precise determination of the specific mode existing at a given resonant frequency. Electromagnetic field configurations, current distributions and geometrical factors can be calculated analytically.

The sample to be characterized is integrated or inserted inside the cavity using two alternative approaches (figure 3.1)[111, 112]: the *surface perturbation* (also referred to as *end-wall replacement*) or the *volume perturbation*.

In the end-wall replacement method one or more conducting surfaces of the resonator are replaced by the samples. Usually in cylindrical metallic cavities the sample substitutes for one base of the cylinder. This surface perturbation approach is particularly suitable when the sample has a large flat surface, such as in thin (epitaxial) films, thick films or pellets.

Through suitable adjustments, single crystals can be examined at the expense of a substantial decrease of sensitivity [109]. For small samples the volume perturbation is more appropriate: the sample is put inside the volume of the cavity in the antinodes of magnetic field in order to maximize sensitiv-

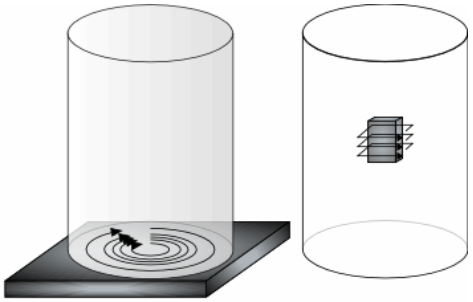

Figure 3.1: A cylindrical cavity with end-wall perturbation by a flat sample (*left panel*) and a volume perturbation by a bulk sample (*right panel*). Arrows represent microwave currents induced on the samples.

ity. Also thin films can be measured by means of this technique, although the antinodes of the electric field can be a better choice [113]. A few other issues of these two methods can be addressed, either mainly sample-related or mainly technique-related:

- sample preparation: both techniques are non-destructive, since they do not require particular preparation or alteration (patterning, for example) of the sample;
- sample edge effects: the surface perturbation approach, by proper choice of the resonant mode, allows to probe the center of the sample film thus minimizing edge effects, which inevitably affects the smaller samples used for the volume perturbation;
- sample positioning: the volume perturbation is sensitive to systematic errors arising from sample positioning, thermal expansion [114] and orientation of anisotropic samples;
- cavity background calibration: by volume perturbation, a fixed background is obtained if the cavity is kept at a fixed (low) temperature. The sample temperature can be independently changed by mounting it on a "hot-finger";
- cavity background reduction: in the hot-finger configuration the cavity can be made up of a superconductor, thus increasing Q_U values up to 10^8 [115] (corresponding to R_s resolution of $\sim 1\mu\Omega$) thanks to the reduction of background losses. Obviously, measurements in an external static magnetic field cannot be performed.

3.2.2 Dielectric resonators

If compared to typical cavities, dielectric resonators give a significant reduction of background losses (and thus a greater sensitivity) and of size (indeed, cavity size is a problem in low frequency applications). In dielectric resonators the electromagnetic fields are confined by using the "lens" effect of a high-ε_r material enclosed in a low-ε_r material (air or vacuum). A typical dielectric resonator of this kind is based on a cylindrical dielectric rod placed between two conducting plates (Hakki-Coleman resonator [116]), laterally shielded by additional conducting walls (left panel of figure 3.2). A variation is the so-called open-ended resonator [117], having one or both plates spaced out from the dielectric rod (right panel of figure 3.2).

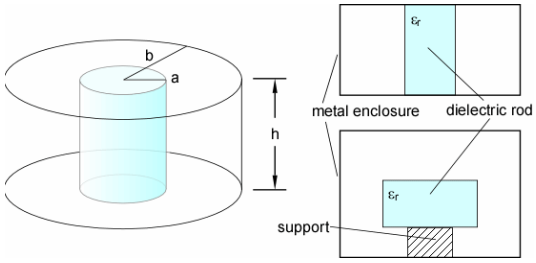

Figure 3.2: Dielectric resonator. *Left panel*: shielded Hakki-Coleman resonator. *Right panel*: section view of a Hakki-Coleman (upper part) and open-ended (lower part) resonators.

In order to find the resonating modes, one has to solve a more complex electromagnetic problem than in cavities. Peculiar to dielectric resonators is the existence of additional modes often referred to as hybrid electromagnetic (HEM), with non zero axial components of both the magnetic and electric fields[1]. In particular, open-ended configurations do not allow for closed form expressions, requiring in general finite-element computation. Specific cases, with the azimuthal symmetric TE modes, can be treated with the simpler approach of the incremental rule [120].

By appropriate design, the power dissipation in these resonators mainly originates from the dielectric losses[2], thus giving higher Q_U (up to 10^6 with

[1]High azimuthal-index HEM modes, called whispering gallery modes, are widely used for accurate dielectric material characterization[118, 119].

[2]The relative weight between dielectric and ohmic losses depends on the resonator structure, on the presence/absence of lateral metallic shielding, on the ratio between dielectric and air filled volumes, on the magnitude of ε_r and on the resonant mode. The balance between these elements determines a classification of resonators which can range from classic

both superconducting plates [122]) compared to cavities. As a consequence, dielectric resonators are largely diffused for the measurements of HTCS surface resistance [123, 124].

The small size of the dielectric resonator allows to measure smaller samples (or to use smaller and more efficient cryostats and magnets). The rigidity of the assembly improves mechanical stability against temperature changes, if compared to empty metallic cavities. However the lower sensitivity of metal cavities allows for the measurements of the entire normal-superconducting transition, while in dielectric resonators the high resistance of the normal state of an HTCS is a so strong perturbation of the resonant mode that the resonant signal is lost.

3.2.3 Planar resonator

Planar resonators such as microstrips [125, 126] or coplanar resonators [127, 128] (see figure 3.3) can give typical Q_U of the order of 10^4, being the fundamental mode mainly in the 1–10 GHz range. Microwave currents are particularly strong at the edge of the central superconductor line. As a consequence, these resonators present high sensitivity to field or vortex penetration, which makes them an interesting tool in studying non-linear effects [129].

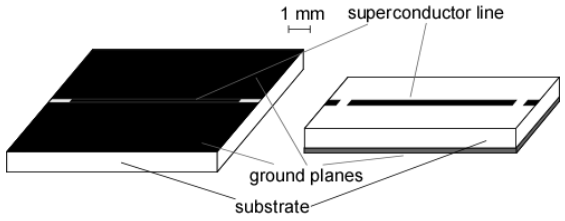

Figure 3.3: Examples of planar resonators. *Left panel*: linear coplanar resonator with fundamental resonance at 7.95 GHz (gap between line and ground planes not in scale) [127]. *Right panel*: microstrip resonator with fundamental resonance at 5 GHz [125].

These resonators are very interesting from a technological point of view because they constitute the building blocks of microwave filters. Therefore HTCS characterization through this approach is immediately applicable to the evaluation of the performances of a real device. Their use in the study of fundamental physical properties presents however a few drawbacks:

cavities to "pure" dielectric resonators passing through the intermediate situation, often referred to as "dielectric loaded cavities"[121]. For my purposes this distinction is not relevant so that I will refer to all these classes as "dielectric resonators".

- the technique is destructive, in the sense that it requires patterning. As a consequence, the use of the same sample with other experimental techniques can be prevented;

- the photolithographic patterning can produce rounded (instead of sharp) sample edges and damages. Since the resonant structure is rather small and microwave currents are concentrated on film edges, such damages can strongly affect the measured response. For example, artifacts on the temperature behavior of Z_s can show up [130];

- in a static magnetic field [129], the high aspect ratio of these structures tends to concentrate the magnetic flux lines on the edges, thus determining non uniform film penetration and possibly significant irreversibility phenomena.

3.2.4 Corbino disk

The Corbino geometry was originally devised by Corbino [131] for the study of metals and adapted to the study of HTCS by Booth et al [102]. It consists of a coaxial cable short-circuited on the HTCS thin film, usually backed by a metallic plate in order to prevent radiation losses (figure 3.4).

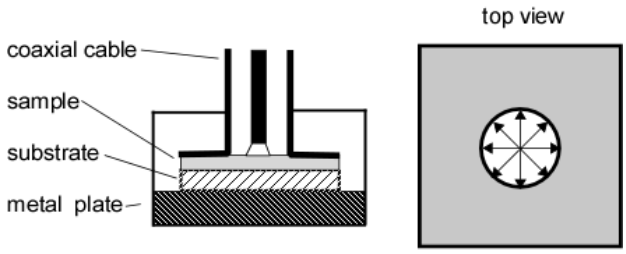

Figure 3.4: Corbino disk setup. *Left panel*: section view of the coaxial cable short-circuited on the sample. *Right panel*: radial pattern of microwave currents induced on the sample.

From the measurement of the (complex) reflection coefficient at the input of the cable one can obtain the reflection coefficient Γ_0 at the sample and then the sample surface impedance by means of the following expression [85]:

$$Z_s(\nu) = Z_0 \frac{1+\Gamma_0(\nu)}{1-\Gamma_0(\nu)} \tag{3.2.4}$$

where Z_0 is the characteristic impedance of the material filling the cable. The coaxial cable supports the TEM mode, characterized by radial currents decreasing with radius r as $1/r$, in a frequency range that goes from dc up to the cutoff frequency of the cable. Typical frequency ranges span from a few MHz up to a few tens of GHz [102]. The essential and more challenging issue is the proper line calibration (which involves complex quantities), since the line contribution to the measured reflection coefficient is comparable with the sample one. In particular, calibration is critical for the part of the line inside the cryostat. In fact its response changes with time, because of varying temperature and varying temperature profiles along the cable. Thus, a full calibration is impossible. Different solutions to this problem have been devised by various groups [102, 132, 133, 134].

3.2.5 Transmission measurements

Another wide band method is based on the measurement of transmitted power through thin films placed inside waveguides [101]. The measured quantity is the total transmission coefficient Υ, defined as the ratio between transmitted and incident electric fields. In the common case of waveguides operated in the TE_{01} mode, with a thin film normal to the structure axis, the transmission coefficient Υ is linked to the HTCS complex conductivity $\tilde{\sigma}$ by the following approximated expression [135]:

$$\Upsilon = \frac{2n}{Z_g d\tilde{\sigma}\,(n\cos k_g l + \mathrm{i}\sin k_g l)} \tag{3.2.5}$$

where d is the film thickness, l and n are the substrate thickness and refractive index, respectively, Z_g and k_g are the mode impedance and propagation constant, respectively. In spite of the analogy with the Corbino technique, there are many practical differences between the two methods. With respect to a coaxial cable, a waveguide presents much lower losses but supports much smaller frequency ranges, which never cover a full order of magnitude. Although electrical contact is not an issue, many limitations are necessary: the film and substrate must be uniform in thickness; film thickness has to be limited in order to allow sufficient microwave transmission through it; care must be taken in order to reduce power leakage from the sample edges; leakage can also be caused by microcracks, pinholes or normal regions. In the microwave frequency range and with HTCS films this technique is therefore not widely used.

3.2.6 Bolometry

The bolometric method is based on the measurement of the temperature variations due to the power dissipated by a generic (super)conductor of surface S exposed to a microwave field of tangential component $H_{//}$. The dissipated power P_{diss} is directly proportional to the sample surface resistance as follows:

$$P_{diss} = \frac{1}{2} R_s \int_S |\mathbf{H}_{//}|^2 dS \tag{3.2.6}$$

This method was applied for the first time to superconducting Al [136], using for the measurement a whole segment of a waveguide made of Al. The application to small HTCS samples has required improvements of various experimental aspects. The sample shape and positioning have to be chosen in order to minimize demagnetization effects and mixing of the elements of the anisotropic conductivity tensor. Care must be taken in the generation of a uniform microwave field across the sample. Residual uncertainties, along with other sources of systematic errors, make the calibration of the system critical. The preparation of reference samples, with shape identical to the sample under study and with known R_s, is then another important issue which involves also proper material choice. The low levels of dissipated power involved, especially for low frequencies (below 20 GHz) and small samples, require high sensitivity bolometers, optimized heat sinks of small dimensions and great care in controlling all the thermal inputs to the system. In any case, signal to noise ratio usually limits the measurement temperature below 10 K, thus preventing Z_s measurements over large temperature ranges and specifically excluding the transition region in HTCS. An example of this technique optimized for $1 \times 1 \times 0.01$ mm^3 YBCO single crystal has been reported in [137], for measurements in the range 0.6 – 20 GHz, with a resolution of 1.5 pW corresponding to $\sim 1\mu\Omega$ at a few K.

In conclusion, this brief overview has highlighted advantages and disadvantages of various selected microwave techniques.

The need to resolve the entire superconducting transition, the requirements of a sensitivity high enough to study the vortex state for $H \ll H_{c2}$, the small dimensions required by the electromagnet determined the choice of combined measurements by metal cavities and dielectric resonators. In the following, I describe the common aspects of the measurement technique, the experimental setups and the design and realization of the dielectric resonator.

3.3 Measurement technique

In this thesis three resonant systems have been employed: two cylindrical metal cavities, operating at 24 GHz and 48 GHz, and a shielded Hakki-Coleman dielectric resonator, developed as part of this thesis as an upgrade of the 48 GHz cavity. A few measurements have been also performed with the Corbino disk facility at University "La Sapienza" in Rome [132]. After the explanation of the measurement principles, I will firstly and more extensively describe the 48 GHz line, where most of the data were taken. Then a brief description of the 24 GHz line will be given. The design and realization of the dielectric resonator, along with the setup upgrade devised to assure its integration in the pre-existing microwave line, will be the subjects of the last section.

3.4 Principles of measurement

An electromagnetic resonator (whether cavity or dielectric resonator) used in the end-wall replacement configuration allows to determine the surface impedance Z_s of a superconducting sample by means of the following expressions (rearranged from (A.2.11) and (A.2.12) presented in appendix A.2):

$$R_s(T,H) = \frac{G_s}{Q_U(T,H)} - G_s\left[\left(\frac{1}{G_0} - \frac{1}{G_s}\right)R_m(T) + \frac{1}{Q_d(T)}\right] \tag{3.4.1}$$

$$\begin{aligned}\Delta X_s(T,H) = X_s(T,H) - X_s(\bar{T},\bar{H}) = -2G_s\frac{\nu_0(T,H)-\nu_0(\bar{T},\bar{H})}{\nu_0(\bar{T},\bar{H})} + \\ +2G_s\left[\left(\frac{1}{G_0} - \frac{1}{G_s}\right)\left(X_m(T,H) - X_m(\bar{T},\bar{H})\right) + \left.\frac{\nu_0(T)-\nu_0(\bar{T})}{\nu_0(\bar{T})}\right|_{diel}\right]\end{aligned} \tag{3.4.2}$$

where the dependencies on the temperature T and field H are explicitly written. In the expression for X_s, in particular, $\bar{T}$ and $\bar{H}$ represent the reference values of temperature and field with respect to which the variations of X_s are evaluated. In equations (3.4.1) and (3.4.2) three classes of quantities can be identified:

- $Q_U(T,H)$ and $\nu_0(T,H)$ are respectively the measured quality factor and resonant frequency of the resonator incorporating the sample;
- G_0 and G_s are geometrical factors, to be computed from their analytical expressions (see appendix A);

- the terms inside square brackets are background contributions, given by the surface impedance of the metallic walls, $R_m(T) + \mathrm{i}X_m(T)$, by the permittivity of the dielectric rod and by the thermal expansion of the resonator. Here it is important to stress that the background does not depend on magnetic field H but only on temperature. As a consequence, the field induced variations of the surface impedance of the superconductor $\Delta Z_s = Z_s(T,H) - Z_s(T,\bar{H})$ at a fixed T can be directly and exactly determined as

$$\Delta R_s(T,H) = G_s \left(\frac{1}{Q_U(T,H)} - \frac{1}{Q_U(T,\bar{H})} \right) \tag{3.4.3}$$

$$\Delta X_s(T,H) = -2G_s \left(\frac{\nu_0(T,H) - \nu_0(T,\bar{H})}{\nu_0(T,\bar{H})} \right) \tag{3.4.4}$$

  where only G_s has to be calculated.

It should be stressed that, once the background has been evaluated, R_s can be determined in absolute values, where only variations ΔX_s can be experimentally measured. To obtain absolute X_s, one usually assumes a reference point. An example is the assumption of validity of the Hagens-Rubens limit, that is $\Im(\sigma) = 0$ above T_c. This approach has to be used carefully since exceptions can arise due to the peculiar physics of the HTCS [138] or to the electromagnetic configuration [139] (see chapter 4).

Resonator response

The resonators used in this thesis work are operated as one-port elements, i.e. in reflection mode. The coupling mechanism (iris for the cavities and probe for the dielectric resonator) excites the desired resonant. At the same time, it allows internal fields to leak outwards. The corresponding externally dissipated power P_E adds up to the internal losses, resulting in a total loss $P_L = P + P_E$. The corresponding loaded quality factor Q_L is related to the unloaded Q_U through the coupling coefficient $\beta = P_E/P > 0$ as:

$$Q_L = \frac{Q_U}{1+\beta} \tag{3.4.5}$$

In the undercoupled resonators, external losses are smaller than the internal ones and $\beta < 1$ so that Q_L is not too different from Q_U. In overcoupling, $\beta > 1$ and Q_L can heavily decrease: this situation is usually avoided since high external losses mask the internal ones, degrading the signal to noise ratio. In order to maximize Q_L resonators are therefore operated in undercoupling.

Considering a section of the microwave line immediately external to the resonator, the square modulus of the reflection coefficient Γ is given by:

$$|\Gamma(\nu)|^2 = \frac{P_r(\nu)}{P_i(\nu)} \tag{3.4.6}$$

where $P_i(\nu)$ and $P_r(\nu)$ are the (frequency dependent) power reflected by the resonator and incident on the resonator, respectively. In a frequency range near the resonant frequency of the considered mode and far away from other resonances, $|\Gamma(\nu)|^2$ is described by a Lorentzian curve [97]:

$$|\Gamma(\nu)|^2 = 1 - \frac{1 - |\Gamma(\nu_0)|^2}{1 + [2Q_L(\nu/\nu_0 - 1)]^2} \tag{3.4.7}$$

where $|\Gamma(\nu_0)| = (1-\beta)/(1+\beta)$. This function describes a bell-shape function with a maximum $|\Gamma(\nu_0)|^2$ at ν_0 and a fractional full width at half maximum equal to $\Delta\nu_{FWHM}/\nu_0 = Q_L^{-1}$. The resonator parameters can be extracted by making a frequency sweep around the resonant frequency ν_0 of the mode of interest and by fitting the measured $|\Gamma(\nu)|^2$ to equation (3.4.7). The fitting parameters Q_L, ν_0 and β immediately yield the quantities of interest Q_U and ν_0 through (3.2.3).

Line calibration

For obvious reasons, the incident and reflected powers are measured quite far from the resonator. The power P_m measured by the detector and the power P_r reflected by the resonator are therefore different. Their relationship in general would involve a full scattering matrix description of the microwave circuit. Assuming that the microwave circuit has only a frequency dependent attenuation coefficient $k(\nu)$, one has:

$$P_m(\nu) = k(\nu)P_r(\nu) = k(\nu)|\Gamma(\nu)|^2 P_i(\nu) \tag{3.4.8}$$

where the last equality is due to equation (3.4.6). It is clear that, in order to extract $|\Gamma(\nu)|^2$, a calibration of the line is needed. The solution used consists in detuning the resonator through a proper mechanism. Once placed off-resonance, the reflection coefficient $\Gamma(\nu) = -1$. The corresponding measured power $P_m^{'}(\nu)$ is therefore:

$$P_m^{'}(\nu) = k(\nu)|-1|^2 P_i(\nu) = k(\nu)P_i(\nu) \tag{3.4.9}$$

By taking the ratio between $P_m(\nu)$ (equation (3.4.8)) at resonant condition and $P'_m(\nu)$ (equation (3.4.9)) with the resonator detuned one obtains:

$$\frac{P_m(\nu)}{P'_m(\nu)} = \frac{k(\nu)|\Gamma(\nu)|^2 P_i(\nu)}{k(\nu)P_i(\nu)} = |\Gamma(\nu)|^2 \tag{3.4.10}$$

which is the desired quantity $|\Gamma(\nu)|^2$.

3.5 Experimental setup

3.5.1 The 48 GHz system

Apparatus

The 48 GHz cavity [140] is placed in a cryostat (figure 3.5) consisting in a steel vessel composed of three chambers.

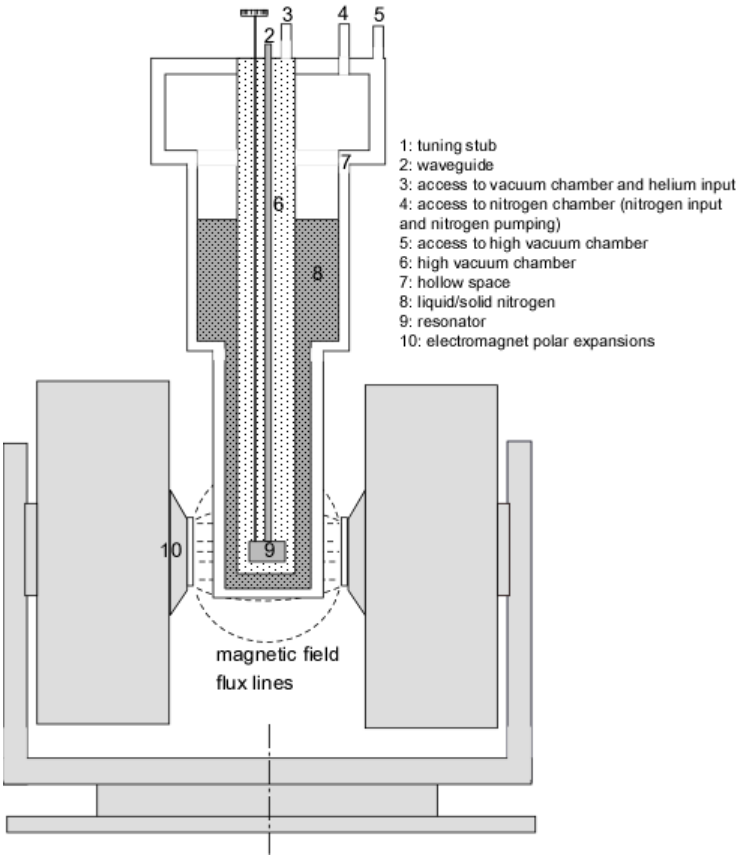

Figure 3.5: System at 48 GHz: cryostat and electromagnet.

In the outermost chamber a 10^{-6} mbar vacuum provides thermal insulation. The intermediate chamber contains liquid nitrogen, which can be frozen using a scroll pump that allows to reach temperatures below 60 K. The inner chamber, containing the resonator and the microwave line, is kept in a low pressure helium atmosphere (typically 0.2 mbar) to assure thermal exchange with the nitrogen bath. The cryostat is inserted inside the air gap of a conventional electromagnet. A static magnetic field up to $\mu_0 H \simeq 7750$ gauss can be generated.

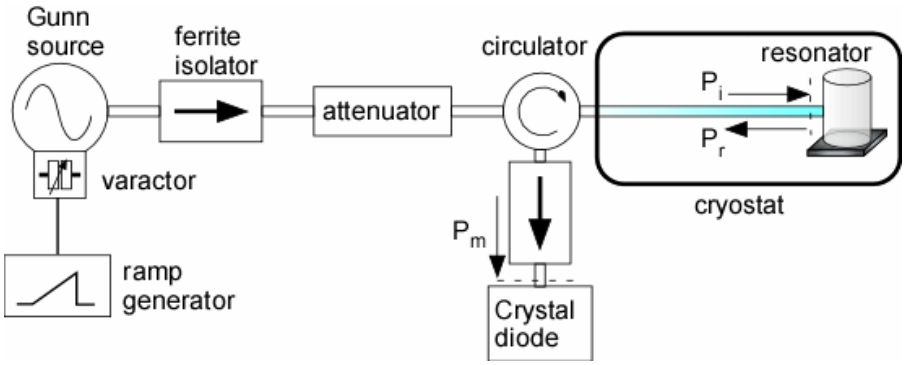

Figure 3.6: Diagram of the 48 GHz microwave circuit.

The microwave circuit is depicted in figure (3.6): a U-band waveguide connects the Gunn diode power source, the power detecting crystal diode and, by means of a vacuum pass-through, the waveguide that is located inside the cryostat together with the cavity. The last segment of the internal waveguide is specifically designed to minimize heat flow, by means of very thin metal walls reinforced by carbon fiber. The circulator directs the Gunn generated wave towards the resonator and deviates the wave reflected by the resonator towards the crystal detector. A ferrite isolator protects the Gunn diode from reflected waves. The Gunn diode operates in a voltage-controllable frequency range of 1 GHz centered in the 48.3 GHz frequency. It supplies a power of approximately 100 mW depending on the operating frequency and with a thermal coefficient of 0.04 dB/K. The operating frequency is also temperature-dependent, having a temperature coefficient of 5 MHz / K. The emitted power is calibrated according to a frequency-power table. The temperature drift is compensated by thermalizing the diode within ± 0.01 K, giving a residual frequency scattering of the order of $\pm$ 100 KHz.

The 48 GHz cavity

The cylindrical silver coated metallic cavity (figure (3.7)) operates in the TE_{011} mode at 48.2 GHz (see also appendix A.1). It has a diameter of 8.2 mm and an approximate height of 8 mm. One of the bases consists in a moving piston which allows to change the cavity length and therefore to tune its resonant frequency in a small range. On the other base the sample is held by a metallic plate pressed by a spring and housing a temperature sensor and an anti-inductive heater. Another heater is placed around the body of the cavity. Both bases are electrically isolated from the side walls by teflon layers: this allows to suppress the degenerate TM_{111} mode leaving unperturbed the TE_{011} mode. The sample surface is exposed to circular microwave currents with a radial dependency as reported in right panel of figure (3.7): it is clear that the edges of the sample are essentially not probed.

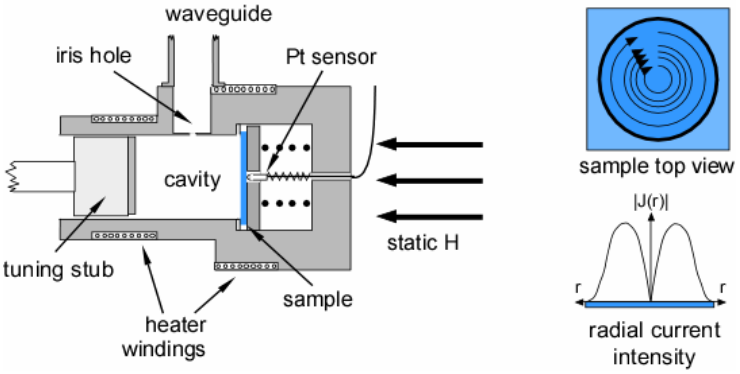

Figure 3.7: Cavity operating at 48 GHz. *Left panel*: section view. *Right panel*: current patterns on the sample.

The TE mode also assures that microwave electrical fields and currents are parallel to the sample surface. In the study of c-axis oriented HTCS films, only the (averaged) a, b plane properties are determined, without mixing with c-axis components.

The cavity is coupled to the waveguide through an iris, located on the cylinder side walls at half height where the cavity electric field has a maximum. The cavity axis is oriented horizontally, so that the sample is normal to the flux lines of the field generated by the magnet.

Calibration and measurement method issues

In a metal cavity the background contribution to the measure of Z_s of a superconductor (see equations (3.4.1) and (3.4.2)) contains only the conducting

walls terms. These terms can be determined by separately measuring the cavity with a silver disk in place of the sample (*homogeneous* configuration), so that:

$$R_m(T) = \frac{G_0}{Q_{U,hom}(T)} \tag{3.5.1}$$

$$\Delta X_m(T) = X_m(T) - X_m(\bar{T}) = -2G_0 \frac{\nu_{0,hom}(T) - \nu_{0,hom}(\bar{T})}{\nu_{0,hom}(\bar{T})} \tag{3.5.2}$$

Substituting the above expressions into (3.4.1) and (3.4.2) one obtains:

$$R_s(T,H) = \frac{G_s}{Q_U(T,H)} - \frac{G_s - G_0}{Q_{U,hom}(T)} \tag{3.5.3}$$

$$\Delta X_s(T,H) = X_s(T,H) - X_s(\bar{T},\bar{H}) = -2G_s \frac{\nu_0(T,H) - \nu_0(\bar{T},\bar{H})}{\nu_0(\bar{T},\bar{H})} + 2G_s \left(1 - \frac{G_0}{G_s}\right) \frac{\nu_{0,hom}(T) - \nu_{0,hom}(\bar{T})}{\nu_{0,hom}(\bar{T})} \tag{3.5.4}$$

Since thermal gradients affect repeatability, slow temperature variations are required. Moreover, the temperature variations of the microwave line response $k(\nu)$ impose to detune the cavity quite often. Since one cannot exactly reposition the piston, little jumps in the cavity resonant frequency (corresponding to an additional scattering on ΔX_s of the order of 100 mΩ) are produced every time the cavity is detuned and re-tuned.

I stress again that measuring magnetic field-induced variations $\Delta Z_s(H)$ these problems disappear or reduce. More precisely, background is exactly cancelled while line calibration can be performed only once, since the system is kept at fixed temperature.

Besides calibration contributions, another source of (systematic) error is given by the uncertainty in the computation of the geometric factor G_s, which enters as a scale factor in determining Z_s. Random errors sources, on the other hand, are quite diversified. In general, sensitivity depends strongly on frequency and on the quality factor of the resonator which is, in turn, influenced by the temperature (see for example references [109, 141, 142]).

A quantitative evaluation of the measurement sensitivity with metal cavity is now given.

The sample and the whole cavity geometric factors are $G_s = 11700\ \Omega$ (for a full base coverage) and $G_0 = 780\ \Omega$, respectively. The cavity unloaded quality factor in the homogeneous condition is about 9000, rising to 10000–12000 with an HTCS film in the superconducting state. Since in this case,

which corresponds to the maximum sensitivity achievable, the scattering on Q_U is at maximum ~ 250, by applying the standard error propagation to equation (3.5.3) one obtains that the sensitivity on R_s is $\approx$30 mΩ. A similar sensitivity evaluation can be performed for the sensitivity on surface reactance variations ΔX_s, which are obviously related to the frequency resolution of the system. This quantity depends in a complex manner on various factors: the resonant curve width (which is smaller for higher Q_L), the frequency stability of the microwave source, the accuracy of the Lorentzian fit, the scattering introduced by the detuning processes. In overall, considering the Gunn frequency stability and the scattering on ν_0 observable on typical measurements, ΔX_s scatters by 10–100 mΩ, depending on the low/high Q condition given and other factors such as thermalization.

Data acquisition

A comprehensive view of the data acquisition graph is given in figure 3.8. Data acquisition is performed by means of a National Instruments DAQ acquisition card and a IEEE 488 interface, computer controlled by Labview program. The saw tooth voltage ramp generator, which determines the frequency sweeps of 100 ms duration, produces a trigger at the beginning of each sweep. This triggers the beginning of the simultaneous acquisition of crystal detector voltage and ramp voltage readings, which are afterwards converted in power and frequency quantities, respectively. Each ramp, consisting in $\approx$ 600 acquired points, is then calibrated and real-time fitted to extract the Lorentzian curve parameters. These parameters are then recorded on a file together with the corresponding resonator temperature and field intensity readings, acquired through IEEE-488 interfaces.

3.5.2 The 24 GHz system

The microwave setup operating at 24 GHz [143] is substantially similar to the 48 GHz line. The resonator has the same characteristics: cylindrical metal cavity, operated in the TE_{011} mode, tunable, with a base holding the sample, iris-coupled through the lateral wall to a K-band waveguide. Cavity dimensions are a 16.4 mm diameter and a $\approx$ 25 mm height. Typical 10×10 mm^2 samples, smaller than the cavity base, are housed with the aid of a metallic mask. The uncertainty on the mask window determines a 20% uncertainty on G_s. The microwave circuit is topologically the same as in the 48 Ghz one. The cavity is mounted on the cold finger of a closed cycle cryogenerator. Temperatures down to 20 K can be reached. The cryogenerator induces strong mechanical vibrations, so that measurements are taken during thermal drift after the

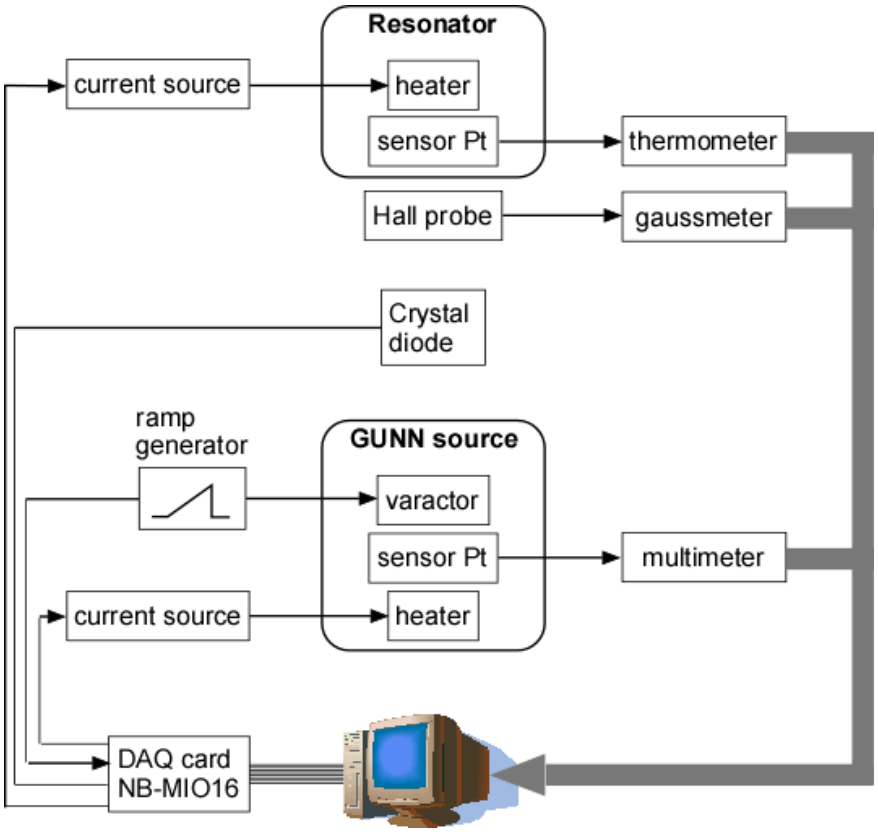

Figure 3.8: System at 48 GHz: data acquisition scheme. Thin lines: analogical signals. Thick lines: digital signals (IEEE-488 bus).

cryogenerator is switched off. The drift is sufficiently slow ($\approx$ 0.3 K/min in the range 30–200 K). Cavity mechanical relaxations affects repeatability of the resonant frequency in the low temperature range, below 50 K. No magnetic field can be applied with this setup, which is used for quick characterizations.

3.6 Design and realization of a dielectric resonator

In this section I will describe the design, realization and setup of the dielectric resonator, devised as an upgrade of the 48 GHz setup. A dielectric resonator was chosen to increase the system sensitivity and contextually reduce the resonator size. Dielectric resonators are often used for the characterization of HTCS films with focus on the determination of R_s [123]. As far as I know,

the use of dielectric resonators for the determination of both R_s and ΔX_s is not widespread (for example, among above mentioned references only [124] presents data for the reactance) and their use for measurement versus magnetic field H is even less common. In the following, therefore, I will describe the experimental technique with particular attention to the determination of $\Delta Z_s(H)$.

In general, the main expected advantages are:

- higher sensitivity, due to an increase of the quality factor Q_U (smaller absolute losses) as well as to a decrease of the sample geometrical factor G_s, so that the sample impedance affects the resonator parameters much more than in cavities;
- higher resonator stability and measure repeatability: the resonator volume is determined by the dielectric rod, so that mechanical relaxation is absent;
- smaller size: the linear size is reduced approximately by a factor $\sqrt{\varepsilon_{r1}}$, ε_{r1} being the real part of the relative permittivity of the dielectric material (i.e. $\varepsilon_r = \varepsilon_{r1} - \mathrm{i}\varepsilon_{r2}$);
- reduction of the resonator dimensions: it implies that smaller samples or smaller areas of large samples are probed, allowing for a scanning characterization of large areas.

Sapphire was chosen as dielectric by virtue of its very low dielectric losses, given by loss tangent $\tan\delta = \varepsilon_{r2}/\varepsilon_{r1} \approx 10^{-6}$ in the microwave frequency range at liquid nitrogen temperatures. Sapphire is slightly anisotropic (with $\varepsilon_{r1,ab} \simeq 9.27$ on the $a-b$ planes and $\varepsilon_{r1,c} = 11.345$ along the c-axis at $\approx$77 K [118]. It has small thermal coefficients both for thermal expansion and for the temperature dependence of the dielectric constant, which improves overall resonator stability.

The geometry is chosen in analogy with the metallic cavity: a cylindrical metallic enclosure containing a coaxial cylindrical dielectric rod of radius a and height h, having the c-axis along the cylinder axis (see left panel of figure (3.2).

The top and bottom plates are in contact with the sapphire rod (shielded Hakki-Coleman configuration). The sample under study replaces one of the plates (end-wall replacement technique). The TE_{011} resonant mode is selected because of the well known advantages of TE_0 modes: high Q_U, circular currents on the bases with no electric field component normal to the base, no need for electric contact between bases and lateral wall. Moreover, being one of the

lower frequency modes, it is usually well separated from other modes. The relations between Z_s of a superconducting base and the parameters of the dielectric resonator are given in the next section.

3.6.1 Measurement of Z_s through a dielectric resonator

The unloaded quality factor Q_U of a shielded dielectric resonator is determined by ohmic power losses on the (super)conducting walls and by dielectric losses. A treatment of the electromagnetic problem in dielectric resonators is given in appendix A.

The full expression for the sample surface resistance R_s can be derived from (A.2.11) giving a specialized version of (3.4.1):

$$R_s = \frac{G_{base}}{Q_U} - G_{base}\left(\frac{R_{bm}}{G_{base}} + \frac{R_{lm}}{G_{lat}} + \eta \tan\delta\right) \tag{3.6.1}$$

where:

- G_{base} and G_{lat} are the geometric factors of the base and of the lateral shield, respectively;
- R_{bm} and R_{lm} are the surface resistances of the base and lateral conductors, respectively, in principle different;
- $\tan\delta$ and η are the dielectric loss tangent and electric energy filling factor;
- the usual temperature and field dependencies are not reported for clarity.

An important figure qualifying the accuracy of the resonator is the filling factor F_r, defined as the ratio between the sample power losses and the total losses. When all the walls and bases are made from the same metal ("homogeneous resonator"), $R_s = R_{bm} = R_{lm} = R_m$, and:

$$F_{r0} = \frac{R_m/G_{base}}{2R_m/G_{base} + R_m/G_{lat} + \eta \tan\delta} \tag{3.6.2}$$

In the ideal situation in which both the dielectric losses and the lateral wall ohmic losses could be neglected, F_{r0} would have the maximum value $F_{r0}^{max} = 1/2$.

Surface reactance variations can be derived from equation (A.2.12) giving the specialized version of (3.4.2):

$$\Delta X_s = -2G_{base}\frac{\Delta\nu_0}{\nu_0} - G_{base}\left[\frac{\Delta X_{bm}}{G_{base}} + \frac{\Delta X_{lm}}{G_{lat}} + \left(\eta\frac{\Delta\varepsilon_{r1,a-b}}{\varepsilon_{r1,a-b}} + 2\sum_k |p_{d_k}|\frac{\Delta d_k}{d_k}\right)\right] \tag{3.6.3}$$

The resolution, sensitivity and accuracy of the dielectric resonator are given by:

- Q_U, the higher the better: it affects the resolution of R_s (through Q_U^{-1}) and of ΔX_s (since $\Delta X_s \propto \Delta\nu_0/\nu_0 \propto \Delta\nu_{FWHM}/\nu_0 \propto Q_U^{-1}$);
- the sample geometric factor G_s, which has a primary role in the determination of the sensitivity of the resonant system to variations of Z_s; this is particularly clear considering, from (3.6.1) and (3.6.3), $\Delta Z_s(H) = G_s[\Delta(1/Q_U) - 2\mathrm{i}\Delta\nu_0/\nu_0]$;
- the filling factor F_r which is a measure of the weight of the background.

Since F_r and Q_U depend on Z_s, which varies by orders of magnitude through the superconducting transition, to evaluate the resonator performances I will refer to the homogeneous configuration, considering it as an average situation.

3.6.2 Size design

The design of the resonator (the choice of the rod radius a and height h and of the metallic shield radius b) is a delicate balance between performance and experimental constraints (an example of general design guidelines can be found in [144]). In the present case, the main requirements are:

1. a resonant frequency around 48 GHz at $\sim$ 77 K similarly to the 48 GHz metal cavity;
2. the reduction of the sample area probed by the resonator (roughly defined by $2a$ in linear dimensions) for future developments (measurements of single crystals of linear dimensions $\sim$1–2 mm, scanning of large films);
3. the outer diameter $2b$ should be sufficiently larger than $2a$ in order to reduce the lateral wall losses (which go to zero as b increases), but simultaneously not too big in order to limit the overall size;
4. the need for detuning and coupling mechanisms require $2b$ and h sufficiently large.

From point 2 I have $2a \simeq 2$ mm. In order to satisfy points 3 and 4 and to avoid the use of metal masks for 10×10 mm^2 films, I fix $2b$=9 mm and require $h \simeq$2.5 mm. a and h are not independent, since point 1 is needed. Using $\varepsilon_{r1,a-b} = 9.27$ at 77 K, I search for an optimization of Q_U, F_{r0} and G_s by varying the single degree of freedom given by the aspect ratio $2a/h$.

Figure 3.9 reports homogeneous Q_U as a function of the ratio $2a/h$ (left panel), computed through the above values and with $R_s = R_{bm} = R_{lm} = 0.02\ \Omega$ (corresponding to the order of magnitude of the surface resistance values of the metallic cavity), and with height h and a (right panel) determined in order to assure the required ν_0. In the left panel of this figure two homogeneous filling factors are also reported: F_{r0} from (3.6.2), related to the whole base surface, and $F_{r0,reduced} = \frac{G_s}{G_{reduced}} F_{r0}$, related to a reduced surface $S_r = \pi$ mm^2 (for small samples of linear size $\sim$2 mm).

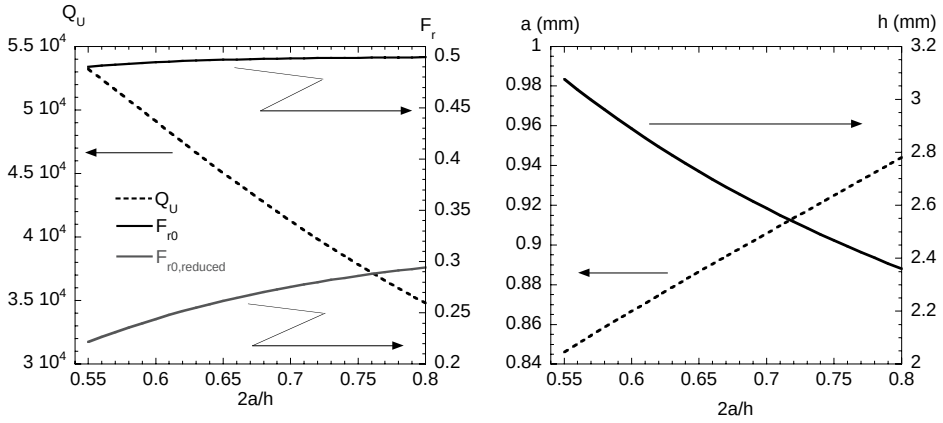

Figure 3.9: Design of the dielectric resonator with shield radius b=4.5 mm. *Left panel*: Q_U and F_{r0} vs the aspect ratio $2a/h$. *Right panel*: a and h vs the aspect ratio $2a/h$.

$2a/h$ is limited below by the mode cutoff condition and above by the requirements on h and a (see right panel of figure 3.9). Two main features can be seen: absolute best values of Q_U are obtained for smaller values of the ratio $2a/h$, while both F_{r0} and $F_{r0,reduced}$ increases with $2a/h$, being F_{r0} always within 2% of its optimum 0.5 value and $F_{r0,reduced} \approx 0.5 F_{r0}$ varying within 20%.

I therefore choose $2a/h = 0.6$ to allow for a safety margin from the cutoff condition in order to compensate potential geometrical and physical tolerances. As a consequence, one has h=2.889 mm, a=0.8667 mm, $F_{r0} \simeq 0.5$ and $F_{r0,reduced} \simeq 0.24$.

As a last step, I calculate the frequency position of the nearest modes in order to verify if they are sufficiently far away (general mode chart can be found in [145]). By explicitly taking into account the uniaxial anisotropy of the sapphire at 77 K ($\varepsilon_{r1,a-b} = 9.27$, $\varepsilon_{r1,c} = 11.345$ [118]), one obtains $\nu_0(HEM_{111})$=37.467 GHz, $\nu_0(TM_{011})$=49.220 GHz, $\nu_0(HEM_{112})$=49.010 GHz. It should be mentioned that, neglecting c-axis anisotropy, one would have obtained $\nu_0(HEM_{111})$=39.308 GHz, $\nu_0(TM_{011})$=50.523 GHz, $\nu_0(HEM_{112})$=49.824 GHz. The minimum acceptable distance can be derived from the half-full-height-width of the Lorentzian bell of the main mode, by definition equal to

$\Delta\nu_{HFHW} = \nu_0/Q_L \simeq \nu_0/Q_U$ for small coupling. In the worst case of $Q_U \simeq 500$ (superconducting film in the normal state) one has $\Delta\nu_{HFHW} \simeq$100 MHz, which is far smaller than the obtained spurious modes spacing.

Sapphire rods having nominal radius $a = 0.88 \pm 0.02$ mm and height $h = 2.90 \pm 0.02$ mm were bought. They are optically polished on the flat surfaces. Among them, a sapphire having measured dimensions a=0.874 mm and h=2.918 mm resulted in the better homogeneous Q_U and therefore was used throughout to build up the dielectric resonator. The theoretical computation gives, for this resonator, the following figures at 77 K for the TE_{011}: ν_0=47.580 GHz, $\eta = 0.86$, $G_{base} = 1995\ \Omega$, $G_{lat} = 8.44 \times 10^4\ \Omega$, overall $G_0 = (2G_{base}^{-1} + G_{lat}^{-1}) = 985\ \Omega$. The calculated spurious modes have frequencies $\nu_0(HEM_{111})$=37.137 GHz, $\nu_0(TM_{011})$=48.749 GHz, $\nu_0(HEM_{112})$=48.561 GHz.

3.6.3 Resonator structure

A scheme of the whole dielectric resonator is given in figure 3.10. The sample, backed by a 4 mm thick metal disk incorporating a Pt-100 temperature sensor, is pressed by a spring (through an outer pressing cage) on the top of the metallic supporting case.

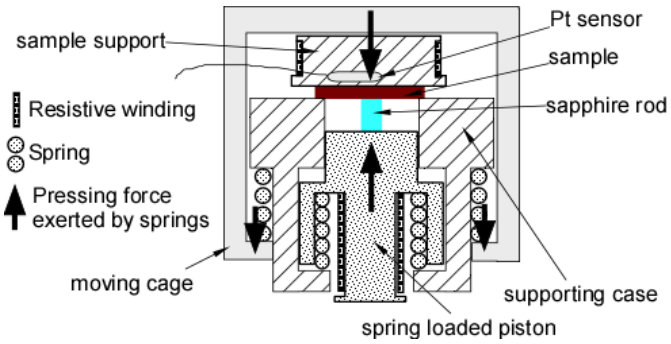

Figure 3.10: Dielectric resonator structure.

The sapphire rod is pressed against the sample by means of a spring loaded piston. Two resistive anti-inductive windings, located on the metal disk and on the piston, act as heaters. All the metallic parts were worked out in non-magnetic brass. The base surface of the piston and a thin metal disk used for the calibration of the resonator are polished. Since the resonator presents a noticeable sensitivity to the centering of the sapphire rod inside the metallic shield, an appropriate centering tool is used.

The coupling between the resonator and the external microwave line is obtained through a probe (electric field coupling), made by a thin (0.2 mm) metallic wire which penetrates in the metallic enclosure for a length of $\simeq$ 1.5 mm (fig. 3.11).

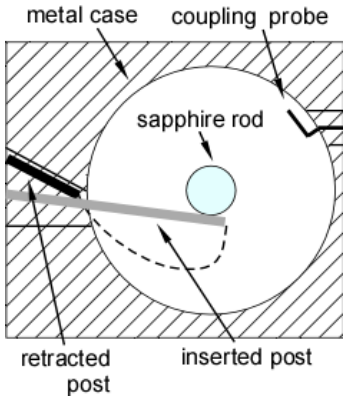

Figure 3.11: Sectional view of the dielectric resonator, showing the coupling probe and the decoupling post.

The microwave fields of the probe couple with the azimuthal electrical field E_ϕ inside the resonator: therefore, in order to have maximum coupling effect, the probe is located in the half height plane, where E_ϕ has its maximum z-dependent value. In this configuration the homogeneous resonator has a coupling coefficient β=0.1 at room temperature. The probe is inserted inside the central conductor of a coaxial V launcher (Wiltron V103F), which is connected to the U-band waveguide by means of an inline U-band–V-coaxial transition (Quinstar Technology). Unlike most of commercially available transitions, this component has parallel waveguide and coaxial connections axes, so that the microwave line does not bend inside the cryostat, thus giving a more compact structure.

For the line calibration (section 3.4) a particular detuning mechanism has been developed. A metallic post, 0.5 mm diameter, is inserted and retracted through a small hole in the lateral wall (figure 3.11). The insertion and extraction are operated from outside the cryostat. The movement of the post is such that, when fully inserted, it is located on the median plane and almost tangent to the dielectric rod. In this way it couples to and heavily perturbs the resonating mode, suppressing it totally. Compared with the moving-piston detuning of the metallic cavity, this system allows for an intrinsically superior repeatability of the line calibration process, which cancels any scattering from the frequency measurements.

A photograph of the whole device is reported in figure (3.12).

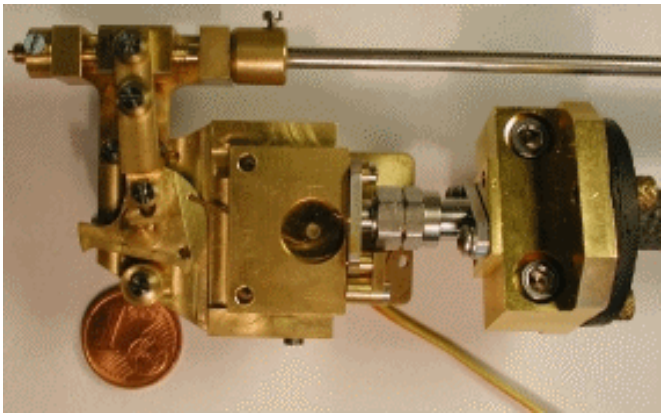

Figure 3.12: Photograph of the dielectric resonator.

3.6.4 Upgrade of the 48 GHz line

Contextually to the development of the sapphire resonator, the 48 GHz line was upgraded by substituting the Gunn diode with a synthesized source (HP 83751B equipped with a multiplying head 83556A) operating in the frequency range 40–60 GHz with an output power up to 3 dBm and frequency stability $\sim$ KHz. The measuring procedure was slightly modified as sketched in figure 3.13. Each frequency sweep, set with a 0.1 s duration, is now initiated with a software primary trigger sent to the synthesized source. The source then generates the frequency sweep and simultaneously emits 1601 secondary triggers evenly spaced in frequency: each one of them triggers the DAQ to take a reading of the power detected by the crystal diode. The corresponding frequency values are calculated by dividing the frequency interval by 1601. The latencies in the synchronization determine uncertainties on the frequency points less than 350 Hz, which can be safely neglected. Magnetic field and temperature reading and controlling are as described in section 3.5.1.

3.6.5 Resonator performances

I first consider the dielectric resonator in its homogeneous configuration (both base plates in metal). At room temperature its typical response is reported in figure 3.14, giving the following figures of merit: Q_U=5950, ν_0=47.38 GHz

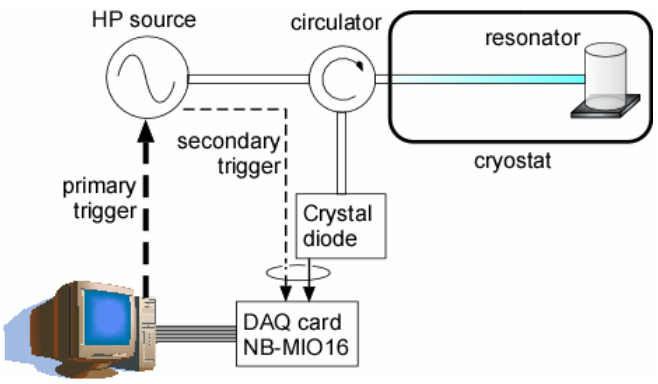

Figure 3.13: New acquisition scheme based on the synthesized source.

(in good agreement with the theoretical value of 47.30 GHz computed with $\varepsilon_{r1,a-b} = 9.4$) and β=0.13.

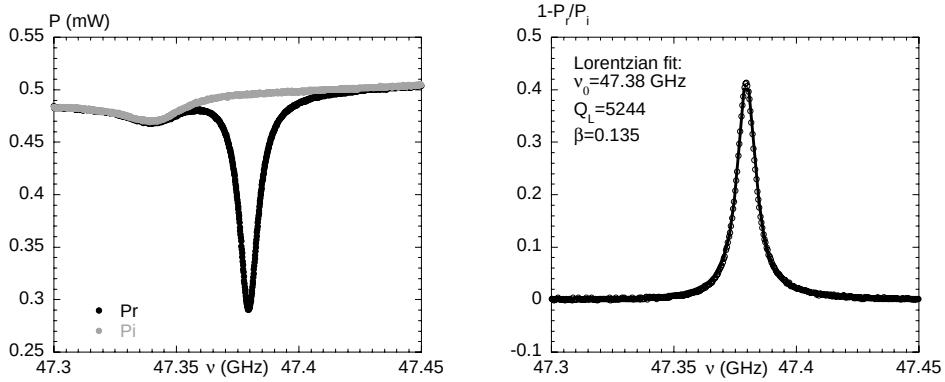

Figure 3.14: Resonance curve of the dielectric resonator at room temperature. *Left panel*: recorded P_r and P_i. *Right panel*: measured lorentzian curve (open symbols) and fit (full line).

Figure 3.15 reports a wider frequency sweep where the nearest spurious modes appear. Their difference from the theoretical values $\nu_0(HEM_{112})$=48.18 GHz and $\nu_0(TM_{011})$=48.58 GHz (computed with $\varepsilon_{r1,a-b} = 9.4$, $\varepsilon_{r1,c} = 11.59$) is ∼600 MHz.

The resonator response against an applied magnetic field is measured at room temperature and reported in figure 3.16, performing the same field sweeps as in the measurements on HTCS. It can be seen that Q_U shows a small scattering uncorrelated to the field, while ν_0 shows a very a small H-dependence

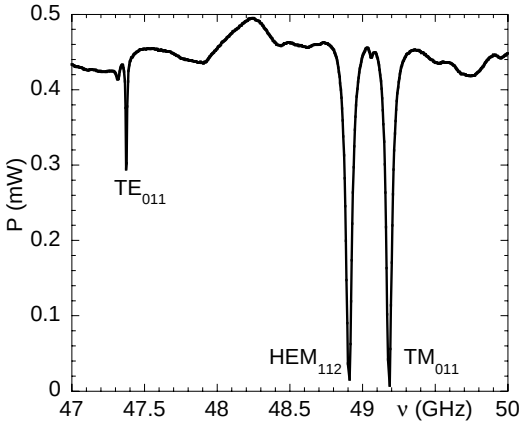

Figure 3.15: Frequency sweep between 47 GHz and 50 GHz. In addition to the main TE_{011} mode, modes HEM_{112} and TM_{011} are present.

at higher fields only. In overall, both factors determine an error of ~ 1 mΩ on the whole $\Delta Z_s(H)$ evaluated between $H = 0$ and $H_{max} \simeq 0.8$ T.

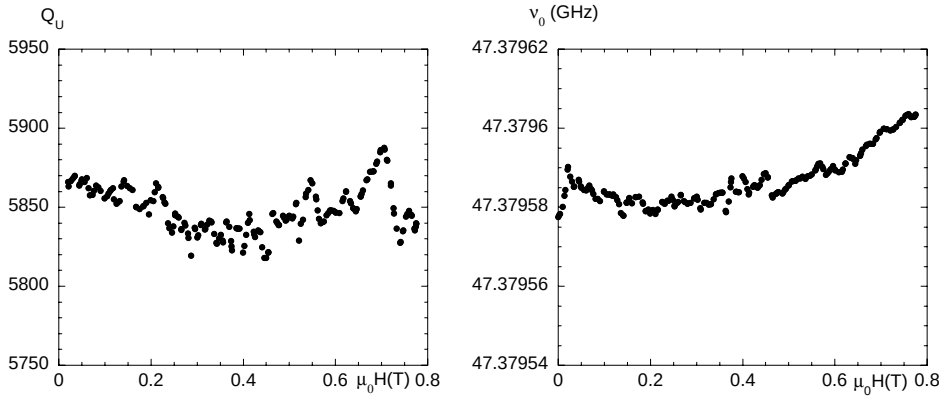

Figure 3.16: Field dependence of parameters of the homogeneous dielectric resonator at room temperature. *Left panel*: Q_U; *right panel*: ν_0.

The temperature behaviour of the measured Q_U and ν_0 are reported in figure (3.17). At 80 K Q_U ~10000. The resonant frequency (right panel) shows regular decrease with temperature and no jumps in correspondence to the line calibration points (an enlargement around 97 K is shown in the inset of right panel).

In order to evaluate the improvement in the measurement accuracy of HTCS surface impedance $R_s + \mathrm{i}\Delta X_s$, a typical measurement performed on a superconducting sample is now considered. The procedure followed to extract Z_s by calibrating the dielectric resonator background is hereby described.

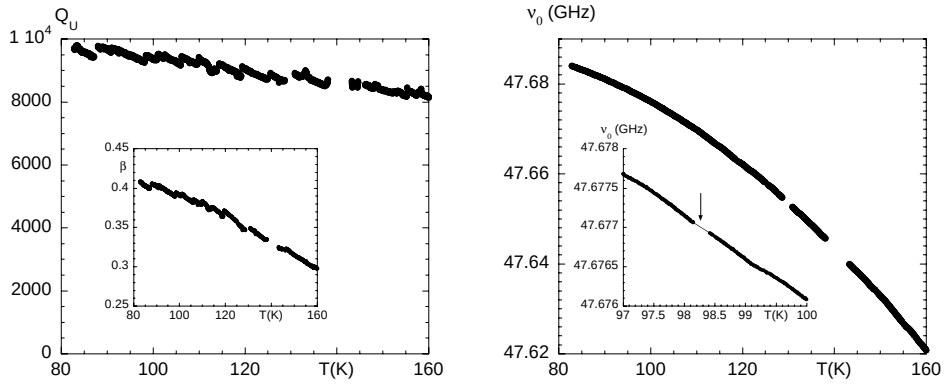

Figure 3.17: Temperature dependence of parameters of the homogeneous dielectric resonator. *left panel*: Q_U (β in the inset); *right panel*: ν_0. Inset of right panel: zoom on ν_0 in correspondence to a detuning-tuning process. The thin line is given as a guide for the eye.

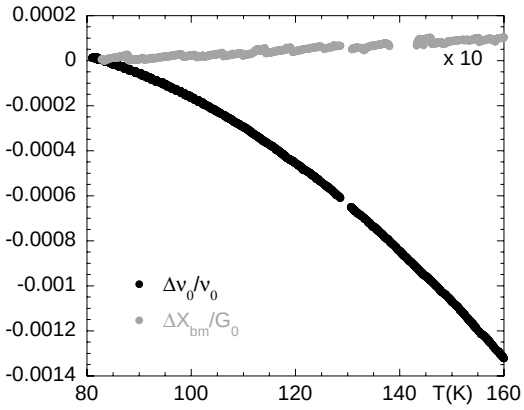

Figure 3.18: Homogeneous dielectric resonator: comparison between the measured frequency change $\Delta\nu_0/\nu_0$ and the metallic shift $\Delta X_{bm}/G_{base}$. The latter is multiplied by 10 for ease of comparison.

In equation (3.6.1) background contributions include the metallic plate losses, the lateral wall losses and the dielectric losses: only the first one is dominant, since sapphire losses (0.1–1 mΩ, with loss tangent from [118]) are well below metallic ohmic dissipation values and since lateral wall geometric factor G_{lat} is much larger than G_{base}. Therefore R_s is given simply by:

$$R_s \cong \frac{G_{base}}{Q_U} - R_{bm} \cong \frac{G_{base}}{Q_U} - \frac{1}{2}\frac{G_{base}}{Q_{U,hom}} \tag{3.6.4}$$

In the last equality one has used $R_{bm} \cong G_{base}/(2Q_{U,hom})$, which can be derived from the homogeneous resonator measurement within the same approximations used above.

In the calibration of X_s one can again safely neglect the lateral wall contribution. On the other hand, the dielectric induced frequency shift, mainly due to permittivity thermal variations[3], is no longer negligible.

This can be shown by examining the homogeneous resonator measurement: assuming the validity of the Hagen-Rubens condition for the metal (R_{bm}=X_{bm}), the metal reactance contribution to the temperature-induced $\Delta\nu_0/\nu_0$ can be evaluated as

$$\frac{\Delta X_{bm}}{G_{base}} = \frac{\Delta R_{bm}}{G_{base}} = \Delta\frac{1}{2Q_{U,hom}} \tag{3.6.5}$$

In figure 3.18 the measured $\Delta\nu_0/\nu_0$ between 80 K and 160 K is compared to the so-estimated metal contribution $\Delta X_{bm}/G_{base}$. Over a temperature range of 10 K, $\Delta X_{bm}/G_{base} \lesssim 10^{-6}$ while $\Delta\nu_0/\nu_0 \simeq 10^{-4}$. However, even if metal reactance is a small contribution to the frequency shift, it cannot be neglected. In fact, $\Delta X_{bm} \cong 0.26\ \mu\Omega$ for every K which is comparable with the resonator sensitivity on ΔX_s, of the order of 1 mΩ (see the following). One therefore uses the measured frequency shift in the homogeneous situation:

$$\frac{\Delta\nu_{0,hom}}{\nu_{0,hom}} = -\frac{\Delta X_{bm}}{G_{base}} - \left.\frac{\Delta\nu_0}{\nu_0}\right|_{diel} \tag{3.6.6}$$

together with the estimation (3.6.5) for X_{bm} in order to obtain the calibrated ΔX_s from (3.6.3) as follows:

$$\Delta X_s = -2G_{base}\frac{\Delta\nu_0}{\nu_0} + 2G_{base}\frac{\Delta\nu_{0,hom}}{\nu_{0,hom}} + G_{base}\frac{1}{2}\Delta\frac{1}{Q_{U,hom}} \tag{3.6.7}$$

It is worth recalling again that magnetic field-dependent measurements at fixed temperature are immune from calibration errors, being subject only to the residual scattering on Q_U (~ 1 mΩ on ΔR_s) and to the slight shift observed on ν_0 at higher fields only (~ 1 mΩ on ΔX_s over the full field sweep).

The dielectric resonator and the metallic cavity are now compared. One first important point concerns the sample geometrical factors G_s, being 1995 Ω and 11700 Ω respectively: this means that, for equal Q_U, the dielectric resonator has a sensitivity increased by one order of magnitude with respect to the cavity. A sample measurement of Z_s in a TBCCO thin film (sample

[3]In fact, for the TE_{011} mode here considered, in expression (3.6.3) $\eta \cong 1$, the dimensional filling factors p_{d_k} are ~ 0 and ~ 1 for the rod dimensions radius and height, respectively. Lateral wall contributions are neglected. Since permittivity thermal coefficient $\Delta\varepsilon_{r1,a-b}/\varepsilon_{r1,a-b}$ is one order of magnitude greater than the thermal expansion coefficients $\Delta d_k/d_k$ [146], the frequency drift in sapphire is indeed dominated by permittivity changes.

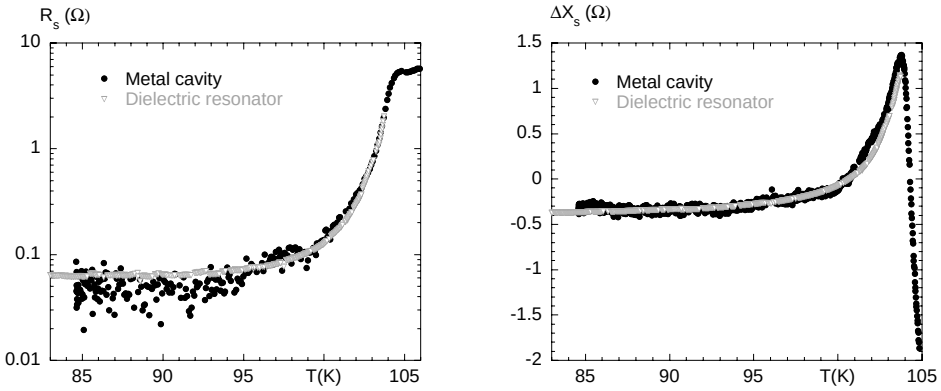

Figure 3.19: Surface impedance of TBCCO sample TS2 measured with the metal cavity at 48.2 GHz (full dots) and with the dielectric resonator at 47.6 GHz (open triangles). Real part of Z_s on the *left panel* and imaginary part (T_{ref}=100 K) on the *right panel*. The agreement is excellent. The improvement in sensitivity in the measurements through the dielectric resonator is apparent.

TS2, thickness 2400 Å, $T_c \approx 104K$) in the superconducting state is performed through the metal cavity (at 48.2 GHz) and through the dielectric resonator (at 47.6 GHz) and presented in figures 3.19 and 3.20. Data of the dielectric resonator is not available above $\approx$ 103 K because the surface resistance of the HTCS becomes too high and the resonance signal is lost.

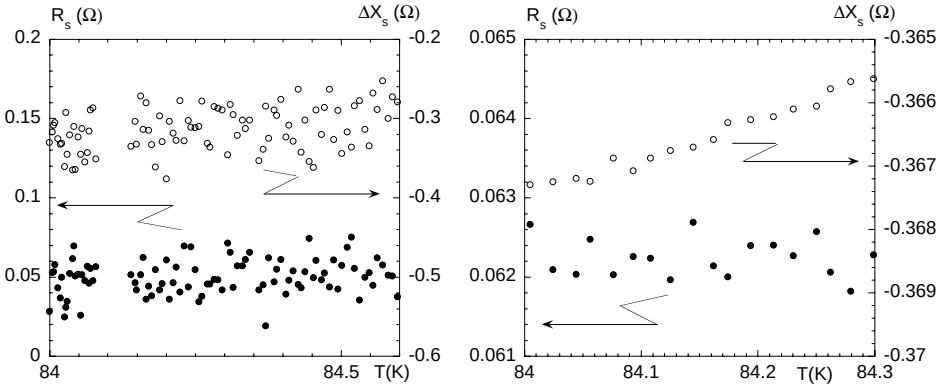

Figure 3.20: Close up of the surface impedance of TBCCO sample TS2 measured through the metal cavity at 48.2 GHz (*left panel*) and through the dielectric resonator at 47.6 GHz (*right panel*). Real parts: full dots. Imaginary parts (T_{ref}=100 K): open symbols. The reduction in scattering using the dielectric resonator is evident (note the different scales).

In the metal cavity data R_s goes down to 0.05 Ω, having a scattering of $\simeq$ 40 mΩ, while ΔX_s has a scattering of $\simeq$ 80 mΩ. Using the dielectric resonator, on the other hand, R_s and ΔX_s scattering are $\simeq$ 0.5 mΩ and $<$ 0.5 mΩ, respectively. The accuracy, therefore, is increased by two orders of magnitude.

In conclusion, the sensitivity of the measurements has been increased by two orders of magnitude by updating the microwave line and using the dielectric resonator.

3.6.6 Future developments

On the basis of the present work, further improvements are planned:

- the present resonator fits into a smaller cryostat that will allow to reach highest magnetic fields;
- the open-ended configuration will be studied. The gap between the sapphire rod and the metal plate will allow to reduce ohmic losses, while the gap between the sample and the rod could allow to thermally decouple the sample from the resonator;
- annular metallic masks will be tested to accommodate smaller samples. If the resonant mode will not be significantly perturbed, the outer diameter could be increased, thus reducing background losses and the resonator sensitivity to rod centering.

Chapter 4

The superconducting films: the electromagnetic problem

This chapter is devoted to the study of the effective surface impedance in thin films. In thin films the electromagnetic microwave field can reach the underlying substrate. The interaction with the whole layered structure can be modelled by an effective surface impedance which is in general different from the expression valid for bulk samples. In particular, this quantity can show temperature and frequency behaviours highly affected by the substrate. The identification of these contributions is essential for a correct interpretation of the data. On the basis of standard impedance transformation, I illustrate the effect of various substrates on the effective surface impedance. Experimental results for the effective surface impedance of HTCS on dielectric and semiconducting substrates are shown.

4.1 Introduction

In the previous chapter the surface impedance Z_s was introduced as the main quantity measured by microwave experiments. It was also anticipated that the simple expression given in equation (3.1.1) holds only in the case of bulk samples, i.e. when the sample thickness t_s is much greater that the penetration depth of the impinging electromagnetic (em) field, which is of the order of $\min(\lambda, \delta)$. In fact, when $t_s \leq \min(\lambda, \delta)$, which is typically true in epitaxial HTCS films, the em field propagates through the sample and reaches the underlying layers. In a typical setup these layers include the film substrate and a backing metallic plate. The resulting layered structure, depicted in figure 4.1, can also include very thin buffer layer(s) between the film and the substrate which, as suggested by the results reported in [147], will be neglected in the

remainder of the treatment.

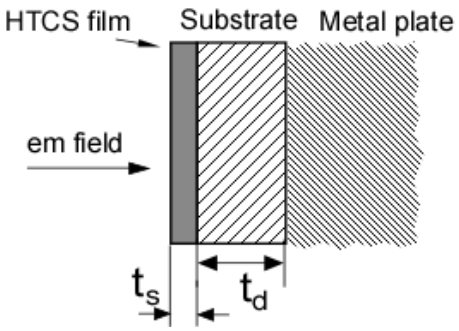

Figure 4.1: Layered structure resulting in a typical microwave measurement on HTCS films (buffer layers are not considered).

For the case depicted in figure 4.1, the impedance transformation [97] gives an *effective* surface impedance Z'_s (from now on the prime sign is used to designate effective quantities):

$$Z'_s = Z_s^w \frac{Z'_d + \mathrm{i} Z_s^w \tan(k_s^w t_s)}{Z_s^w + \mathrm{i} Z'_d \tan(k_s^w t_s)} \tag{4.1.1}$$

where Z'_d is the effective surface impedance of the substrate, Z_s^w and k_s^w are the wave impedance and the wave propagation constant in the HTCS film. The latter two quantities exactly coincide with the plane wave Z_s and $k_s = \mu_0\omega/Z_s$ for TEM wave propagation, while for guided propagation (including resonators) in general they are given by the corresponding modal quantities. Let $\mathbf{k} = (k_{//}, k_{//}, k_\perp)$. The TEM approximation is justified when $k_{//} \ll k_\perp$. This is often satisfied (including the case of TE operated resonators) and only in very particular arrangements the modal quantities differ significantly from TEM. From now on this approximation will be assumed and the "w" superscript will be dropped.

Several simplified forms of equation (4.1.1) can be written in different limiting conditions. As an approximate criterion, if $|Z'_d| \gg |Z_s|$, the substrate contribution can be neglected [148, 149] and equation (4.1.1) reduces to the intrinsic surface impedance of the film [150, 151]:

$$Z'_s \simeq Z_s^{(\mathrm{i})} = -\mathrm{i} Z_s \cot(k_s t_s) \tag{4.1.2}$$

which, if $t_s \ll min(\lambda, \delta)$, gives the so-called thin-film approximation:

$$Z'_s \simeq Z_f = R_f + \mathrm{i} X_f = \frac{1}{\tilde{\sigma}_s t_s} \tag{4.1.3}$$

Depending on the film thickness and temperature range, the last two expressions have been widely used. On the other hand, if $|Z'_d|$ is not large enough, substrate effects cannot be neglected and the full (4.1.1) must be used. In this case an evaluation of Z'_d is necessary: in general it can be modelled in the same way as the film, allowing to write the following expression:

$$Z'_d = Z_d \frac{Z_m + \mathrm{i} Z_d \tan(k_d t_d)}{Z_d + \mathrm{i} Z_m \tan(k_d t_d)} \tag{4.1.4}$$

where Z_d, k_d and t_d are respectively the characteristic impedance, the propagation constant and the thickness of the substrate and Z_m is the bulk impedance of the underlying metallic plate. The computation of Z'_d requires the knowledge of Z_d, which depends on the nature of the substrate material: broadly speaking, dielectric or semiconductor or metal. In general, dielectrics present high enough impedances so that the thin-film approximation for Z'_s holds, although exceptions can arise when the dielectric permittivity has large thermal variations (as in $SrTiO_3$), showing marked resonance phenomena at given temperatures [106, 148, 151], or when the film and the substrate characteristic impedances combine together giving frequency-dependent peaks in R'_s [152]. On the other hand, metallic substrates have small surface impedance values so that their contribution to the HTCS effective Z'_s [153] cannot be neglected. Lastly, an intermediate case with rich and complex phenomenology [149] is represented by semiconductors, investigated as potential substrates in the perspective of integrating semiconductor-based electronics with superconductors for the building of new hybrid devices and circuits [154].

The study and the correct identification of potential substrate effects in measurements of the HTCS effective surface impedance are essential both from a technological point of view, since they contribute to the performances of real devices, and from a point of view of fundamental physics. In particular it is important to distinguish true surface impedance anomalies, which can point to relevant HTCS exotic properties [138], from substrate effects, which can give rise to measurement artifacts susceptible of misinterpretations.

The following sections are devoted to the analysis of HTCS samples grown on various substrate materials. Each set of measurement shows peculiar characteristics which are naturally explained in the light of the above mentioned effective surface impedance approach.

4.2 Dielectric substrates: experimental results

Dielectric substrates, of typical thicknesses t_d=0.5–1 mm, are widely used for the growth of epitaxial films. In addition with physical and chemical compat-

ibility requirements, microwave applications demand also substrates having loss tangent as low as possible. As a consequence, substrates are substantially transparent to the em field propagating through the thin superconducting film. Therefore the em field reaches the metallic back-plate generally used as a support or enclosure for the HTCS sample or device. In this case a semi-quantitative evaluation of the effective surface impedance measured in experiments can be obtained by taking $Z_m \simeq 0$, so that in equation (4.1.4) Z'_d reduces to:

$$Z'_d \simeq \mathrm{i}X'_d = \mathrm{i}Z_d \tan(k_d t_d) \tag{4.2.1}$$

where $Z_d = Z_0\sqrt{\varepsilon_r}$, ε_r is the permittivity of the dielectric (assumed isotropic), $k_d = Z_d/(\omega\mu_0)$ and $Z_0 = 377\ \Omega$ is the vacuum impedance. In the microwave range and for typical values of the above introduced quantities, Z_d and therefore Z'_d reach the order of $10^2\ \Omega$, thus well above typical values for Z_s in superconductors. Consequently thin film expressions such as (4.1.2) or (4.1.3) can be and actually are used. This scenario holds if in the temperature and frequency range used one is far away from the resonance or antiresonance conditions, respectively represented by the divergence or vanishing of $\tan(k_d t_d)$. As an example of this case, I report and discuss a measurement of the effective surface impedance of a calcium-substituted YBCO film[1] ($Y_{1-y}(Ca)_yBa_2Ca_3O_{7-\delta}$ with y=0.07, t_s = 2200 Å, T_c=81 K) grown on $SrTiO_3$ with t_d = 0.5 mm[3] performed with the 48 GHz cavity.

In figure 4.2 the measured Z'_s as a function of the temperature is presented. The real part R'_s exhibits a clear oscillating behaviour, having an amplitude decreasing while temperature lowers. The oscillations become very small as the film becomes superconducting (similar measurements are also reported in literature [106, 148]).

$\Delta X'_s$ shows a similar oscillatory behavior (not reported in literature, as far as I know). The oscillations follow the behavior of R'_s, but they are not "in phase" with it: $\Delta X'_s$ maxima correspond to half height of the oscillations of R'_s.

This behavior, reminiscent of resonance phenomena, is determined by temperature variations of ε_r. In fact, it is well known that ε_r in $SrTiO_3$ [106, 148, 151] attains large values and changes strongly with temperature, approximately according to the Curie law $\varepsilon_r = \frac{\varepsilon_{r0}}{T-T_0}$. As a consequence, Z'_d of the $SrTiO_3$ substrate backed by a conductor significantly varies with temperature.

[1] Courtesy of G. Celentano, *Superconductivity Division, ENEA - Frascati Research Center*, Roma, Italy.

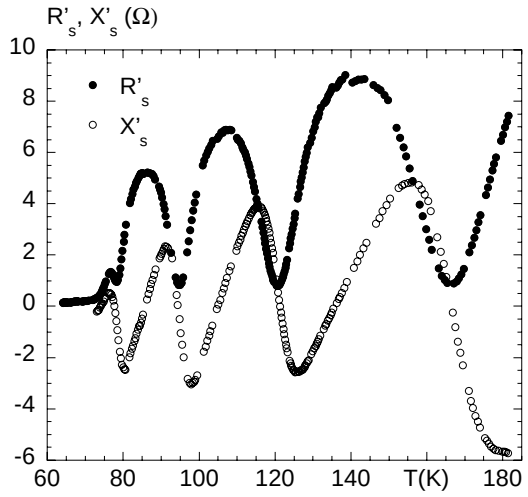

Figure 4.2: Z'_s of $Y_{1-y}(Ca)_yBa_2Ca_3O_{7-\delta}/SrTiO_3$ sample measured at 48 GHz.

The effective surface impedance Z'_s above T_c can be rewritten as follows:

$$Z'_s = \frac{R_f X'^2_d}{R^2_f + X'^2_d} + \mathrm{i}\frac{R^2_f X'_d}{R^2_f + X'^2_d} \tag{4.2.2}$$

being $R_f = \rho_n/t_s$ the thin film expression for the superconductor surface resistance and having assumed lossless dielectric ($Z'_d = \mathrm{i}X'_d$ from equation (4.2.1)). One notes that at antiresonance $\tan(k_d t_d) \to \infty$ so that Z'_d diverges and R'_s equals R_f. The latter can be therefore obtained as the upper envelope of R'_s, as shown in the left panel of figure 4.3. From (4.2.2) one has that, in correspondence to R'_s extrema, X'_s is zero. One then has the reference values to convert measured $\Delta X'_s$ to absolute X'_s (reported in the right panel of figure 4.3). Moreover, it can be easily shown that X'_s extrema (zeroes of $\frac{\delta X'_s}{\delta X'_d}$) are enveloped between the two $\pm\frac{1}{2}R_f$ curves. This is experimentally confirmed in right panel of figure 4.3, where the straight lines enveloping X'_s are derived from the envelope of the real part R'_s.

In order to complete this analysis one can calculate the values for the relative permittivity of $SrTiO_3$ at the resonance and antiresonance temperatures (maxima and minima of R'_s, coincident with the whole set of zeroes of X'_s). The so-obtained data are compared with data existing in literature [155] and fitted to the Curie law (see figure 4.4).

In conclusion, the effect of a dielectric substrate Z'_s appears to be well understood. Unless resonance phenomena arise, Z'_s can be approximated by (4.1.2).

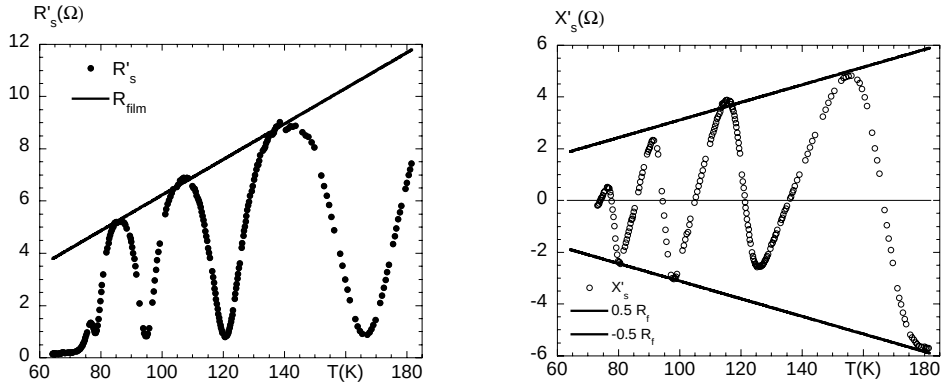

Figure 4.3: Z'_s of $Y_{1-y}(Ca)_yBa_2Ca_3O_{7-\delta}/SrTiO_3$ sample. *Left panel:* R'_s and the straight line giving R_f. *Right panel:* X'_s and enveloping curves $\pm R_f$.

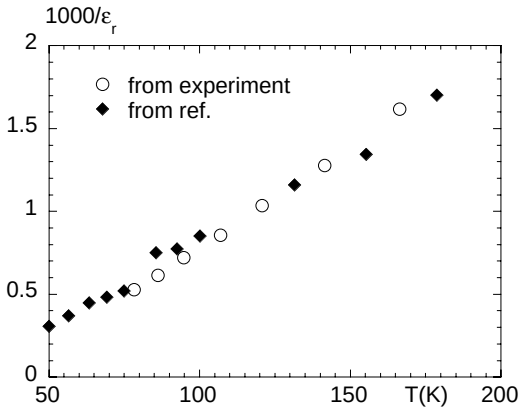

Figure 4.4: Calculated $\varepsilon_r(T)$ values at resonance and antiresonance temperatures and fit to the Curie law. Parameters are: $\varepsilon_{r0} = 81300$ K, T_0=36.3 K. Comparison with data taken from [155].

4.3 Semiconducting substrates: experimental results

Semiconducting materials, mainly Silicon (Si), are investigated as HTCS substrates for a natural integration of semiconducting-superconducting circuits and devices. They require a particular effort in order to overcome technical difficulties due to lattice mismatches as well as thermal expansion differences between the semiconductor and the HTCS. As a consequence, although buffer layers are mandatory, epitaxial films are subject to high mechanical stress which limits the achievable film thickness to approximately 50 nm [156]. This situation corresponds to a strong film transparency giving space to potentially (and effectively present [157]) important substrate effects.

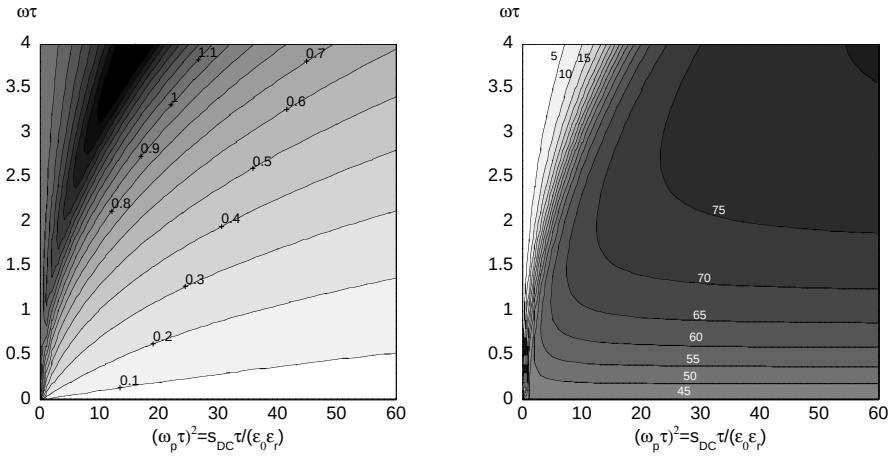

Figure 4.5: Modulus (*left panel*) and phase (*right panel*) of the bulk $Z_d/Z_{d|\sigma=0}$ versus $((\omega_p\tau)^2, \omega\tau)$. Thin lines represent isolevel-curves, their labels indicate the corresponding values. Darker regions correspond to higher values.

In fact, the semiconducting nature gives rise to a particularly rich electrodynamics, changing from insulator to conductor and having strong sensitivity to external quantities (operating temperature and frequency) and material properties (doping types and levels, technical preparation steps such as annealing). In order to transfer these considerations to quantitative grounds, a simple electrodynamic model is now built. A complex permittivity ϵ_c for the semiconductor is introduced:

$$\epsilon_c = \varepsilon_0\varepsilon_r\left(1 - \mathrm{i}\frac{\sigma(T,\omega)}{\epsilon_0\epsilon_r\omega}\right) = \epsilon_0\epsilon_r\left\{1 - \mathrm{i}\frac{[\omega_p(T)\tau(T)]^2}{\omega\tau(T)[1+\mathrm{i}\omega\tau(T)]}\right\} \tag{4.3.1}$$

which incorporates the conducting properties through the complex conductivity σ, equal to $\frac{(\omega_p\tau)^2\varepsilon_0\varepsilon_r}{\omega\tau(1+\mathrm{i}\omega\tau)}$ (ω_p and τ are the plasma angular frequency and scattering time, respectively) in a simple Drude model. For simplicity, in this expression one considers only one type of charge carriers, thus excluding compensated semiconductors. Polarization losses are also neglected, since they are typically important for higher frequencies than those here considered. The temperature dependent ω_p and τ incorporate the whole doping effects, while permittivity ε_r is taken as constant. In equation (4.3.1) ϵ_c reduces to the bare permittivity if $\sigma = 0$ ($\Leftrightarrow \omega_p = 0$), that is in the case of a intrinsic (i.e. almost insulating) semiconductor.

Considering now the surface impedance, in the case of a bulk semiconductor it can be simply written as $Z_d = \sqrt{\mu_0/\epsilon_c}$, while finite substrate thickness can be accounted for by using the full equation (4.1.4). Since, depending on

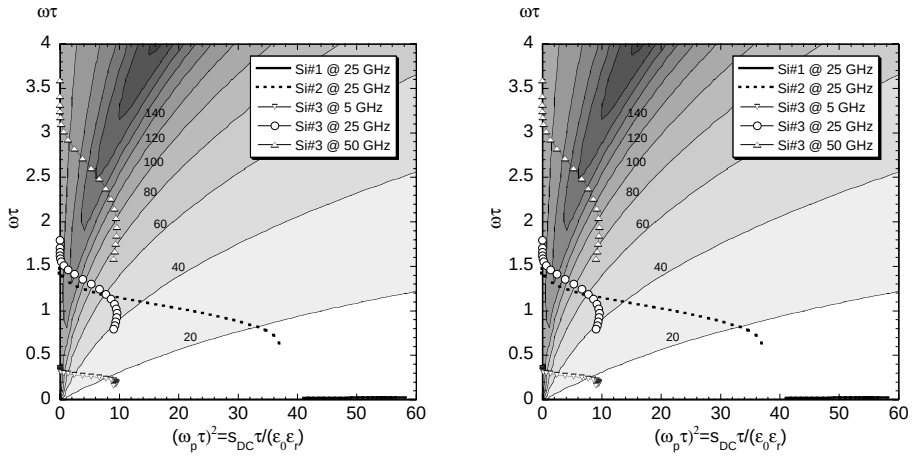

Figure 4.6: Modulus (*left panel*) and phase (*right panel*) of Z_d of Silicon versus $((\omega_p\tau)^2, \omega\tau)$. Thick lines trace the variation of Z_d as T changes from 30 K to 100 K at selected frequencies. Sample doping: $Si\#1$, $N_d = 2.7 \cdot 10^{19}$ cm^{-3}; $Si\#2$, $N_d = 1.75 \cdot 10^{16}$ cm^{-3}; $Si\#3$, $N_d = 2.1 \cdot 10^{15}$ cm^{-3}.

Z_d, the semiconductor substrate can be transparent to the em field, I preliminarily study the behavior of Z_d with respect to doping, temperature and frequency. One represents the complex Z_d, normalized to $Z_{d|\sigma=0} = \sqrt{\mu_0/\varepsilon_0\varepsilon_r}$, in a three-dimensional space as a function of normalized coordinates $(\omega_p\tau)^2$ and $\omega\tau$ (figure 4.5). Within this frame, the frequency dependence is explicitly accounted for through the vertical coordinate, while the temperature T acts on both coordinates, through $\omega_p(T)$ and $\tau(T)$. Two simple limiting cases can be recognized: a high conductivity, metal-like behaviour, in the lower-right corner region ($\sigma \propto \omega_p$), and a almost pure lossless dielectric behaviour in the upper-left corner, which corresponds to intrinsic semiconductor, obtained either without doping or at temperatures below the freezing of the charge carriers. In order to explore the temperature dependence of the substrate impedance, a real situation is considered: one specializes figure 4.5 to Silicon and traces on it (figure 4.6) the path corresponding to $Z_d(T)$. To do so, conductivity data were taken from [158] in three differently doped materials. The curves were evaluated at selected operating frequencies. In particular, sample $Si\#1$ presents an essentially metallic behaviour due to its high doping concentration. Sample $Si\#2$, having intermediate doping levels, shows how at a fixed frequency Z_d can change from dielectric to nearly metallic with increasing temperature. The behaviour of the last sample, $Si\#3$, is evaluated at three increasing frequencies. It is seen that the behaviour changes with frequency, from predominantly dielectric to predominantly metallic.

One can now show how finite thickness affects the effective Si surface

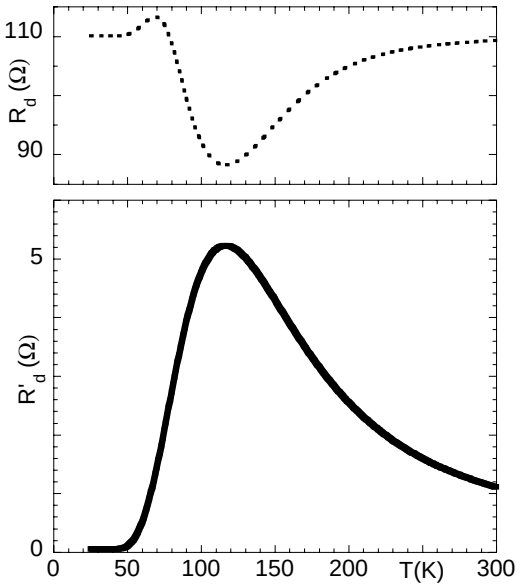

Figure 4.7: R'_d of slightly doped Silicon sample $Si\#3$ with $t_d = 290\mu$m, backed with metal plate, *lower panel*. Correspondent bulk R_d, *upper panel*.

impedance. The considered structure is a layer made of the slightly doped Silicon $Si\#3$, having thickness $t_d = 290\mu$m and backed by a metal plate of impedance Z_m. In figure 4.7 the calculated R'_d and R_d at 24 GHz frequency are shown. It is apparent how R'_d differs from R_d: in particular, the low temperature freezing of the charge carriers manifests itself with R'_d going almost to zero, as opposed to R_d showing high and almost constant values.

I now present microwave measurements in a YBCO sample grown on Si[2] which shows that the effect above described is in fact experimentally observed. A thin (t_s=80 nm) epitaxial film of YBCO has been grown onto a 10 mm $\times$10 mm buffered Silicon substrate (n-type, t_d=290 μm$\pm$10μm, room temperature resistivity of 4–6 Ωcm, $T_c \simeq 87.5$ K as estimated from the inflection point of ρ_{dc}).

The measurements of the HTCS effective surface impedance Z'_s were performed by means of the metallic cavities operating at 24 GHz and 48 GHz. Results are reported in figure 4.8 along with dc resistivity data. Data reported show many anomalous features: first of all, in the normal state ($T > T_c$) the absolute values of the surface resistance are quite high. They do not scale with $\sqrt{\nu}$ (as in the bulk limit (3.1.1)) and differs also from the dc value ρ_{dc}/t_s (as in the thin-film limit (4.1.3)). Moreover, these normal state R'_s are almost constant in the temperature range reported, contrary to the pronounced

[2]Courtesy of L. Méchin, GREYC (CNRS), France [159].

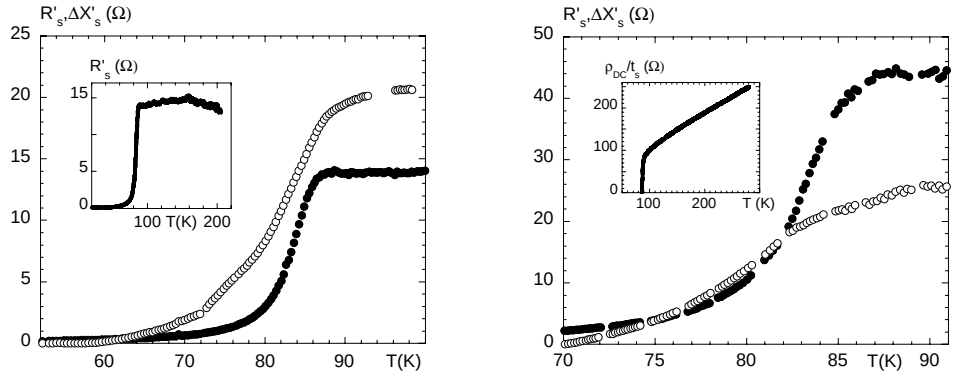

Figure 4.8: R'_s (full dots) and $\Delta X'_s$ (open symbols) of YBCO/Si film vs temperature, measured at 24 GHz (*left panel*) and 48.2 GHz (*right panel*). *Left panel inset*: R'_s at 24 GHz over a wide range of temperatures. *Right panel inset*: dc resistance per square ρ_{dc}/t_s vs temperature.

temperature dependence shown by the dc measurement. Second, if one considers the overall variation $\Delta X'_s(T)$ from well below T_c up to the normal state, one can observe that at 24 GHz it is markedly larger than the corresponding variation of R'_s, while at 48 GHz the variation of $\Delta X'_s(T)$ is smaller than the corresponding variation of R'_s.

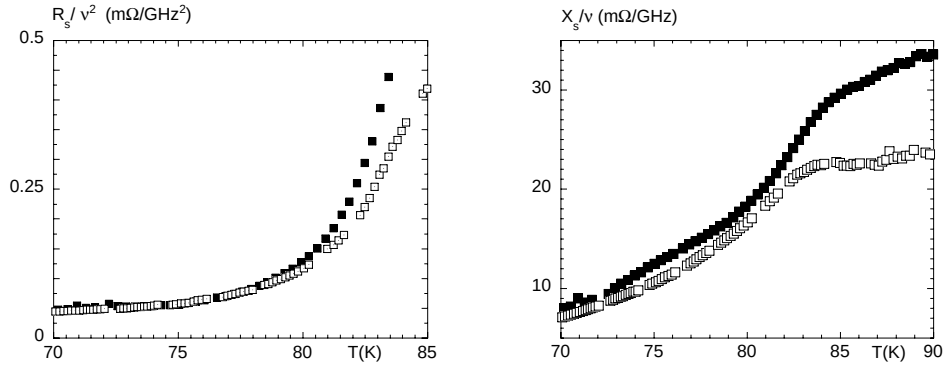

Figure 4.9: Rescaled bulk surface impedance: full squares, data taken at 23.9 GHz; open squares, 48.2 GHz. At low temperatures the scaling with frequency takes place, in agreement with (4.3.2). *Left panel*: surface resistance scaled with the frequency as R_s/ν^2. *Right panel*: bulk surface reactance scaled with the frequency as X_s/ν.

All these features find a satisfactory explanation by taking into account the Silicon substrate contribution. The full treatment is reported in appendix B: here only the main points are recalled. First, R'_d is separately measured at 24 and 48 GHz. Thus, equation (4.1.1) can be inverted and the bulk Z_s

extracted. The resulting R_s and X_s are found to follow the expected scaling R_s/ν^2 and X_s/ν (see figure 4.9), given by the simple two fluid model:

$$Z_s \simeq \frac{1}{2}\omega^2\mu_0^2\lambda^3\sigma_1 + \mathrm{i}\omega\mu_0\lambda \tag{4.3.2}$$

Summarizing, it has been shown how different substrate materials can significantly influence the effective surface impedance of the HTCS thin film. For the study of the physics of the HTCS electrodynamics, it is important to extract the complex resistivity $\tilde{\rho}$ from the measured surface impedance by means of the simplest calculation, without incurring into spurious effects. To this end, it is necessary to have a substrate giving constant and high-valued impedance. Semiconducting as well as ferroelectric materials are therefore not suitable, being the best choice given by low-loss and low-permittivity (in order to avoid substrate resonance conditions) dielectrics.

Chapter 5

Field dependence of the complex resistivity

In this chapter I present and discuss the data taken in various HTCS films using the techniques described in chapter 3. A brief summary of the chemical, structural and geometrical characteristics of the films will be given. Afterwards, for each HTCS sample the effective surface impedance Z'_s data will be described in their main features —with particular care to the measurements in varying applied magnetic field at fixed temperatures— and then discussed in detail.

5.1 Measured samples

All measurements here presented were taken in thin, high-quality superconducting films. $SmBa_2Cu_3O_{7-\delta}$, $YBa_2Cu_3O_{7-\delta}$, $Bi_2Sr_2CaCu_2O_{8+x}$ and $Tl_2Ba_2CaCu_2O_{8+x}$ were investigated extensively. Samples were 10×10 mm^2 squares of thickness t_s, grown by means of magnetron sputtering or high O_2 pressure sputtering techniques. Substrates, with thicknesses t_d=0.5–1 mm, have been carefully chosen for microwave measurements. The crystal structure was investigated by X-ray $\Theta - 2\Theta$ diffraction. The c-axis orientation was assessed by measurements of the full-width-half-maximum (FWHM) of the rocking curve of an appropriate peak. In-plane X-ray $\Phi-$scan was measured in samples Sam93, Smb6, B35, LY6 and LY8 showing excellent in-plane epitaxiality. Surface roughness was investigated by AFM over typical 1 μm $\times$ 1 μm area. All samples were nearly optimally doped or slightly overdoped. The temperature dependence of the dc resistivity or of the real part of the microwave resistivity never exhibited upward curvature above T_c. The critical temperature T_c was estimated from the inflection point of the temperature-dependent

real part of the microwave resistivity [1]. Typical ±0.5 K uncertainties in the determination of T_c are inessential for the purposes of this thesis. The resistivity ρ_0 at $T \approx 1.1T_c$ is determined from the measured real part ρ_1 in zero magnetic field. Material parameters and appropriate references are reported in table 5.1. More details on sample preparation and characterization are reported in the references (see table 5.1). All the RE-BCO (E23, Sam93 and Smb6) and BSCCO B35 have been measured by means of the 48 GHz system including the Gunn source and the metal cavity (MC). TBCCO samples have been measured using the dielectric resonator (DR), having used the metal cavity only for additional zero-field measurements. Two additional YBCO samples, LY6 and LY8, were measured earlier on through the MC and reported elsewhere [161]. They are here reported for comparison.

Sample	LY6	LY8	E23	Sam93	Smb6	B35	TS2	TS5
Material	YBCO	YBCO	YBCO	SmBCO	SmBCO	BSCCO	TBCCO	TBCCO
Substrate	$LaAlO_3$	$LaAlO_3$	YSZ/CeO_2	$LaAlO_3$	$LaAlO_3$	$LaAlO_3$	sapphire	sapphire
Thickness (nm)	220	220	200	220	220	220	240	240
$\Theta - 2\Theta$ FWHM	0.1°	0.1°	0.2°	0.2°	0.2°	N.A.	0.4°	0.4°
S.roughness RMS (nm)	2	2	N.A.	3	3	2	N.A.	N.A.
T_c (K)	89.5	89.5	88	87	87	90	104	106
ρ_0 ($\mu\Omega$·cm)	130	130	200	300	300	150	190	250
System used	MC*	MC*	MC	MC	MC	MC	DR,MC	DR,MC
References	[161, 162]	[161, 162]	[163]	[164, 165]	[164, 165]	[166]	[35]	[35]

Table 5.1: Structural and electrical characterization of the investigated samples. $\rho_0 = \rho_1$(100 K, 48 GHz) and $\rho_0 = \rho_1$(120 K, 48 GHz) in RE-BCO/BSCCO and TBCCO samples, respectively. N.A.: not available. *: measurements not done in this thesis. MC: metal cavity; DR: dielectric resonator.

Due to the small thickness values, in all the samples the thin-film approximation (equation (4.1.3)) can be used, so that $Z'_s = \tilde{\rho}/t_s$. The applicability of this approximation has been checked by numerical simulation, along [167]. The normalized resistivity $r = r_1 + \mathrm{i}r_2 = \tilde{\rho}/\rho_0$ will be often used. Two kinds of measurements are made: the transition is usually determined at zero field by changing the temperature with a rate ≈ 0.2 K/min. Field sweeps, on the other hand, are made by zero-field cooling the samples down to the desired temperature, which is then kept fixed within ±5 mK during the sweep of the field from zero to its maximum value (≈ 0.8 T). The London approximation is assumed valid, so that the magnetic induction B equals the applied $\mu_0 H$, i.e. $B \approx \mu_0 H$ [2]. Demagnetizing cycles have been performed in order to determine if irreversible magnetization effects were present: no significant hysteresis

[1] This temperature is found to coincide within ±0.5 K with the temperature where the real and imaginary parts of the microwave fluctuational conductivity are equal to each other, which is an accurate evaluation of the mean-field critical temperature [160].

[2] This approximation is applicable apart from a negligible range of few mT around 0 T. In addition, the related nonuniformities of the field penetration inside the square samples are confined to low H and in the very center of the sample [168], which is not probed by the resonator-induced currents.

was observed apart from specific cases. In particular, TBCCO only showed appreciable hysteresis and only at very low fields.

5.2 SmBCO: experimental results

I start by presenting measurements taken on two SmBCO samples (Sam93 and Smb6): their transitions, measured at 48 GHz in both real R'_s and imaginary $\Delta X'_s$ components, are reported in figures 5.1.

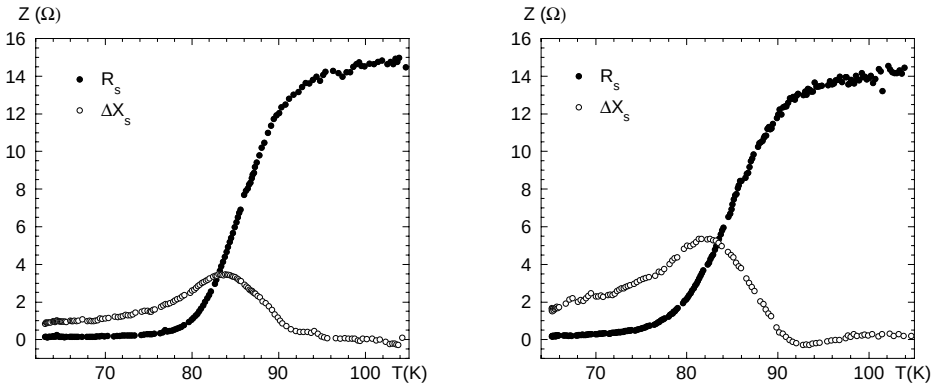

Figure 5.1: R'_s (full dots) and $\Delta X'_s$ (open symbols) of sample Sam93 (*left panel*) and Smb6 (*right panel*) measured using the 48 GHz cavity.

An extended series of magnetic field sweeps at various temperatures in the range 64–90 K was performed on both samples. In figures 5.2 and 5.3 the field-induced variation of the normalized complex resistivity, $\Delta r(\mu_0 H) = r(\mu_0 H) - r(0)$, is reported at several temperatures.

Both samples present the same experimental behaviour. The real part, Δr_1, increases with the field showing an increasing amplitude up to a typical temperature T_{max} (left panels of figure 5.2; $T_{max} \approx 82$ K in Sam93, $T_{max} \approx 79$ K in Smb6). For $T > T_{max}$ the field-induced increase lessens in amplitude by increasing T (right panels of figure 5.2). The imaginary part variation Δr_2 is positive with increasing field at lower temperatures, becomes approximately H-independent at a given T_0 and then starts to decrease with the field (figure 5.3: Sam93, with $T_0 \approx 80$ K, in left panel; Smb6, with $T_0 \approx 75$ K, in right panel). Both Δr_1 and Δr_2 exhibit a downward curvature behavior with respect to the applied field. Moreover, in most part of the temperature range $\Delta r_1 > \Delta r_2$, with the exception of the low and the high extremes of the temperature range where Δr_1 and Δr_2 are of comparable magnitude. In order to more easily identify the field dependence, the same data of figures 5.2 and 5.3 (focusing on sample Sam93) are replotted vs $\sqrt{\mu_0 H}$ in figures 5.4 and 5.5.

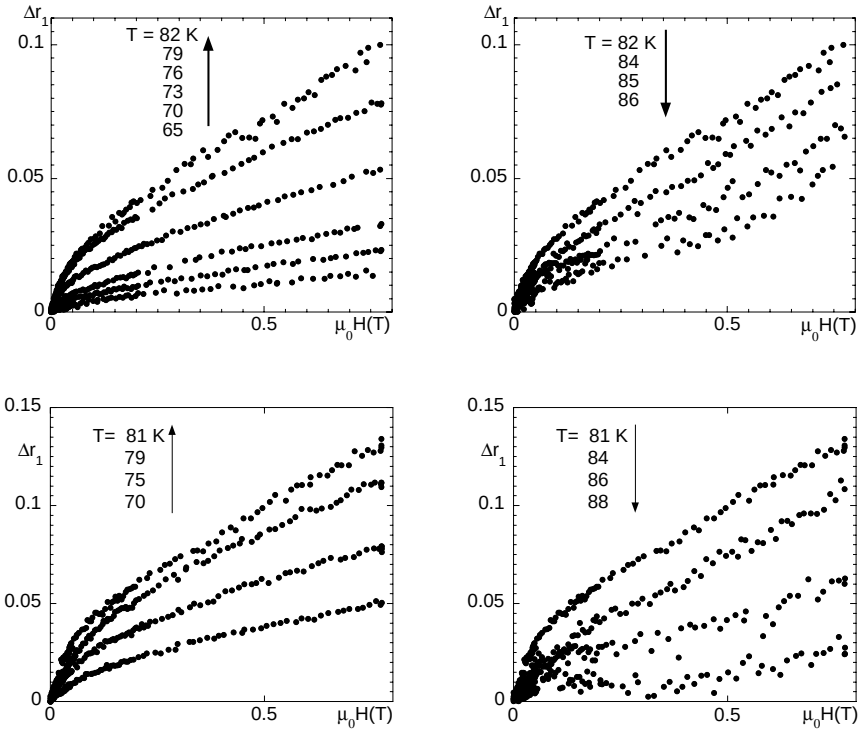

Figure 5.2: Field-induced increase of the normalized real resistivity Δr_1 for sample Sam93 (*upper panels*) and Smb6 (*lower panels*) at selected temperatures. *Left panels*: raise of Δr_1 with temperature up to T_{max} K. *Right panels*: decrease of Δr_1 with temperature increasing over T_{max}.

It is immediately seen that $\Delta r_2 \propto \sqrt{\mu_0 H}$, while Δr_1 has an upward curvature. Within the experimental uncertainty, Δr_1 is the sum of a linear and a square-root term in the applied field. Summarizing, the following empirical relation:

$$\Delta r = \tilde{b}(T)\mu_0 H + \tilde{a}(T)\sqrt{\mu_0 H} \tag{5.2.1}$$

where $\tilde{a} = a_1 + \mathrm{i}a_2$ and $\tilde{b} = b_1 + \mathrm{i}b_2$, describes the full body of the data in SmBCO with $b_2 = 0$. Interestingly, these field dependencies do not vary, neither when Δr_2 changes from positive to negative, nor when the temperature raises so that the measurements presumably cross the irreversibility line (by increasing the temperature from 65 K to T_c one certainly crosses it), nor when the temperature is raised above T_{max}. Only very close to T_c (approximately 1 K below, where strong fluctuational effects become predominant) the field dependencies empirically found appear to slightly modify and the above empirical equations no longer describe the data very accurately. All the obtained

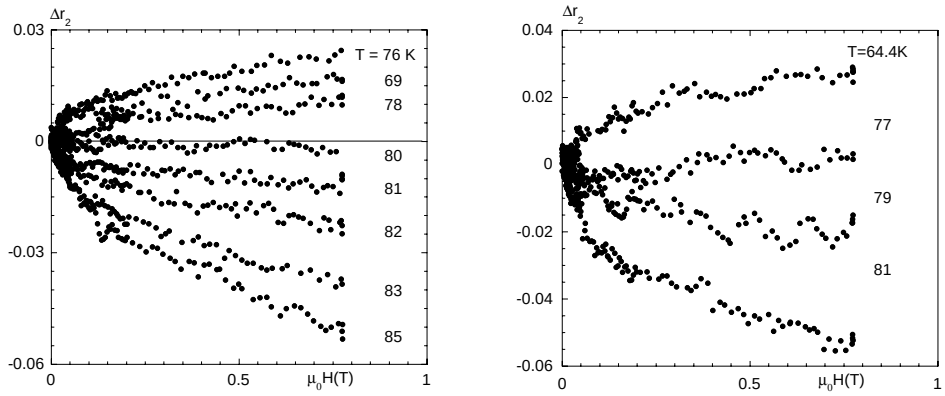

Figure 5.3: Field-induced variation of the normalized imaginary resistivity Δr_2 for sample Sam93 (*left panel*) and Smb6 (*right panel*) at selected temperatures. At $T = T_0$ the field variation changes sign.

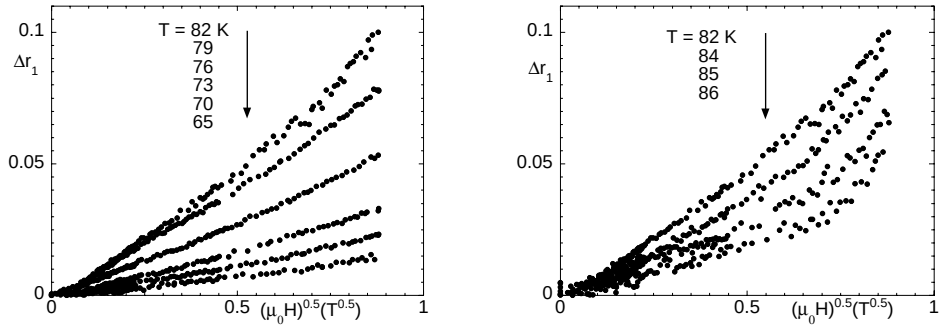

Figure 5.4: Sample Sam93: same data as upper panels of figure 5.2 vs $\sqrt{\mu_0 H}$.

coefficients in the two samples studied have the same behavior as a function of the temperature, as reported in figure 5.6 (along with fitting curves obtained by the model discussed in next section).

Together with the absence of any hysteresis, all this is a clear indication against the relevance of pinning at the measuring frequency and in favour of some "intrinsic" origin for the behaviour of the resistivity in the mixed state. Given the very clear field dependencies of the complex resistivity, I search for a theoretical frame able to describe the data, taking into account that no features appear when the irreversibility line is crossed.

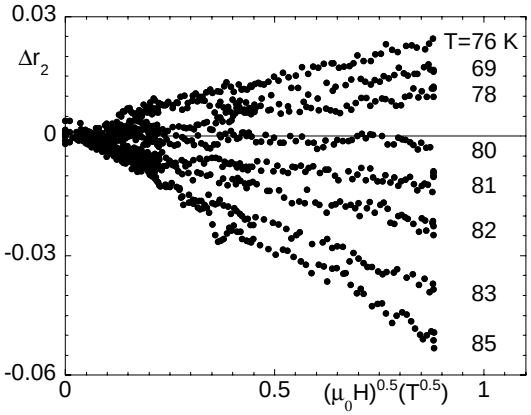

Figure 5.5: Sample Sam93: same data as left panel of figure 5.3 vs $\sqrt{\mu_0 H}$.

5.3 Generalized Coffey-Clem model for the complex resistivity

A model for the field induced Δr is hereby discussed, since the data taken in SmBCO clearly guide to the identification of the main mechanisms involved.

When discussing the data on SmBCO one faces two main experimental features: the field dependencies of r_1 and r_2, which are clearly sublinear, and the very relevant increase of the imaginary part in even moderate fields. Since the role of pinning reveals itself mostly on the imaginary part, one might be tempted to assign the strong field dependence of Δr_2 simply to a strong pinning. Within this quite conventional view, one could apply the GR model described in section 2.6: inverting the data through equation (2.6.3), one would directly obtain ν_p, η, k_p. The result of the procedure is reported in figure 5.7 for several temperatures.

As it can be seen, the so-obtained pinning frequency would be a very weak function of the applied field, in agreement with commonly reported dependencies [64]. However, the viscosity η would present a clear increase with the field (approximately as $\sim \sqrt{B}$), as reported in figure 5.7 (panel b). This dependence is not easily explained. In fact, a similar behaviour at high fields has been tentatively explained in $Bi_2Sr_2CuO_6$ [169] in terms of a peculiar field dependence of the quasiparticle relaxation time in a d-wave superconductor, appearing when the intervortex distance becomes smaller than the mean free path. However, the model would explicitly predict the usual *field independence* at low fields. Due to the field and temperature ranges here explored (by far lower than the temperature-dependent upper critical field), this picture does not seem very convincing. The anomalies become even more evident when,

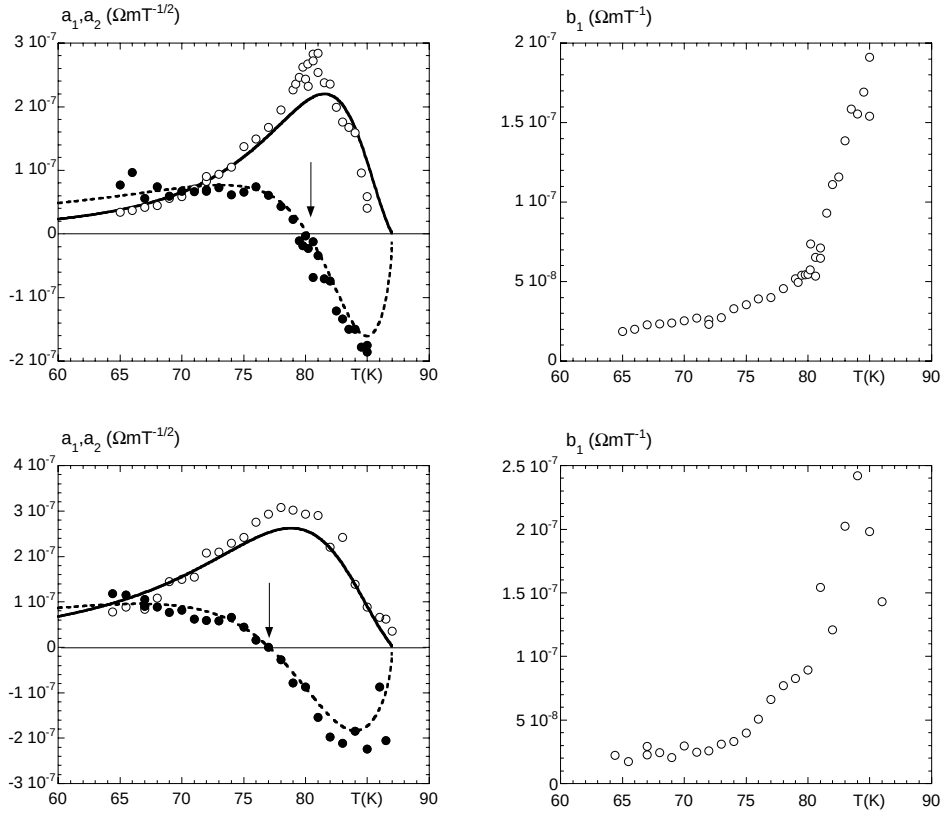

Figure 5.6: Temperature dependence of coefficients a_1, a_2, b_1 for sample Sam93 (*upper panels*) and Smb6 (*lower panels*). *Left panels*: a_1 (open symbols) and a_2 (full dots). Arrows mark the temperature T_0 where the imaginary resistivity is nearly insensitive to the applied field. Continuous and broken lines are the simultaneous fits (see next section) with equations (5.4.1) and (5.4.2), respectively. *Right panels*: b_1.

within the same GR model, one tries to obtain the pinning constant k_p from the vortex pinning frequency and the vortex viscosity: as reported in figure 5.7 (panel c), the so-obtained pinning constant would *increase* along with the field (again, approximately as a square root). This behaviour does not seem reasonable. In particular, one notes that in reference [169] k_p was found to be constant at low fields and to decrease at higher fields, as expected in high-frequency measurements. It can be concluded that an explanation of SmBCO data in terms of the GR model is at least questionable.

I now show that the empirical field dependencies for the complex resitivity can be immediately derived within a CC model, described in section 2.8, by including a field dependence of the QP fractional density in agreement with the existence of lines of nodes in the superconducting gap (section 2.7).

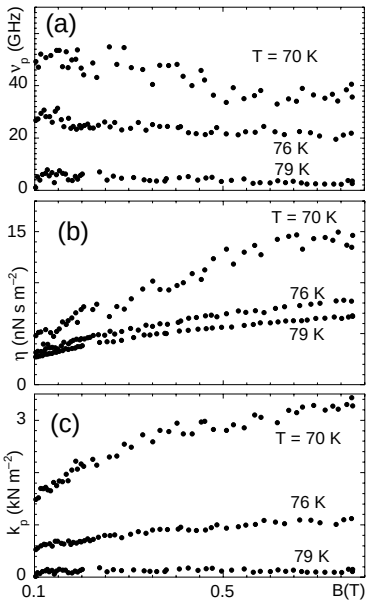

Figure 5.7: Vortex parameters as calculated from data of sample Sam93 according to the conventional Gittleman-Rosenblum model. (a): seeming pinning frequency. (b): seeming vortex viscosity. (c): seeming pinning constant. The noticeable field dependence of the so-calculated vortex viscosity and pinning constant cannot be easily justified.

I start by rewriting the general CC equation (2.8.3) in terms of complex resistivity:

$$\tilde{\rho} = \frac{1 - \mathrm{i}\sigma_2\rho_v}{\sigma_1 - \mathrm{i}\sigma_2} = \frac{1}{\sigma_1 - \mathrm{i}\sigma_2} - \mathrm{i}\frac{\sigma_2\rho_v}{\sigma_1 - \mathrm{i}\sigma_2} \tag{5.3.1}$$

where $\tilde{\sigma} = \sigma_1 - \mathrm{i}\sigma_2$ is the usual two fluid conductivity and ρ_v the complex vortex resistivity. I focus on the first member of the last equality which represents the charge carriers contribution to $\tilde{\rho}$ and thus does not depend on vortex motion. Writing the response of QP as a Drude approximation, one resorts to the usual two fluid expression (1.3.4):

$$\tilde{\sigma} = \sigma_1 - \mathrm{i}\sigma_2 = \sigma_0 \left(x_n \frac{\varpi}{1 + \mathrm{i}\varpi} - \mathrm{i}x_s \right) = \bar{\sigma} \left[x_n\varpi - \mathrm{i}(x_s + \varpi^2) \right] \tag{5.3.2}$$

where $\varpi = \omega\tau_{QP}$, $\sigma_0 = ne^2/m\omega$, $\bar{\sigma} = \sigma_0/(1 + \varpi^2)$, being τ_{QP} the QP scattering time. I incorporate the field dependence in the two-fluid conductivity, accordingly to section 2.7, through the superfluid and QP fractional densities written as follows [3] (from equation (2.7.5)):

[3]For simplicity the quasiparticle scattering time has been considered field-independent.

$$\begin{aligned} x_s(t,b) &= x_{s0}(t)(1-b^\alpha) \\ x_n(t,b) &= x_{n0}(t) + x_{s0}(t)b^\alpha \end{aligned} \tag{5.3.3}$$

where $b = B/B_{pb}$ is the field normalized with the pairbreaking field B_{pb} and $\alpha = \frac{1}{2}$ as appropriate for a superconductor with lines of nodes in the gap. Taking into account that b^α is a small parameter, one can expand these two-fluid terms to the first order in b^α. Writing down this expansion for the two-fluid resistivity, one obtains:

$$\Delta\tilde{\rho} = \tilde{\rho}(b) - \tilde{\rho}(0) = \Delta\rho_1 + \mathrm{i}\Delta\rho_2 = (\hat{a}_1 + \mathrm{i}\hat{a}_2)b^\alpha \tag{5.3.4}$$

where high order terms in b^α have been neglected[4]. The expressions for the coefficients $\hat{a}_1$ and $\hat{a}_2$ are:

$$\begin{aligned} \hat{a}_1 &= \frac{1}{\bar{\sigma}}\frac{1}{x_{n0}\varpi}\frac{1}{1+\Sigma_0^2}\frac{x_{s0}(1+\varpi^2)}{(x_{n0}\varpi)^2+(x_{s0}+\varpi^2)^2}(x_{s0}+\varpi\Sigma_0) \\ \hat{a}_2 &= \frac{1}{\bar{\sigma}}\frac{1}{x_{n0}\varpi}\frac{1}{1+\Sigma_0^2}\frac{x_{s0}(1+\varpi^2)}{(x_{n0}\varpi)^2+(x_{s0}+\varpi^2)^2}(x_{s0}\Sigma_0-\varpi) \end{aligned} \tag{5.3.5}$$

with $\Sigma_0 = \frac{\sigma_2}{\sigma_1}\Big|_{b=0} = \frac{x_{s0}+\varpi^2}{x_{n0}\varpi}$.

I now come back to equation (5.3.1) and focus on the second, vortex-related term $\rho_{v\Sigma} = -\mathrm{i}\frac{\sigma_2\rho_v}{\sigma_1-\mathrm{i}\sigma_2}$. Since, as first approximation, $\rho_v \sim$ number of vortices $\sim B$, the field expansion for $\rho_{v\Sigma}$ to the lower order yields:

$$\rho_{v\Sigma} \simeq -\mathrm{i}\left.\frac{\sigma_2}{\sigma_1-\mathrm{i}\sigma_2}\right|_{b=0}\rho_v = \frac{1}{1+\Sigma_0^2}\left(1-\mathrm{i}\frac{1}{\Sigma_0}\right)\rho_v \tag{5.3.6}$$

The field dependence of ρ_v can be extraordinarily complex (see section 2.8). However, in the present case the data can help in the simplification of the overall equation. In fact, any creep phenomena should show an upward curvature of the $\rho_1(B)$ data: this is not seen in the data. I then write the simplest tentative form for ρ_v assuming $\epsilon = 0$ (GR limit), so that $\rho_v = \frac{\Phi_0 B}{\eta}\frac{1}{1+p^2}(1+\mathrm{i}p) = \frac{\Phi_0 B}{\eta_{eff}}(1+\mathrm{i}p)$ (with $p = \nu_p/\nu$ and $\eta_{eff} = \frac{\eta}{1+p^2}$). The

However, one can show that this choice changes the subsequent equations only by a numerical factor. For example, allowing for an electron-vortex scattering like the one proposed in [170], one would only redefine the quantity $\frac{x_s}{x_n}$ in equations (5.4.1),(5.4.2).

[4]Indeed, the terms $b^{2\alpha}$ have been determined. Once computed with all the numerical quantities obtained through this whole procedure, they resulted negligible with respect to both b^α and b terms arising from vortex dynamics.

latter assumption is further supported by the experimental fact that the data do not show any detectable feature with increasing temperature from below to above the irreversibility line. $\rho_{v\Sigma}$ can be therefore cast in the form:

$$\rho_{v\Sigma} = \frac{1}{1+\Sigma_0^{-2}} \frac{\Phi_0 B}{\eta_{eff}} \left[\left(1 + \frac{p}{\Sigma_0} \right) - \mathrm{i} \left(\frac{1}{\Sigma_0} - p \right) \right] = (\hat{b}_1 + \mathrm{i}\hat{b}_2) b_v \qquad (5.3.7)$$

having defined the normalized field $b_v = \frac{B}{\rho_0 \eta_{eff}/\Phi_0} = B/B_\eta \approx B/B_{c2}$.

It is worth noting that equation (5.3.7) determines a B-linear term for the imaginary resistivity. Within this method, the absence of a linear term in the field variation of the imaginary part is a signature of a vortex motion with $p \ll 1$ ($\Sigma_0 \gg 1$ is usually verified below T_c): this is the high frequency, small oscillation, regime due to high frequency operating frequency, corresponding to flux flow. Since $\hat{b}_2 = 0$, η_{eff} reduces to η.

5.4 SmBCO: discussion

I now apply the extended CC model developed above to the data taken in SmBCO. In this case, the field variations of the experimental complex resistivity should then be compared to the model with:

$$\Delta\rho_1(B) = \hat{a}_1 \left(\frac{B}{B_{pb}} \right)^{\frac{1}{2}} + \hat{b}_1 \frac{B}{B_\eta} \equiv a_1(T) B^{\frac{1}{2}} + b_1(T) B \qquad (5.4.1)$$

$$\Delta\rho_2(B) = \hat{a}_2 \left(\frac{B}{B_{pb}} \right)^{\frac{1}{2}} \equiv a_2(T) B^{\frac{1}{2}} \qquad (5.4.2)$$

As a first result, it can be noted that the functional field dependencies that have been empirically found in the data are predicted by the model. This is one main results: the experimental field dependence of the complex resistivity, not explainable in the framework of fluxon motion only, is captured by a model that includes simple free flux line oscillation (corresponding to flux flow resistivity) and the essential role of superfluid depletion in a superconductor having lines of nodes in the gap. As a further important result, it can be noted that the a_1 and a_2 coefficients here defined present the same qualitative features as in the experimental values: on one side, the study of equation (5.4.1) reveals that a_1 presents a peak; more important, it is immediately seen that a_2 undergoes a sign change at such temperature that:

$$x^*_{s0}\Sigma^*_0 = \varpi \;\Rightarrow\; \varpi = \sqrt{\frac{x^*_{s0}}{x^*_{n0} - x^*_{s0}}} \qquad (5.4.3)$$

Summarizing, the model here developed contains all the experimental features present in the data: the field dependencies of the complex resistivity and the behavior with the temperature of a_1 and a_2, including the change of sign of a_2.

For a quantitative fit of the data with the theoretical expressions, one has to determine the temperature dependencies of the parameters contained in equations (5.4.1),(5.4.2). Exploiting the similarities with YBCO and the vicinity to T_c, I have taken $x_{s0} = (1-t)$ and $x_{n0} = t$, and $B_{pb} = B_{pb0}\,(1-t)$. To my knowledge there are no detailed studies of the finite frequency conductivity in SmBCO that could give indications on the temperature dependence of the QP scattering time: I then make the very crude assumption that the QP scattering time is temperature-independent. With this choice, on the basis of the constraint given by equation (5.4.3) one has $\omega\tau_{QP}$ =0.085 and 0.13, yielding τ_{QP}=0.28 ps and 0.43 ps, in sample Sam93 and Smb6, respectively. The simultaneous fits of $a_1(T)$ and $a_2(T)$ contain only $\sigma_0\sqrt{B_{pb0}}$ as a common scale factor. In left panels of figure 5.6 the coefficients a_1 and a_2 are plotted, compared to the theoretical curves computed on the basis of equations (5.4.1),(5.4.2). Taking B_{pb0} =100 T, one has $\sigma_0 = 10^7\ \Omega^{-1}\mathrm{m}^{-1}$ and $4.5\cdot 10^6\ \Omega^{-1}\mathrm{m}^{-1}$ in sample Sam93 and Smb6, respectively.

The numerical values of ϖ are larger by a factor ~ 30 than expected with $\rho_0 \simeq 280\ \mu\Omega$cm and $\lambda_0 \sim 2000$Å. However, this is consistent with the findings in the parent compound YBCO below T_c [12, 171]. Moreover, the numerical values τ_{QP} compare surprisingly well to findings in YBCO: at 80 K, is found τ_{QP} =0.2 ps in crystals [12] and 0.5 ps in films [171] (with $\omega/(2\pi)$=48.2 GHz). Given the crudeness of the model and the absence of fit parameters ($\sigma_0\sqrt{B_{pb0}}$ is an overall scale factor), the theoretical expectations describe with surprising accuracy the data. The essential physics of the field dependent microwave response is likely to be related to the effects extensively described in this section.
Lastly, I discuss the fluxon dynamics. Within the present interpretation, it is entirely described by the coefficient b_1. Using for Σ_0 the determinations obtained from a_1 and a_2 above, one immediately gets the fluxon viscosity η, as reported in figure 5.8.

As it can be seen, the data for η attain the same value in both samples, indicating that the physics in the vortex core is related to sample-independent processes.

As a final remark, it is worth reminding that the quantitative description of the vortex state microwave response here presented could be accomplished only with the essential inclusion of the enhanced QP increase in a magnetic

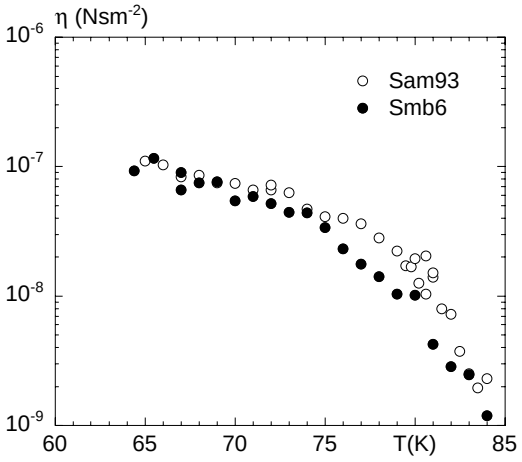

Figure 5.8: Vortex viscosity in SmBCO samples.

field. A description in terms of fluxon motion only would give very unlikely dependencies of the vortex parameters.

5.5 YBCO: results and discussion

The YBCO sample E23, measured by means of the 48 GHz cavity, presents the transition reported in figure 5.9.

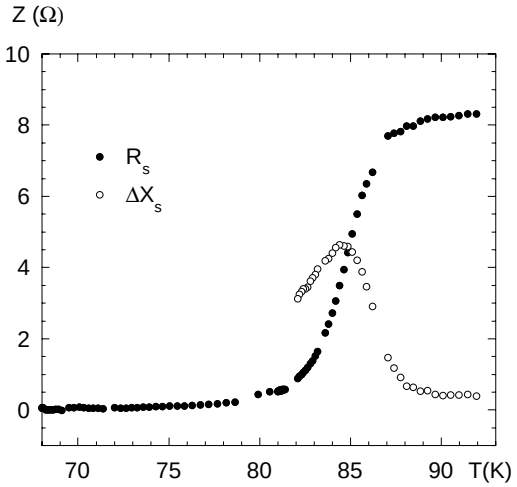

Figure 5.9: R'_s (full dots) and $\Delta X'_s$ (open symbols) of sample E23 measured with the 48.2 GHz cavity. In this case, the cavity background was not found to be regular, so the data for the reactance are truncated below ~ 82 K.

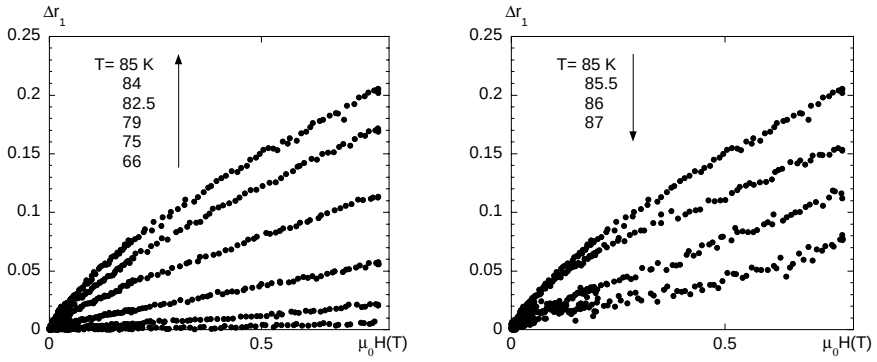

Figure 5.10: Field-induced increase of the normalized real resistivity Δr_1 for sample E23 at selected temperatures. *Left panel*: raise of Δr_1 with temperature up to $T_{max} \approx 85$ K. *Right panel*: decrease of Δr_1 with temperature increasing over T_{max}.

Field sweeps were done in a temperature range of 63–90 K. In figures 5.10 and 5.11 $\Delta r(\mu_0 H) = r(\mu_0 H) - r(0)$ is reported at several temperatures. Data are reminiscent of those of the SmBCO samples but present some differences. Δr_1 is greater than Δr_2 only for the lower temperatures, while going near to T_c the absolute variation of Δr_2 becomes larger than Δr_1. Δr_1 always increases with the field: its variation amplitude first increases with temperatures up to $T_{max} \approx 85$ K and then decreases. It also presents a downward curvature, analogous to SmBCO data but less marked. Δr_2 presents a small positive variation up to $T_0 \approx 82$ K, while above it presents negative variations. As for the real part, Δr_2 shows a curvature which is less marked with respect to SmBCO data. In particular, it is evident only at higher temperatures ($T \gtrsim 85$ K). Analogously to SmBCO, it is seen that Δr can be empirically described by equation (5.2.1). However, differently from SmBCO, in YBCO one has to take $b_2 \neq 0$. The resulting coefficients are plotted as a function of temperature in figure 5.12 (along with fits described later on).

Other YBCO samples (LY6 and LY8, data taken from [161]) gave similar results and considerations as exemplified in figures 5.13 and 5.14.

Discussion

YBCO data show qualitatively a behaviour similar to SmBCO data apart from three aspects: Δr variations with B are small in comparison with the maximum variation attained near T_c in the great majority of the temperature range observed (which determines a much larger scattering in the $a_{1,2}$ and $b_{1,2}$ parameters). Moreover, near T_c Δr_2 presents an absolute variation greater than Δr_1. Last, together with Δr_1, Δr_2 too presents a sublinear B dependence

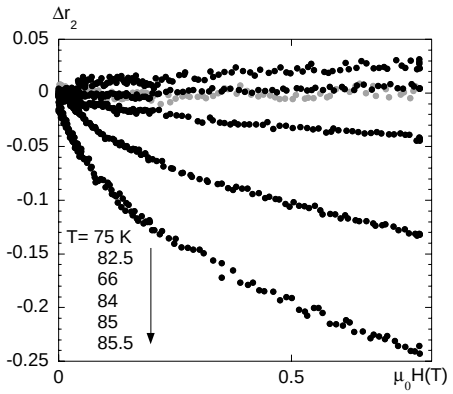

Figure 5.11: Field-induced variation of the normalized imaginary resistivity Δr_2 for sample E23 at selected temperatures. Up to $T_0 \approx 82$ K the field variation is positive, while above T_0 it becomes negative.

which requires both linear and square roots terms to be described. Starting from the similarity with SmBCO, I perform a modelling analogous to the one followed for SmBCO but with non zero $\hat{b}_2$ coefficient (equation (5.3.7)). As a consequence, the pinning term $p \neq 0$. Within this framework one comes up with a couple of equations:

$$\Delta r_1(B) = \frac{\hat{a}_1}{\rho_0}\left(\frac{B}{B_0}\right)^{\frac{1}{2}} + \frac{\hat{b}_1}{\rho_0}\frac{B}{B_{c2}} \equiv b_1(T)B + a_1(T)B^{\frac{1}{2}} \qquad (5.5.1)$$

$$\Delta r_2(B) = \frac{\hat{a}_2}{\rho_0}\left(\frac{B}{B_0}\right)^{\frac{1}{2}} + \frac{\hat{b}_2}{\rho_0}\frac{B}{B_{c2}} \equiv b_2(T)B + a_2(T)B^{\frac{1}{2}} \qquad (5.5.2)$$

which, again, analytically correspond to the empirical expressions describing the measured $\Delta r(B)$ (equation (5.2.1)). The a_1, a_2 and b_1 coefficients analytically present the same features as their experimental counterparts, as observed before. In addition, the b_2 coefficient too reproduces the sign change of the experimental b_2 in correspondence to a temperature such that:

$$1 - \Sigma_0 p = 0 \qquad (5.5.3)$$

I first fit the temperature dependence of $a_1(T)$ and $a_2(T)$. It can be noted that the small change of $\Delta\rho_2(\mu_0 H)$ determines a rather high scattering of $a_2(T)$. As a consequence, the best fit is determined by $a_1(T)$. Fits reported in figure 5.12 determined the parameters $\omega\tau_{QP} = 0.05$ and, taking B_{pb0} =100 T, $\sigma_0 = 2.5 \cdot 10^6\ \Omega^{-1}\mathrm{m}^{-1}$. It is seen that the model applies very well to a_1, while

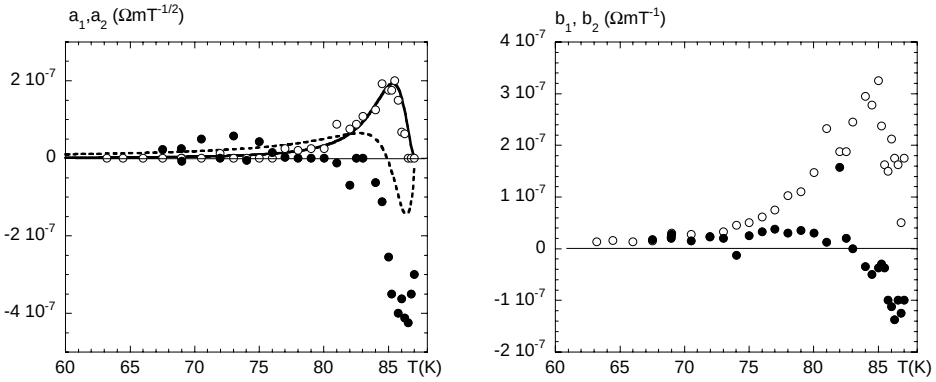

Figure 5.12: Temperature dependence of coefficients a_1, a_2, b_1 and b_2 for sample E23. *Left panel*: a_1 (open symbols) and a_2 (full dots). Continuous and broken lines are the simultaneous fits (see the text) with equations (5.5.1) and (5.5.2), respectively. *Right panels*: b_1 (open symbols) and b_2 (full dots).

for a_2 it is only qualitative. Nevertheless, the information coming from those fits and from the following analysis of $b_1(T)$ and $b_2(T)$ contributes to build a consistent framework. On the basis of the model, it is seen that:

$$-\frac{b_2}{b_1} = \frac{\hat{b}_2}{\hat{b}_1} = \frac{1 - \Sigma_0 p}{\Sigma_0 + p} \tag{5.5.4}$$

From this equation, using the experimental b_1 and b_2 and Σ_0 given by the fits of a_1, one obtains the (de)pinning frequency reported in left panel of figure 5.15. As expected, ν_p decreases slightly with temperature, and attains rather high values. The vortex viscosity can be obtained either from b_1 of from b_2, inverting equation (5.3.7). The result is reported in right panel of figure 5.15.

Equations (5.3.7) can be inverted, giving reasonable figures for ν_p and η, and this is a noteworthy consistency check indeed. As a final remark on the vortex parameters, it can be noted that all the measured viscosities in RE-BCO films scale on the same curve with numerical factors ~ 1 (figure 5.16). Moreover, the data points taken with Corbino technique [175] and taken at three different frequencies in YBCO crystals [65] scale also on the same curve, suggesting a common behaviour for the electronic states in the vortex cores of SmBCO films, YBCO films and YBCO crystals.

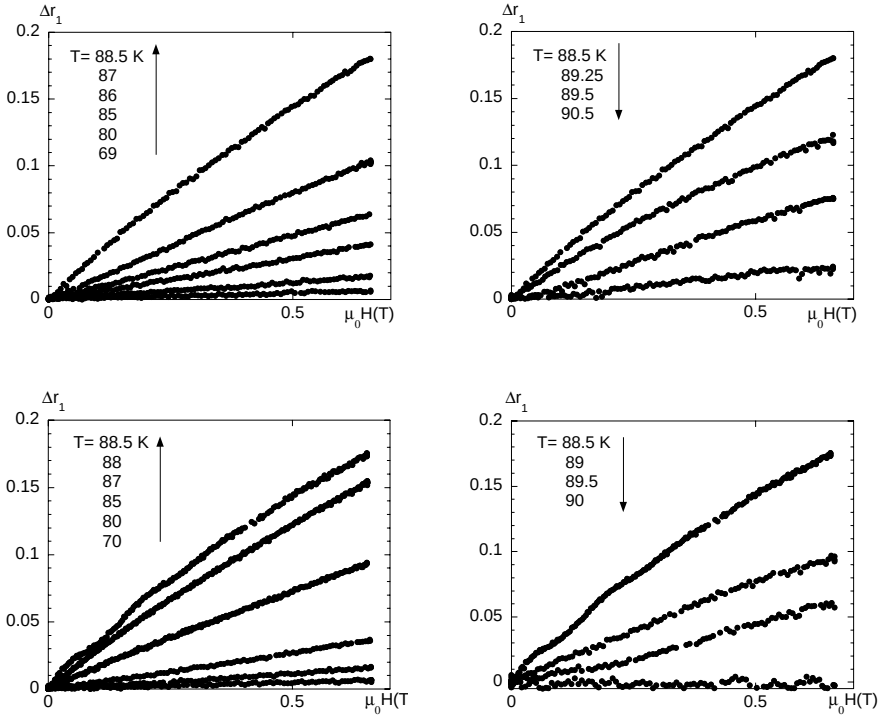

Figure 5.13: Field-induced increase of the normalized real resistivity Δr_1 for sample LY6 (*upper panels*) and LY8 (*lower panels*) at selected temperatures. *Left panels*: raise of Δr_1 with temperature up to $T_{max} \approx 88$ K. *Right panels*: decrease of Δr_1 with temperature increasing over T_{max}. It can be noted that the field behaviour is similar to sample E23.

5.6 BSCCO: experimental results

I report here for completeness and briefly discuss the measurements on the BSCCO sample performed by means of the metal cavity. The measured transition is reported in left panel of figure 5.17. It is seen that, despite the good structural data, the superconducting transition is very broad. Moreover, it extends above the temperatures appropriate to T_c Bi:2212 systems. This can be evidence for strong superconducting fluctuations or Bi:2223 inclusions. Inhomogeneities (corresponding to a distribution of different critical temperatures) are almost certainly present. As a consequence, the field dependencies must be intended as "average" behaviours.

Field sweeps measurements have been taken in the temperature range between 78 K and 95 K. The field behavior of the variation of the normalized real resistivity Δr_1 is shown in the left panel of figure 5.18 for selected temperatures. It can be seen that Δr_1 is positive with increasing field and its

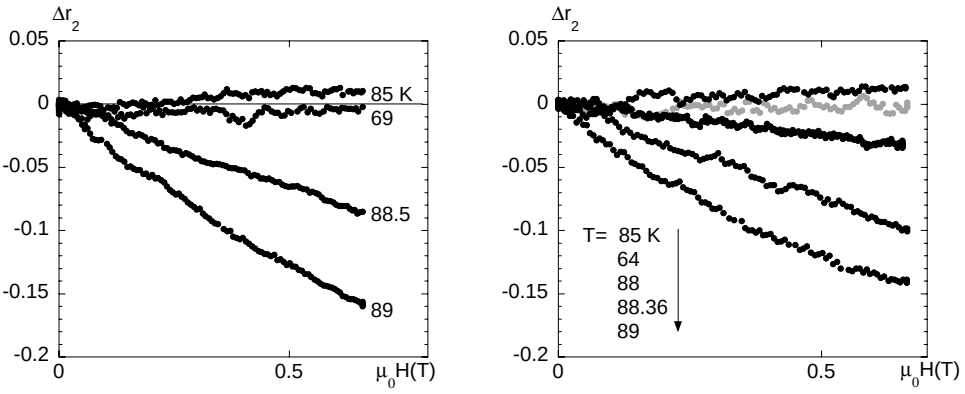

Figure 5.14: Field-induced variation of the normalized imaginary resistivity Δr_2 for sample LY6 (*left panel*) and LY8 (*right panel*) at selected temperatures. At $T = T_0 \approx 88$ K the field variation changes sign. It can be noted that the field behaviour is similar to sample E23.

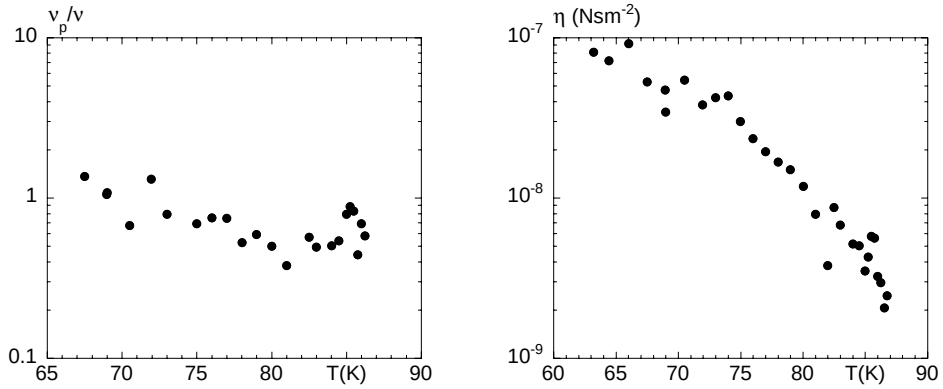

Figure 5.15: Normalized pinning frequency ν_p/ν and vortex viscosity η for sample E23, extracted from data within the described model.

amplitude decreases as the sample warms up and vanishes for $T \approx 95$ K$> T_c$. Contrary to the behaviour in RE-BCO, with increasing temperatures the field dependence changes from a clear downward curvature to a behaviour essentially linear in $\mu_0 H$. Δr_2 (right panel of figure 5.18) is negative (apart a steep positive rise exhibited only at the lowest temperatures), while its amplitude increases with temperature rising up to ≈ 90 K and then decreases, vanishing near 95 K. $\Delta r_1 > \Delta r_2$, apart from $T \simeq 90$ K where they are comparable.

Scattering of Δr_2 prevents from a proper determination of the empirical field dependence. For the real part Δr_1, on the other hand, it is possible to fit the data with the empirical relation 5.2.1, yielding the temperature behaviour of coefficients a_1 and b_1 reported in right panel of figure 5.17. At low temper-

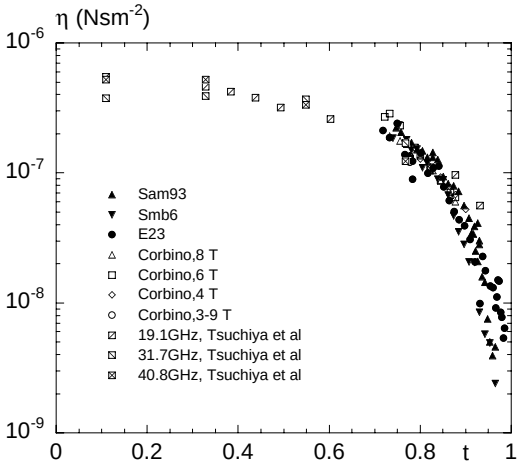

Figure 5.16: Vortex viscosity as a function of the reduced temperature t in SmBCO (black triangles), in YBCO E23 (full dots), in other YBCO films measured with the Corbino technique [175] at different field values (open symbols) and in YBCO crystals from reference [65] for three different frequencies (barred squares) as a function of the reduced temperature. Data in SmBCO are scaled by a factor 2, E23 by a factor of 2.6.

atures, $T < 83$ K, Δr_1 is essentially $\propto \sqrt{H}$; at intermediate temperatures, 83 K$< T <$87 K, it is an admixture of linear and square root terms; at higher temperatures it is mainly linear. The linear field dependence appears to be detectable only across T_c (also above). Conversely, at the lower temperatures Δr_1 presents large field-induced variations, almost purely $\propto \sqrt{H}$. In addition, Δr_2 is large where $\Delta r_1 \sim H$ and drops below the sensitivity where $\Delta r_1 \sim \sqrt{H}$.

Those behaviours are at odds with most of the expected dependencies. Pinning appears to be absent, as deduced from $\Delta r_1 \gg \Delta r_2$ at low temperatures. In the flux flow regime one should have $\Delta r_1 \sim H$; this is the case only close to (and above) T_c, where by contrast Δr_2 is large and negative. Choosing an alternative mechanism, such as nodal QP pairbreaking, Δr_1 should be $\sim \sqrt{H}$. However, the amplitude should increase with increasing temperatures, while the $\sqrt{H}$ dependence on Δr_1 decreases and vanishes for $T > 87$ K. It is not clear whether exotic field dependencies of vortex parameters could account for the observed behaviours. Summarizing, these puzzling BSCCO data escape to conventional interpretations, thus presumably requiring additional effects. However, the data seem to point to two separate mechanisms, one ending at $T \approx 88$ K and another existing only across T_c. The temperature range of the broad transition has significant overlap with the temperature range where $b_1 \neq 0$. Thus, a tentative interpretation of this mechanism in terms of superconducting fluctuations is quite natural. At this stage, one cannot possible to identify the fluctuation-driven mechanism responsible for the observed

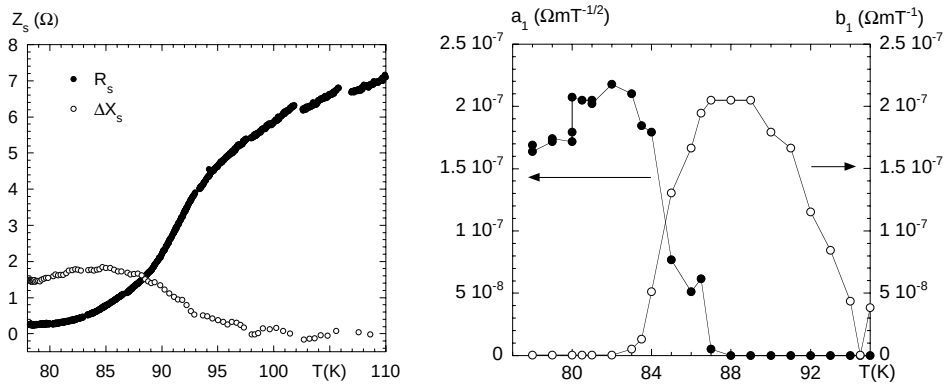

Figure 5.17: *Left panel*: R'_s (full dots) and $\Delta X'_s$ (open symbols) of sample B35 measured with the 48.2 GHz metal cavity. *Right panel*: a_1 and b_1 coefficients vs temperature.

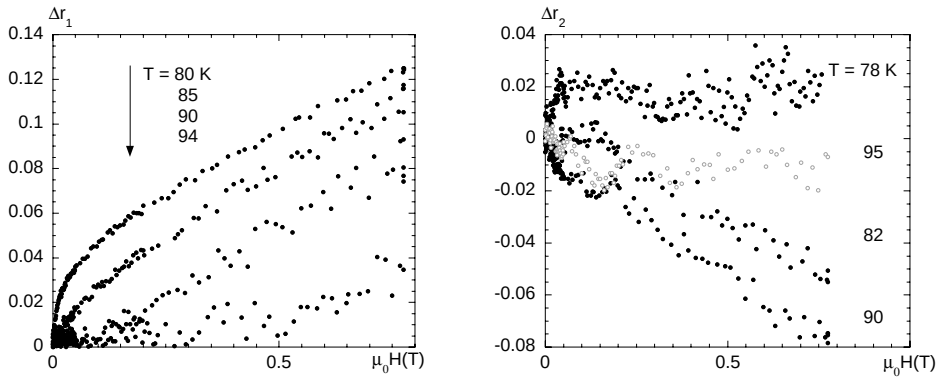

Figure 5.18: Normalized field-induced variation of the resistivity for sample B35 at selected temperatures. *Left panel*: decrease of Δr_1 amplitude with increasing temperature. *Right panel*: Δr_2 vs field. Amplitude increases up to $T \approx 90$ K, then decreases to zero as $T \to 95$ K.

dependence: order-parameter (amplitude) fluctuations and vortex-antivortex creation and motion are equally possible candidates. I conclude that the field dependence of the microwave resistivity in BSCCO is still an elusive matter and requires further studies.

5.7 TBCCO: experimental results

Two TBCCO films (TS5 and TS2) from the same batch were investigated. The superconducting transitions, measured with the dielectric resonator at 47.6 GHz, are reported in figure 5.19 for both samples. Comparison with the measurements taken by means of the metal cavity has been given in section 3.6.5.

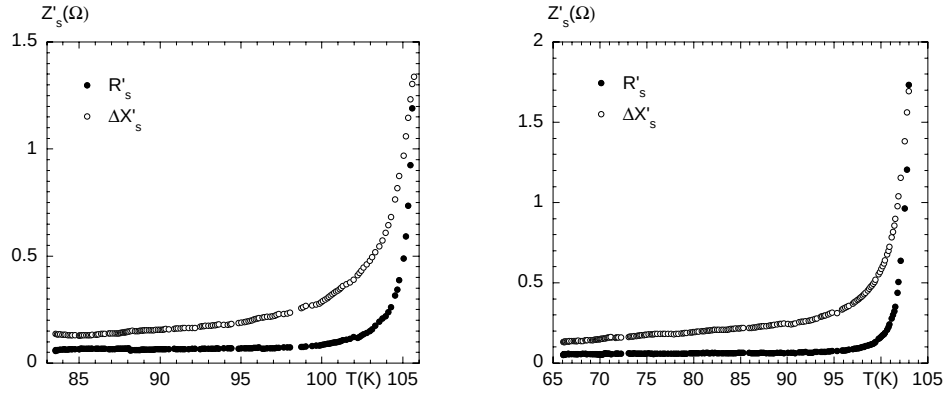

Figure 5.19: $Z'_s(T)$ of TS5 and TS2 (*left* and *right panel*, respectively) measured at 47.6 GHz with the dielectric resonator.

Extensive measurements of $\Delta R'_s + \mathrm{i}\Delta X'_s$ as a function of the applied field were performed with the dielectric resonator, in the temperature range 58–105 K. The smaller mass of the dielectric resonator allowed for a lower base temperature with respect to the metal cavity.

Typical field sweeps for the normalized resistivity change in sample TS5 are reported in figure 5.20 and 5.21 for the real and imaginary parts, respectively.

Sample TS2 exhibited a nearly identical behaviour: comments to the measurements on TS5 apply to TS2 as well. As can be seen, the field dependence of the complex resistivity in TBCCO exhibits a much richer behaviour with respect to the other cuprates investigated in this thesis. Starting from lower temperatures, in most of the field range explored Δr_1 increases with upward curvature (as opposed to the behaviour in other cuprates). At very low dissipation levels (see enlargement at low fields in figure (5.20)) a steep rise at low fields develops. This feature can be detected, with lower and lower amplitude and in smaller and smaller field ranges, in the whole temperature range explored. It should be emphasized that the largest amplitude of this feature is ≈ 0.1 % of the normal state: it has been possible to observe the feature only thanks to the much enhanced sensitivity of the dielectric resonator.

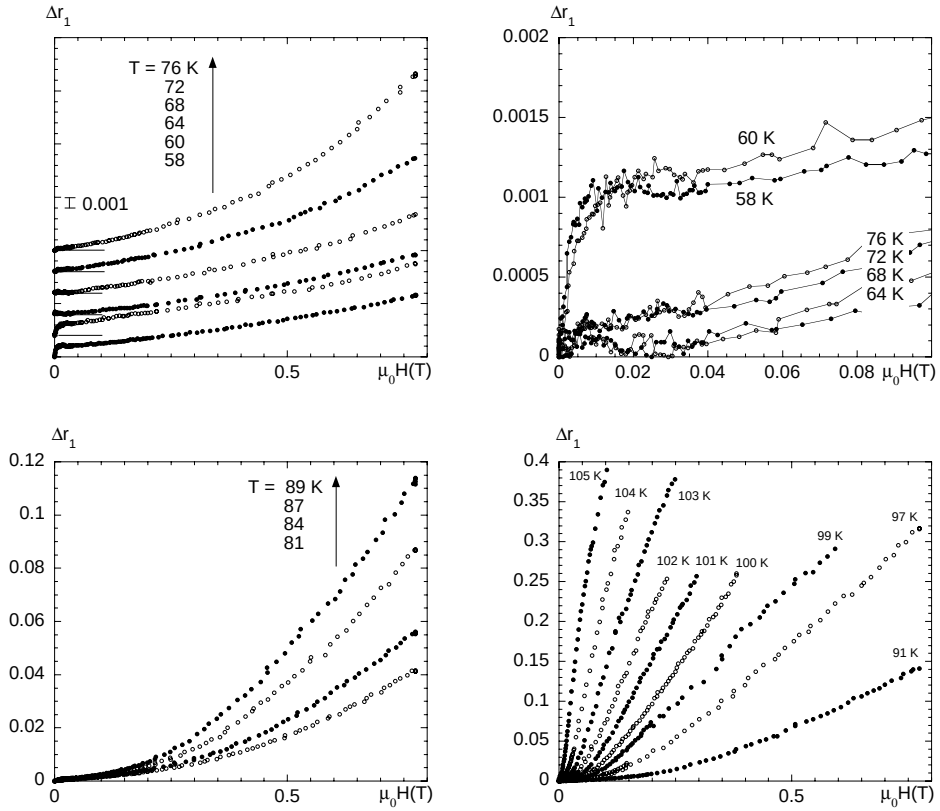

Figure 5.20: Field-induced increase of the normalized real resistivity Δr_1 for sample TS5. *Upper left panel*: 58–76 K; measurements are offset for clarity. *Upper right panel*: 58–76 K, enlargement at low fields. Note the resolution of the measurements taken with the dielectric resonator: the full scale is 0.2% of the normal state. *Lower left panel*: 80–90 K. *Lower right panel*: 91–105 K.

In the same temperature and field ranges, Δr_2 exhibits an even more complex behaviour: at low temperatures it increases with upward curvature, with $\Delta r_2 > \Delta r_1$. With increasing temperatures, a wide maximum shows up, and eventually Δr_2 decreases below the zero-field value. It is remarkable that, in the temperature and field range of the non-monotonic behaviour of Δr_2, Δr_1 does not present any detectable variation of field dependence. Lastly, at low fields a feature similar to the one observed in Δr_1 is present, with the additional peculiarity of a non-monotonous behaviour at the lowest temperatures investigated.

It should be noted that the low field features are affected by strong hysteresis, while the field dependence of the complex resistivity above the low-field feature does not present any noticeable hysteresis.

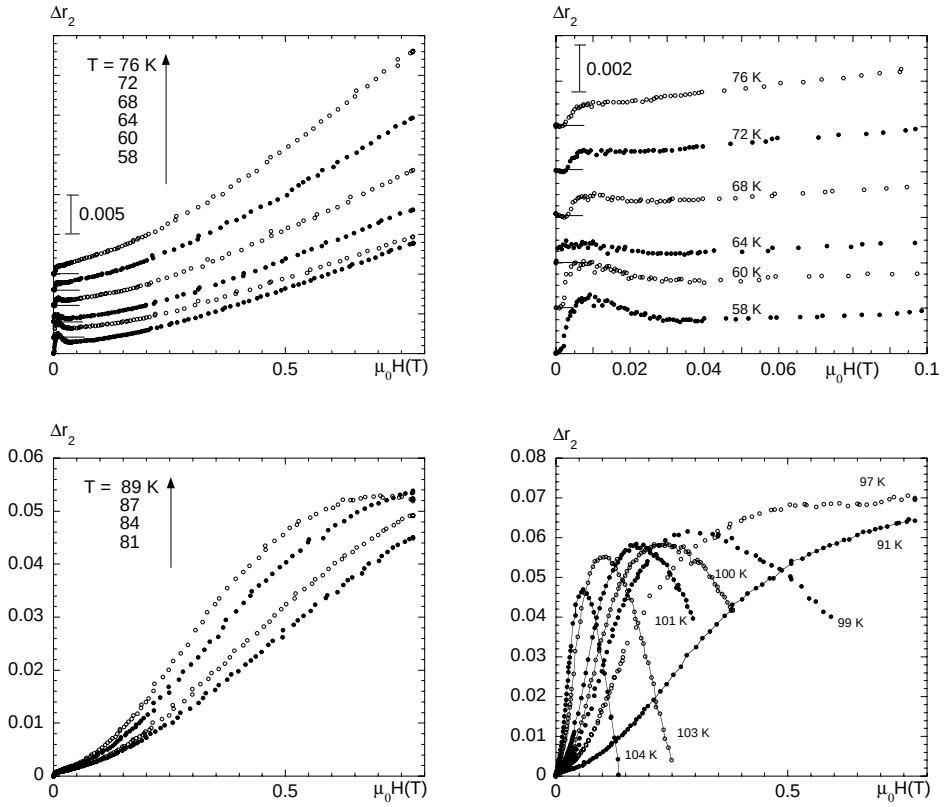

Figure 5.21: Field-induced increase of the normalized imaginary resistivity Δr_2 for sample TS5. *Upper left panel*: 58–76 K; measurements are offset for clarity. *Upper right panel*: 58–76 K, enlargement at low fields. *Lower left panel*: 80–90 K. *Lower right panel*: 91–105 K.

5.8 TBCCO: discussion

The data in TBCCO clearly present many features not observed in the other cuprates investigated. While the low field feature could be observed only thanks to the sensitivity of the dielectric resonator, other characteristics (upward curvature, maximum in Δr_2, $\Delta r_2 > \Delta r_1$ in a wide temperature range) mark a clear difference of TBCCO with respect to RE-BCO (and in part to BSCCO). It is remarkable that the field dependence is so different from the measured response in the isomorphic compound BSCCO.
I discuss first the low field feature and then I will focus on the scaling behaviour of the complex resistivity change.

Low fields

The behaviour of the low field complex resistivity, the steep raise followed by a saturation, accompanied by hysteresis, is reminiscent of the field dependence of the response of a network of Josephson junctions [176, 177, 178, 179]. In order to put on quantitative grounds the low field feature observed, one can identify a few characteristic fields: $H_{p,l}$ is the field corresponding to the low-T peak on Δr_2, $H_{p,h}$ is the field value of the high-T maximum on Δr_2, $H_{s,1}$ and $H_{s,2}$ correspond to the half-value of the initial steps shown by Δr_1 and Δr_2, respectively. It is seen that $H_{s,1}$ and $H_{s,2}$ essentially coincide in the whole temperature range. In figure 5.22 the characteristic fields in both samples are reported.

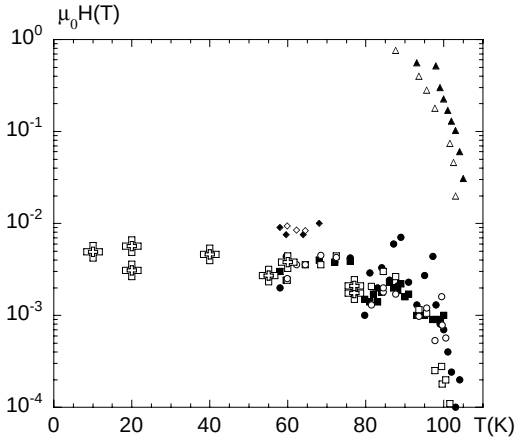

Figure 5.22: Characteristic fields vs temperature of the samples TS5 (black symbols) and TS2 (white symbols). Squares: $H_{s,1}$; circles: $H_{s,2}$; diamonds: $H_{p,l}$; triangles: $H_{p,h}$. Crosses: threshold field for nonlinear dissipation determined in reference [180].

It is apparent that all the characteristic fields in both samples agree with one another, further indicating the equivalence of the samples even in this very peculiar feature. Moreover, all fields but $H_{p,h}$ describe the same trend, indicating that they refer to the same physical mechanism. Additional insight can be gained by comparison with nonlinear surface impedance measurements on similar samples [180]: in fact, the characteristic fields here reported agree quantitatively with the threshold field for nonlinear dissipation (crosses in figure 5.22), that has been ascribed to the motion of Josephson or Abrikosov-Josephson fluxons [181, 182] in grain boundaries [180] (see appendix C).
Summarizing, the low field features of the field dependent microwave linear complex resistivity in the TBCCO samples indicate the existence of Josephson-like grain boundaries.

Scaling properties

I here discuss the overall field dependence of the largest part of the complex resistivity, with no reference to the low field behaviour above described.
A complicated field dependence such as the one exhibited by the present measurements would led to intrinsically complicated models, where the field dependence of the parameters would play a major role. Tentative fits with the Coffey-Clem model gave contradictory results and (most important) were not found to be sufficiently unambiguous. I then exploit in this section some very general characteristic of the measurements, without pretending to describe quantitatively the complex response. In passing, it can be noted that the situation is again quite different than it is in RE-BCO, where a simple (albeit algebraically complicated) model having few parameters was able to take into account most of the observed data.
A proper representation of the data is extremely useful to the above-described goal. As a first step, in figure 5.23 I examine the data in the impedance plot of $\Delta X'_s$ vs $\Delta R'_s$ in both samples.

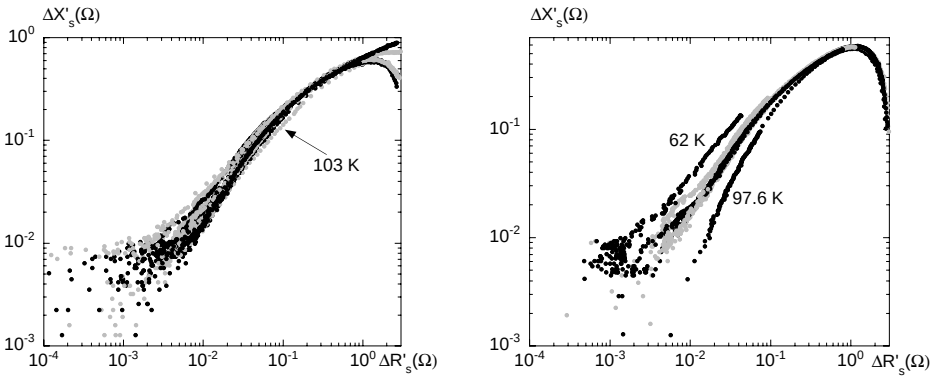

Figure 5.23: Impedance plot $\Delta X'_s$ vs $\Delta R'_s$ for sample TS5 (*left panel*, 64–102 K, 103 K) and TS2 (*right panel*, 62 K, 68–95.5 K, 97.6 K). The superimposition of the curves in the indicated temperature range is apparent. Arrow intersects the three detaching curves with increasing T as reported.

A remarkable superposition of most curves is noted in the temperature ranges 64–102 K and 68–95.5 K in TS5 and TS2, respectively. This phenomenon weakens at high H and T, presumably because of the insurgence of the Δr_2 maximum. The superposition breaks off also at low values for $\Delta R'_s$, where the initial step shows up. Since this scaling holds by varying both the field H and the temperature T, analytically one expects that $\Delta R'_s$ and $\Delta X'_s$ present the following composite functional dependence:

$$\begin{aligned} \Delta R'_s(H,T) &= \mathcal{R}(f(H,T)) \\ \Delta X'_s(H,T) &= \mathcal{X}(f(H,T)) \end{aligned} \tag{5.8.1}$$

where $\mathcal{R}(x)$ and $\mathcal{X}(x)$ are two functions depending only on the argument x, so that any T and B dependence must appear through it, and $f(H,T)$ is an unknown function of B and T. In this way, by inverting (5.8.1) one obtains $(f(H,T)) = \mathcal{R}^{-1}(\Delta R'_s)$ which, substituted in (5.8.2), yields the universal law $\Delta X'_s(\Delta R'_s) = \mathcal{X}(\mathcal{R}^{-1}(\Delta R'_s))$ independent from H and T. Physically, it is plausible to search for a functional form as follows:

$$f(H,T) = \frac{H}{h^*(T)} \tag{5.8.2}$$

where $h^*(T)$ is a temperature-dependent scale field. It has been found that such a field scale exists. In fact, it has been possible to scale all the curves that collapsed in the impedance plot simply by adjusting the field scale, $h^*(T)$. $b^*(T)$ has been determined by focusing on $\Delta R'_s(H,T)$: selecting a "master curve" (at T_{ref}=101 K and 93.6 K for TS5 and TS2, respectively), $h^*(T)$ is determined so that $\Delta R'_s(H/h^*(T),T) = \Delta R'_s(H/1,T_{ref})$ (by definition, $h^*(T_{ref}) = 1$). The result is reported in figure 5.24.

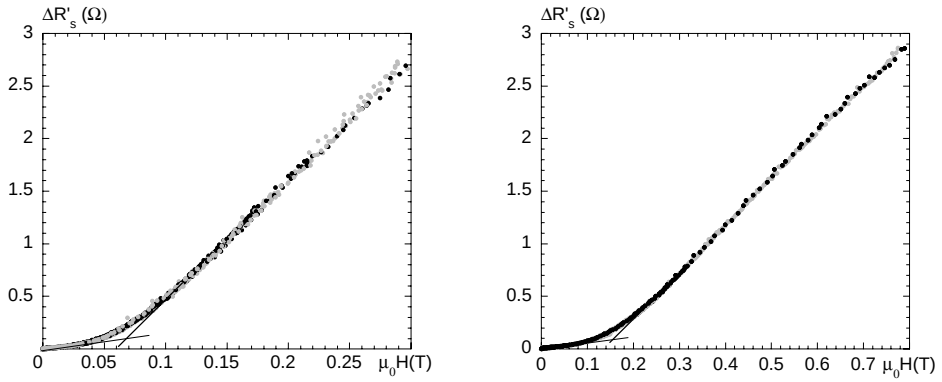

Figure 5.24: Scaled $\Delta R'_s(H/h^*(T),T)$ for various temperatures for TS5 (*left panel, 18 curves with* $64 \leq T \leq 102$) and TS2 (*right panel, 7 curves with* $68 \leq T \leq 95.5$). The crossing of the superimposed straight lines determines the absolute value of the scale field (see text).

In order to assign an absolute value to the scaling field, it should be noted that the $\Delta R'_s$ curves (this is most evident in the scaled curve) present a rather clear "knee". The absolute scaling field H^* has been determined by drawing the straight lines depicted in figure 5.24. The temperature dependence of the scaling fields is reported in left panel of figure 5.25.

The shape of the curve is analogous to the reported irreversibility and/or melting lines, so that a comparison with literature is in order. In right panel of figure 5.25 the data for H^* vs the reduced temperature t are compared to the melting line determined in TBCCO crystals from I-V scaling [184].

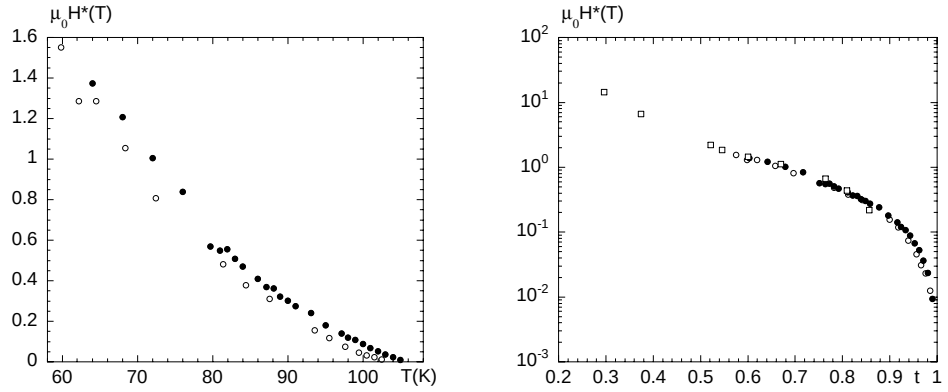

Figure 5.25: *Left panel*: scale field H^* for TS5 (full dots) and TS2 (open symbols) vs temperature. *Right panel*: same as before, vs reduced temperature t. Also reported the melting field in TBCCO crystal (with a multiplicative factor of 2.2) taken from [184] (open squares).

It is seen that the two sets of data describe the same behaviour, being present only a multiplicative factor. In reference [184] the low field data were interpreted by and quantitatively fitted to the Glazman-Koshelev [185] theory for the 3D solid-liquid melting of vortex matter. To the least, one can deduce from the scaling, from the comparison with data taken in dc and from the strongly enhanced response above H^* that the data here taken suggest a transition/crossover at the field H^* of the vortex matter. The scaling indicates that, whichever is the detailed model describing the response, in the field range here explored the vortex dynamics is ruled by the field H^*.
I lastly comment on the behaviour of $\Delta X'_s$. After having accomplished the scaling of the real part, it is readily seen in figure 5.26 that the imaginary part scales similarly (without additional parameters), although at higher fields the scaling clearly breaks down approaching the maximum.

Taking into account the experimental results and the discussion of the data regarding the RE-BCO samples, this departure might be ascribed to the increased superfluid depletion with approaching T_c: correctly, it would give a decreasing dependence on the field, and it should not necessarily scale with a vortex-matter-related scaling field H^*. In order to describe the details of this contribution, it would be necessary to identify the leading mechanism for the vortex response.

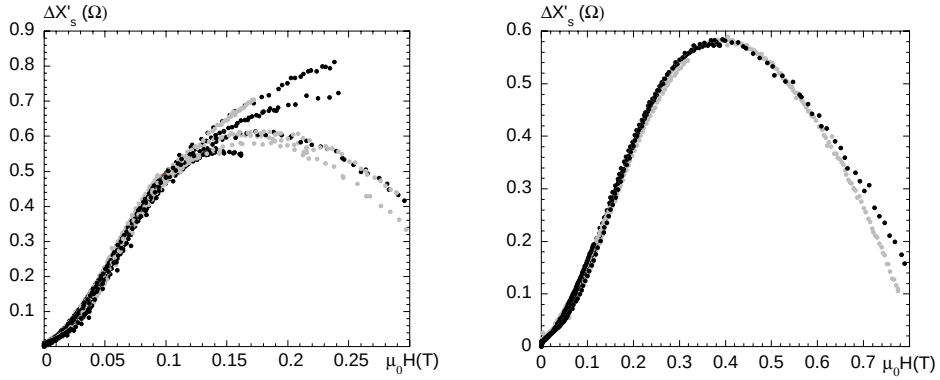

Figure 5.26: Scaled $\Delta X'_s(H/h^*(T), T)$ for various temperatures for TS5 (*left panel, 18 curves with* $64 \leq T \leq 102$) and TS2 (*right panel, 7 curves with* $68 \leq T \leq 95.5$), with H^* determined from the scaling of $\Delta R'_s$.

5.9 Concluding remarks

In this chapter data for the microwave response of several cuprate thin films have been presented. It has been shown that very simple models, albeit peculiar of the electronic state of cuprate, can describe the behaviour of RE-BCO films. In more anisotropic compounds the situation is less clear. However, while BSCCO remains elusive, TBCCO shows clear features that constitute a ground base for future work: the clear scaling behaviour indicates that the vortex dynamics is ruled by transformation of the vortex matter (or, at least, by dramatic changes in the vortex mobility), while the non-monotonous field dependence of the imaginary part suggests also in TBCCO a role for the field induced superfluid depletion close to T_c.

Chapter 6

Conclusions

In this thesis the electrical complex resistivity in the mixed state of various epitaxial films of superconducting cuprates was studied by means of microwave resonating technique.

The method of measurement of the effective surface impedance for thin films underwent a critical study. The resulting overall response of the film/substrate structure was analytically studied considering very general substrates, from metallic-like to dielectrics, including semiconducting materials. $YBa_2Cu_3O_{7-\delta}$ samples grown over ferroelectric and Silicon substrates were experimentally studied and compared to the mentioned theoretical and numerical study. This preliminary investigation allowed for a correct interpretation of the subsequent measurements of the effective surface impedance as a function of the applied field.

A new experimental setup was put in operation. A dielectric resonator operating at 47.5 GHz was designed, developed, tested and effectively used in the study of the highly anisotropic cuprate $Tl_2Ba_2CaCu_2O_{8+x}$. The comparison between the data taken through the dielectric resonator and the data obtainable by means of the pre-existing metal cavity showed an improvement in sensitivity of two orders of magnitude in both the real and imaginary components of the surface impedance. A specific detuning system for the dielectric resonator was devised in order to address calibration issues. Further possible developments are devised.

The materials investigated presented a quite wide range of features in their field-induced complex resistivity variations. It was found that a conventional analysis, based only on fluxon dynamics, could never describe the experimental findings. On the basis of the generally accepted existence of zero-energy excitations (nodes in the superconducting gap) of the superfluid energy spectrum, a model as simple as possible has been developed by extending the Coffey-Clem theory. In this way, the findings in the RE-BCO samples could be accounted

for in the temperature and field dependence. In particular, SmBCO compounds were found to be strongly influenced by pair-breaking effects induced by even moderate static applied fields. Vortex dynamics, in this case, was completely described within a free flux flow regime. YBCO presented also a relevant quasiparticle contribution, but in this particular sample vortex dynamics was influenced by pinning effects. In both cases the vortex intrinsic parameter, i.e. the vortex viscosity, was found to present the same temperature behaviour, being quantitatively the same within scale factors of the order of unity. Moreover, all the measured viscosities in RE-BCO films scaled also with data presented in literature in other YBCO films and single crystals, suggesting a common behavior for the electronic states in the vortex cores of SmBCO films, YBCO films and YBCO crystals. The quasiparticle relaxation time below T_c has been estimated of the order τ_{QP}=0.2–0.5 ps, in agreement with reported estimates in YBCO crystals and films.

In more anisotropic compounds the phenomenology was even richer, but also less clear. In particular, BSCCO presented a puzzling behaviour, escaping to conventional interpretations even in the framework of vortices together with quasiparticle contributions. However, the data taken seem to point to two separate mechanisms: one confined to lower temperatures, and another existing only near (and above) T_c. The wide transition shown by this compound hints indeed at fluctuation dominated behaviour in the higher temperature range, although the identification of the specific mechanisms deserves further study.

At last, TBCCO measurements, performed through the newly developed dielectric resonator, presented a different and richer phenomenology, essentially referable to three main mechanisms. Firstly, the very low field region, well detectable thanks to the superior sensitivity of the dielectric resonator, presents a steep rise, followed by a saturation, in the surface impedance variations with the applied field. Data indicate characteristic fields which quantitatively agree with breakdown of linear microwave response. This feature, together with the field dependence, points to a picture in terms of Josephson-junctions-like grain boundaries. Secondly, the data showed, in a wide interval of field and temperature values in our measurement range, a reactive contribution larger than the resistive one and an overall upward curvature against the applied field. Remarkably, the real resistivity presents an apparent scaling behavior with a characteristic scale field H^*. The latter was evaluated and found to be the same (within factors ~ 1) as in melting fields presented in literature. Above H^*, the microwave response steepens sharply. Thus, the data here taken in TBCCO suggest that vortex matter undergoes a transition/crossover at the field H^*, with a corresponding change of fluxon mobility. Lastly, at higher temperatures near T_c, the above mentioned scaling breaks off, particularly in the

reactive component. Indeed, the reactive part starts to decrease, reminiscent of the behaviour observed in RE-BCO, suggesting an insurgent contribution of superfluid depletion.

In conclusion, the microwave response of various cuprates in the mixed state has been extensively studied, also by developing an upgrade of the experimental setup. It is seen that by considering vortex motion only it is not possible to take into account the observed behaviour. Several peculiar aspects of HTCS, such as low-energy excitations and vortex matter transformations, appear to play major roles in the measured response.

Appendix A

Electromagnetic resonators

A.1 A few words about resonant modes

An electromagnetic resonator is a structure capable of supporting confined electromagnetic (em) fields. In the ideal condition of lossless conductors and dielectrics, the em field configurations can be determined by solving the Helmholtz equations together with the boundary conditions imposed by the structure. In the case of homogeneous and isotropic media, these equations read:

$$\nabla^2\mathbf{E} + k^2\mathbf{E} = 0$$
$$\nabla^2\mathbf{H} + k^2\mathbf{H} = 0$$

where $k = \omega\sqrt{\mu_0\varepsilon}$. Once solved, the Helmholtz equations yield a countable infinity of solutions, called *modes*, each one having its own resonant frequency ν_0. The mode with the lowest ν_0 is called *fundamental*, while modes with same ν_0 are said to be *degenerate*. Modes are usually classified considering their field components with respect to a given direction. In geometries such as those of rectangular, cylindrical and coaxial cavities and usual dielectric resonators, the relevant direction is the longitudinal axis. In these cases modes are said to be transverse electric (TE) or transverse magnetic (TM) if electric or magnetic fields are purely transverse (i.e. have zero longitudinal components), respectively. Multiply connected structures (such as coaxial cavities) can support also transverse electromagnetic (TEM) fields, without any longitudinal component. Structures with inhomogeneous medium (such as dielectric resonators) allow for hybrid electromagnetic (HEM) modes, which have all the six em field components different from zero. Various further classifications within the HEM family exist [121].

A mode is fully described by supplying its class type and the three *modal indexes*, which allow to uniquely identify it among the countable infinity of similar solutions. In cylindrical structures the modal indexes triplet *mnp* usually refers to azimuthal, radial and axial (longitudinal) directions. As an example, in figure A.1 (adapted from [186]) some modes of a cylindrical cavity are given: the fundamental TE_{111}, the azimuthal symmetrical TE_{011} and its degenerate TM_{111}, the mode TE_{012} having axial index > 1.

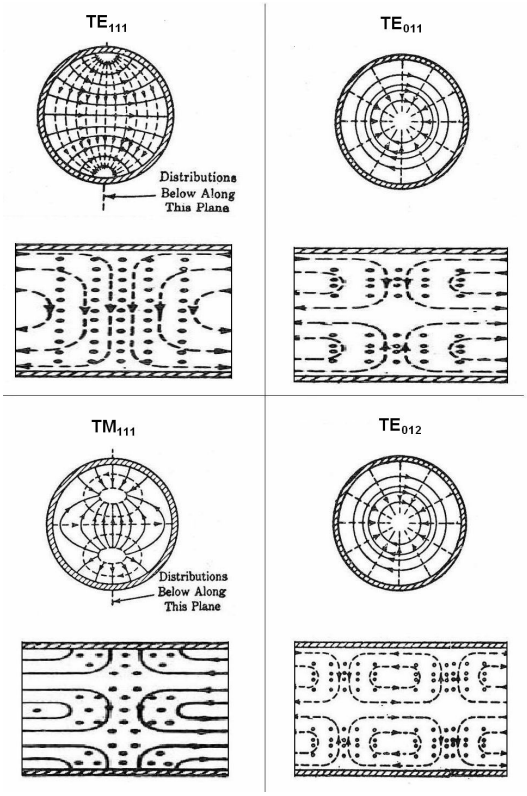

Figure A.1: Modes of a cylindrical cavity: transverse and longitudinal sections (adapted from [186]).

A.2 Resonator parameters and surface impedance

A mode in an ideal lossless resonator oscillates indefinitely having frequency ν_0. In the real condition, taking into account finite energy dissipation, the (quasi)mode is exponentially dumped with a time constant equal to $Q/(2\pi\nu_0)$,

where Q is the mode quality factor. Taking into account only internal power dissipation P, the unloaded Q_U is defined as:

$$Q_U = \frac{2\pi\nu_0 W}{P} \tag{A.2.1}$$

where W is the average electromagnetic energy stored in the resonator volume V. W is computed as the sum of the electric and magnetic energies:

$$W = W_e + W_h \tag{A.2.2}$$

$$W_e = W_{e,0} + W_{e,d} = \frac{1}{4}\int_{V_0} \varepsilon_0 |\mathbf{E}|^2 dV + \frac{1}{4}\int_{V_d} \varepsilon_0 \varepsilon_{r1} |\mathbf{E}|^2 dV \tag{A.2.3}$$

$$W_h = \frac{1}{4}\int_{V} \mu |\mathbf{H}|^2 dV \tag{A.2.4}$$

being ε_{r1} the real part of the permittivity of an isotropic[1] dielectric material filling the volume V_d and storing the electric energy $W_{e,d}$. V_0 is the empty volume that contains the electric energy $W_{e,0}$ and $V = V_0 \bigcup V_d$. For what concerns the magnetic field, the relative permeability is assumed to be $\mu_r = 1$. At resonance, by definition, it is $W_e = W_h$. The power dissipation is $P = P_\Omega + P_d$, where P_Ω is a surface contribution arising from ohmic dissipation in finite-conductivity conductors and P_d is a volume contribution arising from the polarization dissipation in lossy dielectrics[2]. These quantities can be computed within a perturbation approach: losses are assumed to be small enough to leave unperturbed the electromagnetic field distribution. In this way the surface current density $\mathbf{J}_{surf}$ can be determined from the unperturbed tangential magnetic fields $\mathbf{H}_t$ on the surfaces so that:

$$P_\Omega = \frac{1}{2} R_s \int_S |\mathbf{J}_{surf}|^2 dS = \frac{1}{2} R_s \int_S |\mathbf{H}_t|^2 dS \tag{A.2.5}$$

where R_s is the surface resistance of the (super)conductor occupying the resonator surface S. If the (super)conductor surfaces S_i, with $S = \bigcup_i S_i$, have different surface resistances $R_{s,i}$, the above integral can be decomposed as:

$$P_\Omega = \sum_i \frac{1}{2} R_{s,i} \int_{S,i} |\mathbf{H}_t|^2 dS \tag{A.2.6}$$

[1]This choice does not lose generality for the purposes of this thesis. In fact, the TE_{011} mode in uniaxially anisotropic dielectric resonator, which is the one of interest (see following section), can be treated as depicted here provided that the transverse value of ε_r is used.

[2]Radiation power losses, which characterizes leaky modes in open structures such as gapped dielectric resonators, are not considered.

Dielectric losses, on the other hand, are:

$$P_d = \frac{1}{2}\omega_0 \int_{V_d} \varepsilon_0 \varepsilon_{r2} |\mathbf{E}|^2 dV \tag{A.2.7}$$

where ε_{r2} is the imaginary part of the permittivity of the dielectric material. Using these expressions, partial quality factors can be introduced. The ohmic quality factor Q_Ω can be expressed as:

$$\frac{1}{Q_\Omega} = \sum_i \frac{R_{s,i}}{G_i} \tag{A.2.8}$$

where the geometric factor G_i of the surface S_i is defined as:

$$G_i = \frac{\omega_0 W}{\frac{1}{2}\int_{S,i} |\mathbf{H}_t|^2 dS} \tag{A.2.9}$$

The geometric factors G_i combine giving the overall $G_0^{-1} = \sum_i G_i^{-1}$.

The dielectric quality factor Q_d can be written as:

$$\frac{1}{Q_d} = \frac{W_{e,d} \tan\delta}{W_e} = \eta \tan\delta \tag{A.2.10}$$

where $\tan\delta = \varepsilon_{r2}/\varepsilon_{r1}$ is the dielectric loss tangent and $\eta = W_{e,d}/W_e \lesssim 1$ is the electric energy filling factor. The overall quality factor Q_U in (A.2.1) can be now rewritten as follows:

$$\frac{1}{Q_U} = \frac{P_\Omega + P_d}{\omega_0 W} = \frac{1}{Q_\Omega} + \frac{1}{Q_d} = \sum_i \frac{R_{s,i}}{G_i} + \eta \tan\delta \tag{A.2.11}$$

Non-idealities have also effects on the resonant frequency. Starting from the imaginary component of the resonator perturbation equation [187] and taking into account separately the different perturbation sources, the fractional variation of the resonant frequency can be written as:

$$\frac{\Delta\nu_0}{\nu_0} = -\sum_i \frac{\Delta X_{s,i}}{2G_i} - \left.\frac{\Delta\nu_0}{\nu_0}\right|_{diel} \tag{A.2.12}$$

where $\left.\frac{\Delta\nu_0}{\nu_0}\right|_{diel}$ represents the dielectric contribution

$$\left.\frac{\Delta\nu_0}{\nu_0}\right|_{diel} = \frac{1}{2}\eta\frac{\Delta\varepsilon_r}{\varepsilon_r} + \sum_k |p_{d_k}| \frac{\Delta d_k}{d_k} \tag{A.2.13}$$

In the above equations ΔA represents the variation of the quantity A with respect to its reference value A, $\Delta X_{s,i}$ is the surface reactance of the (super)conductor occupying the surface S_i, d_k are the linear dimensions of the

dielectric and p_{d_k} the corresponding dimensional filling factor. Each p_{d_k} can be computed resorting to its expression (to be derived from the resonator perturbation equation) or from the incremental rule [188] as $|p_{d_k}| = |\partial\nu_0/\partial d_k|(d_k/\nu_0)$. Equation (A.2.12) is commonly used to extract the variation of the surface reactance from the measured frequency shift.

A.3 Modal fields of the dielectric resonator

In this appendix the electromagnetic structure represented in figure A.2 (along with its cylindrical coordinate system) is studied [121, 189]. It consists of an uniaxially anisotropic cylindrical dielectric rod ($r \leq a$, region 1) surrounded by air or vacuum ($a < r \leq b$, region 2) coaxially enclosed in a metallic case.

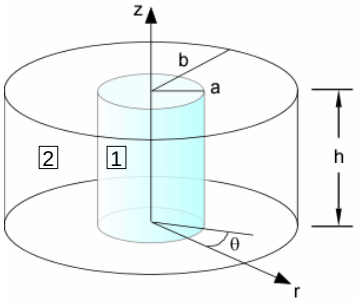

Figure A.2: Shielded dielectric resonator in cylindrical coordinate system.

The uniaxially anisotropic relative permittivity tensor is given by:

$$\bar{\bar{\varepsilon}}_r = \begin{bmatrix} \varepsilon_t & 0 & 0 \\ 0 & \varepsilon_t & 0 \\ 0 & 0 & \varepsilon_z \end{bmatrix} \tag{A.3.1}$$

and the anisotropy coefficient is defined as $\alpha = \varepsilon_z/\varepsilon_t$. The relative magnetic permeability of all the materials is assumed $\mu_r = 1$ and the conductors are assumed to be lossless. In the frequency domain, using the time-harmonic factor $e^{\mathrm{i}\omega t}$, the source-free Maxwell equations in the dielectric are:

$$\nabla \times \mathbf{E} = -\mathrm{i}\omega\mu_0\mathbf{H} \tag{A.3.2}$$
$$\nabla \times \mathbf{H} = \mathrm{i}\omega\varepsilon_0\bar{\bar{\varepsilon}}_r\mathbf{E} \tag{A.3.3}$$
$$\nabla \cdot (\bar{\bar{\varepsilon}}_r\mathbf{E}) = 0 \tag{A.3.4}$$
$$\nabla \cdot \mathbf{H} = 0 \tag{A.3.5}$$

Equation (A.3.4) can be rewritten as:

$$\nabla \cdot \mathbf{E} = \left(1 - \frac{\varepsilon_z}{\varepsilon_t}\right) \frac{\partial E_z}{\partial z} \tag{A.3.6}$$

Combining the Maxwell equations and using expression (A.3.6), one derives the following Helmholtz equations for the electric $\mathbf{E}$ and magnetic fields $\mathbf{H}$ inside the dielectric:

$$(\nabla \cdot \nabla)\mathbf{E} - \left(1 - \frac{\varepsilon_z}{\varepsilon_t}\right) \nabla \frac{\partial E_z}{\partial z} + k_0^2 \bar{\bar{\varepsilon}}_r \mathbf{E} = 0 \tag{A.3.7}$$

$$(\nabla \cdot \nabla)\mathbf{H} + \mathrm{i}\omega\varepsilon_0 \nabla \times (\bar{\bar{\varepsilon}}_r \mathbf{E}) = 0 \tag{A.3.8}$$

Since all the electromagnetic field components can be derived once the z-components E_z and H_z are known, one can focus on them looking for the scalar equations which they must satisfy. Projecting the above expressions along the z direction and using the following identity derived from the first Maxwell equation:

$$\{\nabla \times (\bar{\bar{\varepsilon}}_r \mathbf{E})\}_z = -\mathrm{i}\omega\varepsilon_0\varepsilon_t H_z \tag{A.3.9}$$

one can write down the desired scalar (and decoupled) wave equations for the z-components of $\mathbf{E}$ and $\mathbf{H}$:

$$\nabla^2 E_z - \left(1 - \frac{\varepsilon_z}{\varepsilon_t}\right) \frac{\partial_2 E_z}{\partial z^2} + \varepsilon_z k_0^2 E_z = 0 \tag{A.3.10}$$

$$\nabla^2 H_z + \varepsilon_t k_0^2 H_z = 0 \tag{A.3.11}$$

where $k_0 = \omega\sqrt{\varepsilon_0\mu_0}$ is the vacuum wave number. In the region 2 of the resonator these same equations can be used with $\bar{\bar{\varepsilon}}_r = \bar{\bar{1}}$, being $\bar{\bar{1}}$ the unity matrix. Equations (A.3.10) and (A.3.11) are solved together with the boundary conditions on the conducting walls (upper and lower plates and lateral wall), giving the following quantities (subscripts 1 and 2 denote quantities in region 1, dielectric, and region 2, air, respectively):

$$E_{z1} = A k_{e1}^2 J_m(k_{e1} r) \cos m\theta \cos \beta z \tag{A.3.12}$$

$$H_{z1} = B k_{h1}^2 J_m(k_{h1} r) \sin m\theta \sin \beta z \tag{A.3.13}$$

in region 1 with $0 \leq r \leq a$, and

$$E_{z2} = k_2^2 C P_{E,m}(k_2 r) \cos m\theta \cos \beta z \tag{A.3.14}$$

$$H_{z2} = k_2^2 D P_{H,m}(k_2 r) \sin m\theta \sin \beta z \tag{A.3.15}$$

in region 2 with $a < r \leq b$. In the above equations:

$$
\begin{aligned}
k_{e1}^2 &= \varepsilon_z k_0^2 - \frac{\varepsilon_z}{\varepsilon_t}\beta^2 = \alpha k_{h1}^2 && \text{(A.3.16)}\\
k_{h1}^2 &= \varepsilon_t k_0^2 - \beta^2 && \text{(A.3.17)}\\
k_2^2 &= \beta^2 - k_0^2 && \text{(A.3.18)}\\
\beta &= \frac{p\pi}{h} && \text{(A.3.19)}\\
k_0 &= \omega_0\sqrt{\varepsilon_0\mu_0} = \frac{2\pi\nu_0}{c} && \text{(A.3.20)}\\
P_{E,m} &= K_m(k_2 r) - \frac{K_m(k_2 b)}{I_m(k_2 b)} I_m(k_2 r) && \text{(A.3.21)}\\
P_{H,m} &= K_m(k_2 r) - \frac{K'_m(k_2 b)}{I'_m(k_2 b)} I_m(k_2 r) && \text{(A.3.22)}
\end{aligned}
$$

where the vacuum wave number k_0 is now evaluated at the resonant frequency $\nu_0 = \omega_0/(2\pi)$, and $c = 1/\sqrt{\mu_0\varepsilon_0}$ is the speed of light. A, B, C and D are mode constants determined (apart an overall scale factor defining the absolute intensity of the electromagnetic fields) by the boundary conditions at the dielectric/vacuum interface; m, n, and p are the mode numbers in the azimuthal, radial and axial directions, respectively; $J_m(x)$, $I_m(x)$ and $K_m(x)$ are the Bessel function of the first kind, modified Bessel functions of the first and second kind, respectively; the primes on the Bessel functions and on the $P_{E|H,m}(x)$ functions denote a differentiation with respect their argument x. All the remaining field components are obtained through the following:

$$
\begin{aligned}
E_r &= -\mathrm{i}\omega\mu_0 \frac{1}{k_h^2}\frac{1}{r}\frac{\partial H_z}{\partial\theta} + \frac{\varepsilon_z}{\varepsilon_t}\frac{1}{k_e^2}\frac{\partial^2 E_z}{\partial r\partial z}\\
E_\theta &= \mathrm{i}\omega\mu_0 \frac{1}{k_h^2}\frac{\partial H_z}{\partial r} + \frac{\varepsilon_z}{\varepsilon_t}\frac{1}{k_e^2}\frac{1}{r}\frac{\partial^2 E_z}{\partial\theta\partial z}\\
H_r &= \frac{1}{k_h^2}\frac{\partial^2 H_z}{\partial r\partial z} + \mathrm{i}\omega\varepsilon_0\varepsilon_z\frac{1}{k_e^2}\frac{1}{r}\frac{\partial E_z}{\partial\theta}\\
H_\theta &= \frac{1}{k_h^2}\frac{1}{r}\frac{\partial^2 H_z}{\partial\theta\partial z} - \mathrm{i}\omega\varepsilon_0\varepsilon_z\frac{1}{k_e^2}\frac{\partial E_z}{\partial r}
\end{aligned}
\qquad \text{(A.3.23)}
$$

The continuity condition for the tangential components of the fields at the dielectric/vacuum interface requires that $E_{z1} = E_{z2}$, $H_{z1} = H_{z2}$, $E_{\theta1} = E_{\theta2}$, $H_{\theta1} = H_{\theta2}$, which give an homogeneous linear system which has non-trivial solutions for A, B, C, D if its coefficient matrix determinant is non zero. This

condition is verified for the solutions, in terms of resonant frequency ν_0, of the following characteristic equation:

$$F_1 F_2 - F_3^2 = 0 \tag{A.3.24}$$

with

$$\begin{aligned} F_1 &= \varepsilon_z \frac{J_n'(x_e)}{x_e J_n(x_e)} + \frac{P_{E,n}'(y)}{y P_{E,n}(y)} \\ F_2 &= \frac{J_n'(x_h)}{x_h J_n(x_h)} + \frac{P_{H,n}'(y)}{y P_{H,n}(y)} \\ F_3 &= \frac{m\beta}{k_0}\left(\frac{1}{x_h^2} + \frac{1}{y^2}\right) \end{aligned} \tag{A.3.25}$$

where $x_e = k_{e1}a$, $x_h = k_{h1}a$ and $y = k_2 a$. In particular, the characteristic equation for TE_{0np} is $F_2 = 0$; for TM_{0np} and TM_{mn0} it is $F_1 = 0$ and for the hybrid modes HEM_{mnp} with $n \geq 1$ it is the full expression $F_1 F_2 - F_3^2 = 0$.

I now particularize for the case of the TE_{011} mode, writing down the full field expressions and the the figures of merit of the dielectric resonator used in this work. The field expressions are derived from (A.3.12), (A.3.14) and (A.3.23) giving the following:

$$\begin{aligned} H_{z1} &= H_0 J_0(k_h r)\sin\beta z \\ H_{z2} &= H_0 \frac{J_0(k_h a)}{P_{H,0}(k_2 a)} P_{H,0}(k_2 r)\sin\beta z \\ E_{\theta 1} &= -H_0 \frac{\mathrm{i}\omega\mu_0}{k_h} J_1(k_h r)\sin\beta z \\ E_{\theta 2} &= -H_0 \frac{\mathrm{i}\omega\mu_0}{k_h} \frac{J_1(k_h a)}{P_{H,0}'(k_2 a)} P_{H,0}'(k_2 r)\sin\beta z \\ H_{r1} &= -H_0 \frac{\beta}{k_h} J_0(k_h r)\cos\beta z \\ H_{r2} &= -H_0 \frac{\beta}{k_h} \frac{J_0(k_h a)}{P_{H,0}(k_2 a)} P_{H,0}(k_2 r)\cos\beta z \\ E_z &= E_r = 0,\ H_\theta = 0 \end{aligned} \tag{A.3.26}$$

where H_0 is a re-defined overall scale factor.

The amounts of electric energy stored in regions 1 and 2, which are required to compute η and therefore Q_d, are:

$$
\begin{aligned}
W_{e1} &= \frac{\varepsilon_t \varepsilon_0 \pi}{8} h a^2 |H_0|^2 \mathrm{IntJ} \\
W_{e2} &= \frac{\varepsilon_0 \pi}{8} h a^2 |H_0|^2 \mathrm{IntP} \qquad \text{(A.3.27)} \\
\mathrm{IntJ} &= J_0(x_h)^2 - \frac{2}{x_h} J_0(x_h) J_1(x_h) + J_1^2(x_h) \\
\mathrm{IntP} &= \left[\frac{J_1(x_h)}{P'_{H,0}(y)} \right]^2 \left[P^2_{H,0}(y) - \frac{2}{y} P_{H,0}(y) P'_{H,0}(y) - P'^2_{H,0}(y) - \left(y \frac{b}{a} \right)^2 P^2_{H,0} \left(y \frac{b}{a} \right) \right]
\end{aligned}
$$

The geometric factors G_{base} and G_{lat}, respectively for one base and for the lateral walls, are:

$$
G_{base} = 4\pi Z_0 \left(\frac{\nu_0 h}{c} \right)^3 \frac{\varepsilon_t \mathrm{IntJ} + \mathrm{IntP}}{\mathrm{IntJ} + \mathrm{IntP}} \qquad \text{(A.3.28)}
$$

$$
G_{lat} = 4\pi^3 Z_0 \left(\frac{\nu_0}{c} \right)^3 \frac{a^4}{b} \frac{1}{y^2} \frac{\varepsilon_t \mathrm{IntJ} + \mathrm{IntP}}{\left(\frac{J_1(x_h)}{P'_{H,0}(y)} \right)^2 P^2_{H,0}(yb/a)} \qquad \text{(A.3.29)}
$$

with $Z_0 = \sqrt{\mu_0/\varepsilon_0}$ being the vacuum characteristic impedance. Last, the overall geometric factor is computed as $G_0^{-1} = 2G_{base}^{-1} + G_{lat}^{-1}$.

Appendix B

Details on interpretation of YBCO/Si surface impedance data

In this appendix I report the full procedure used to invert relation (4.1.1) and to extract the bulk Z_s from the measured Z'_s of the YBCO/Si film described in section 4.3. Firstly, the small film thickness allows us to simplify equation (4.1.1) by Taylor expanding to first order the $\tan(k_s t_s)$ term:

$$Z'_s = Z_s^{(\mathrm{f})} \frac{Z'_d + \mathrm{i}\omega\mu_0 t_s}{Z_s^{(\mathrm{f})} + Z'_d} \tag{B.1.1}$$

Secondly, one defines the reference temperatures delimiting the temperature ranges considered: T_{min} is 52K and 70K for 24 and 48 GHz respectively, and T_{max}=97 K and T_{max}=91 K for 24 and 48 GHz respectively. Effective substrate surface resistance values R'_d are separately measured in the temperature range of interest around T_c, yielding almost constant values of 9.4 Ω and 32 Ω for 24 and 48 GHz respectively. In particular, R'_d at 24 GHz measured over a wide temperature range is reported in figure B.1. It can be seen that its behavior resembles more closely the finite thickness effective R'_d (lower panel of figure 4.7) than a bulk substrate R_d.

I now illustrate the procedure used: I initially focus the attention to the data taken at 48 GHz. First of all, one needs to know the values of the whole impedances involved which, in particular, require the knowledge of the corresponding (absolute) reactances X'_s and X'_d. One then evaluates their values above T_c. At the reference temperature $T_{max,48} > T_c$, the real and imaginary parts of equation (B.1.1) contain the two unknown reactances $X'_s(T_{max,48})$ and $X'_d(T_{max,48})$. R'_s and R'_d are measured and $R_s^{(\mathrm{f})} = \rho_{dc}/t_s$ (see equation

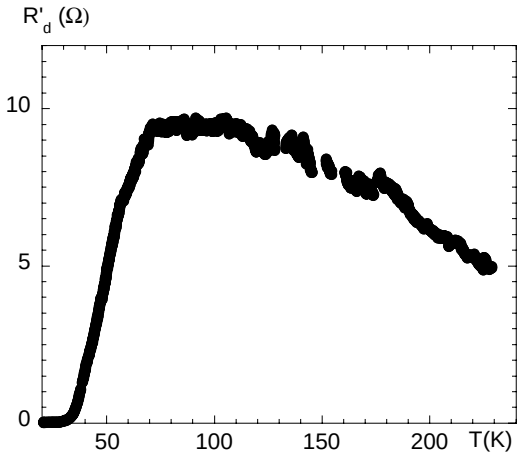

Figure B.1: Effective surface resistance R'_d of Silicon substrate only at 24 GHz.

(4.1.3): small imaginary parts due to superconducting fluctuations [174] are neglected). Solving this algebraic problem, one obtains $X'_s(T_{max,48}) = 29\,\Omega$ and $X'_d(T_{max,48}) = 83\,\Omega$. The absolute value of $X'_s(T)$ for all temperatures is then computed from the measured $\Delta X'_s(T)$, so that the whole $Z'_s(T)$ is now known. As far as Z'_d is concerned, one takes a constant $Z'_d(T) = (32 + \mathrm{i}83)\,\Omega$ in the 70-91 K range. By using the so-obtained $Z'_d(T)$ and $Z'_s(T)$ one inverts equation (4.1.1) and extract the bulk surface impedance $Z_s(T)$ of the superconductor: the result is reported in left panel of figure 4.9. The same computation can be performed for the 24 GHz measurements at $T_{max,24}$, obtaining $X'_s(T_{max,24}) = 21\,\Omega$, $X'_d(T_{max,24}) = 27\,\Omega$ and the reconstructed bulk surface impedance as reported in right panel of figure 4.9.

Appendix C

Abrikosov-Josephson Vortices

In the following, a brief summary on Abrikosov-Josephson vortices [181] will be given. Since they have intermediate properties between an Abrikosov vortex (already described in chapter 2) and a Josephson vortex, some notions about the latter will be also recalled.

It is well known that a Josephson junction (i.e. a weak link between two superconducting electrodes, made either by an insulating layer, by a normal layer or by a constriction) can sustain Josephson currents according to the Josephson equations [6], which relate the order parameter phase difference between the electrodes to the current and voltage across the junction. The following geometry is now considered: a junction consisting of two semi-infinite superconductors divided by a planar weak link of thickness d occupying the yz plane, in the presence of a magnetic field applied in the z direction (see left panel of figure C.1).

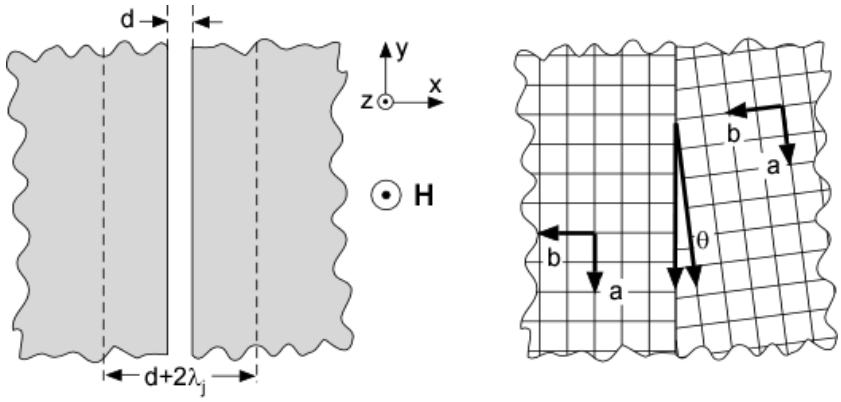

Figure C.1: Schematic diagrams of a Josephson junction (*left panel*) and of a grain boundary (*right panel*).

In this case, the phase difference between the superconductors varies period-

ically along the y direction. Each period of this variation is associated with a flux quantum which identifies a so-called Josephson fluxon. The core of a Josephson (hereafter J) fluxon, differently from an Abrikosov (hereafter A) fluxon, is not linked to variations of the modulus of the order parameter $|\psi|$, but only to a 2π variation of the phase of ψ. The phase and field profiles along the junction can be determined by solving the (local) sine-Gordon equation [6]. Both quantities vary along the junction on the same length scale $\lambda_j = \sqrt{\Phi_0/[2\pi(2\lambda + d)\mu_0 J_{cj}]}$ [6], where J_{cj} is the critical current density of the junction. In particular, the field distribution is [183]:

$$B(x,y) = \frac{\Phi_0}{2\pi\lambda\lambda_j} \frac{e^{-|x|/\lambda_j}}{\cosh(y/\lambda_j)} \tag{C.1.1}$$

The corresponding current distribution is depicted in left panel of figure C.2 (taken from [183]).

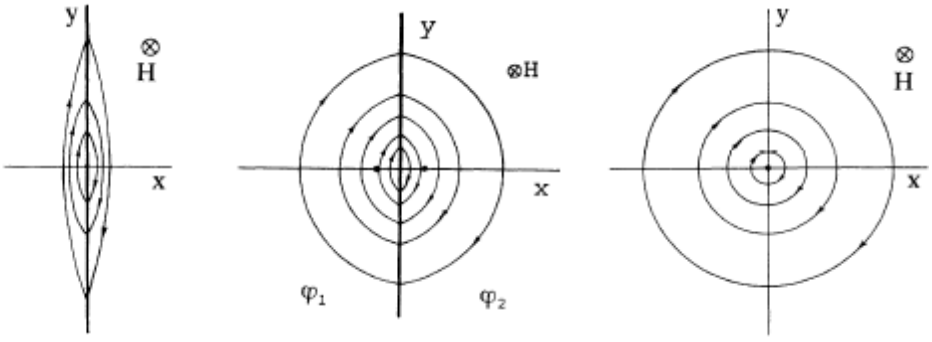

Figure C.2: Current distributions in J, AJ, and A fluxons in *left, center* and *right panels* respectively (taken from [183]).

Abrikosov-Josephson fluxons can appear along HTCS grain boundaries. Typically, grain boundaries in HTCS exhibit a weak link behaviour as soon as the grain boundary angle θ (see right panel of figure C.1) becomes greater than a given typical angle $\theta_0 \approx 5^o$ [181]. For $\theta < \theta_0$, magnetic flux penetrates the grain boundary in form of A fluxons, which usually experiment pinning strength weaker than fluxons in the grains. For $\theta > \theta_0$, the grain boundary critical current density J_{gb} sustaining the fluxons drops below the depairing current density of the bulk of the grains $J_d = \Phi_0/(3\sqrt{3}\pi\mu_0\lambda^2\xi)$ and the normal core of A fluxons disappears [190], being substituted by a Josephson phase core of length along the boundary $l = \lambda_j^2/\lambda \simeq \xi J_{gb}/J_d > \xi$. For currents $J_{gb} < J_d/\kappa$, $l > \lambda$ and the vortex is a full J vortex. In the intermediate range of currents $J_d > J_{gb} > J_d/\kappa$, $l < \lambda$ and the vortex has mixed Abrikosov-Josephson (hereafter AJ) properties. More precisely, the Josephson phase core

is accompanied by a field distribution which, determined within the non-local Josephson electrodynamics equations ([181, 183] and references therein), is given by [183]:

$$B(x,y) = \frac{\Phi_0}{2\pi\lambda^2} K_0 \left[\frac{\sqrt{(l+|x|)^2+y^2}}{\lambda} \right] \tag{C.1.2}$$

As it can be seen, the field distribution is similar to that of A fluxons (see equation (2.1.1)), having space variations on the scale λ. The current distribution of AJ fluxons is reported in the center panel of figure C.2, together with that of a A fluxon in the right panel (taken from [183]). In particular, the AJ fluxon current distribution can be thought as the superposition of two specular A fluxon distributions put at distance l from the grain boundary plane (dots in figure C.2).

Summarizing, the AJ fluxons have the core structure of J fluxons and the magnetic structure of A fluxons.

As far as the fluxon dynamics is concerned, AJ fluxons are characterized by two length scales: the longitudinal core size l and the intervortex spacing a [181]. The large size of AJ core, being usually $l \gg \xi$, together with the absence of the normal region, makes pinning forces acting on AJ fluxons weaker than those acting on A fluxons. Pinning forces are mainly of magnetic origin as those arising from the interaction with the A fluxons present in the bulk of grains. The second relevant length, the intervortex spacing a, has the same field dependence as that of A fluxons, given the common field distribution shared by both types: $a = \sqrt{\Phi_0/B}$ (for $H \gg H_{c1}$). This quantity concurs in defining the one-dimensional distribution of fluxons along the grain boundary. In overall, it can be shown [181, 182] that AJ fluxon motion gives a low frequency resistance as the following:

$$R_f = \frac{R\sqrt{B}}{\sqrt{B+B_0}} \tag{C.1.3}$$

where $B_0 = (J_{gb}/J_d)^2 B_{c2} \ll B_{c2}$ and R is the grain boundary QP resistance. The resulting $R_f(B)$ curve has a downward curvature which saturates above B_0, where the AJ fluxons cores overlap. The AJ fluxon dynamics at finite frequencies present a similar behaviour [181]:

$$Z_{AJ} = \frac{R_f + R\mathrm{i}\omega\tau_f}{1+\mathrm{i}\omega\tau_f} \tag{C.1.4}$$

where $\tau_f = \tau/\sqrt{1+B/B_0}$, being τ the grain boundary QP scattering time. In conclusion, it can be noted that the AJ fluxon response differs substantially

from the A fluxon response, the latter being essentially linear in B (as shown in chapter 2) and showing saturation only at B_{c2}.

Bibliography

[1] "My Credo" - Berlin 1932, from Michael W and Gribbin J 1994 *Einstein: A Life in Science*, Penguin Books

[2] Kamerling Onnes H 1911 *Leiden Comm.* **120b, 122b, 124c**

[3] Meissner W and Ochsenfeld W 1933 *Naturwissenschaften* **21** 787

[4] Landau L D, Lifsits M, Pitaevskij L P 1977 *Fisica Statistica*, Editori Riuniti (in italian)

[5] Ginzburg V L and Landau L D 1950 *Zh. Eksperim. i Teor. Fiz.* **20** 1064

[6] Tinkham M 1996 *Introduction to Superconductivity, (2nd Edition)*, McGraw-Hill

[7] de Gennes P G 1965 *Superconductivity of Metals and Alloys*, Addison Wesley Publishing Company, Inc.

[8] Poole C P Jr, Farach H A, Creswick R J 1995 *Superconductivity*, Academic Press Inc.

[9] Gor'kov L P 1959 *Zh. Eksp. Teor. Fiz.* **36** 1918 [1959 *Phys. JEPT* **9** 1364]

[10] London F and London H 1935 *Proc. R. Soc.* **A149** 71

[11] Gorter C J and Casimir H B G 1934 *Phys. Z.* **35** 963; 1934 *Physica* **1** 306

[12] Bonn D A, Liang R, Riseman T M, Baar D J, Morgan D C, Zhang K, Dosanjh P, Duty T L, MacFarlane A, Morris G D, Brewer J H, Hardy W N, Kallin C and Berlinsky A J 1993 *Phys. Rev. B* **47** 11314

[13] Bardeen J, Cooper L N and Schrieffer J R 1957 *Phys. Rev.* **108** 1175

[14] Cooper L N 1956 *Phys. Rev.* **104** 1189

[15] Fröhlich H 1950 *Phys. Rev.* **79** 845

[16] Maxwell E 1950 *Phys. Rev.* **78** 477; Reynolds C A, Serin B, Wright W H and Nesbitt L B 1950 *Phys. Rev.* **78** 487

[17] Mattis D C and Bardeen J 1958 *Phys. Rev.* **111** 412

[18] Waldram J R, Theopistou P, Porch A and Cheah H M 1997 *Phys. Rev. B* **55** 3222

[19] Bednorz G and Müller K A 1986 *Z. Phys.***B64**189

[20] Wu M K, Ashburn J L, Torng C J, Hor P H, Meng R L, Gao L, Huang Z J, Wang Y Q and Chu C W 1987 *Phys. Rev. Lett.* **58** 908; Hikami S, Hirai T, Kagoshima S 1987 *Jpn. J. Appl. Phys.* **26** L314; Zhao Z X, Chen L, Cui C, Huang Y, Liu Z, Chen G, Li S, Guo S and He Y 1987 *Kexue Tongbao* **33** 661

[21] Orenstein J and Millis A J 2000 *Science* **288** 468

[22] Coleman P 2003 *Ann. Henri Poincaré* 2003 **4** 1 (also in *cond-mat/* 0307004)

[23] Timusk T and Statt B 1999 *Rep. Prog. Phys.* **62** 61

[24] Won H, Haas S, Parker D, Telang S, Ványolos A and Maki K 2005 *cond-mat/* 0501463

[25] Kivelson S A and Fradkin E 2005 *cond-mat/* 0507459

[26] Norman M R and Pépin C 2003 *Rep. Prog. Phys.* **66** 1547

[27] Carlson E W, Emery V J, Kivelson S A and Orgad D *Concepts in high temperature superconductivity* in *The Physics of Superconductors, Vol. II: Superconductivity in Nanostructures, High-T_c and Novel Superconductors, Organic Superconductors*; Editors: Bennemann K H and Ketterson J B; Springer, Berlin, 2004; preprint *cond-mat/* 0206217

[28] Hirchfeld P J, Putikka W O and Scalapino D J 1993 *Phys. Rev. Lett.* **22** 3705; 1994 *Phys. Rev. B* **50** 10250

[29] Hosseini A, Harris R, Kamal S, Dosanjh P, Preston J, Liang Ruixing, Hardy W N and Bonn D A 1999 *Phys. Rev. B* **60** 1349

[30] Zhang Y, Ong N P, Anderson P W, Bonn D A, Liang R and Hardy W N 2000 *Phys. Rev. Lett.* **86** 890; Chiao M, Hill R W, Lupien C, Popic B, Gagnon R and Taillefer L 1999 *Phys. Rev. Lett.* **82** 2943

[31] Dahm T, Hirschfeld P J, Scalapino D J and Zhu L 2005 *cond-mat/* 0507723

[32] Hagen S J, Jing T W, Wang Z Z, Horvath J, Ong N P 1988 *Phys. Rev. B* **37** 7928

[33] Hardy W N, Bonn D A , Morgan D C, Liang R and Zhang K 1993 *Phys. Rev. Lett.* **70** 3999

[34] Wahl A, Maignan A, Martin A, Hardy V, Provost J and Simon Ch 1995 *Phys. Rev. B* **51** 9123; Cohen L F, Cowie A, Gallop J C, Gosh I S and Goncharov I N 1997 *J. Supercond.* **10** 85; Ramirez A P, Rosseinsky M J, Murphy D W and Haddon R C 1992 *Phys. Rev. Lett.* **69** 1687

[35] Schneidewind H, Manzel M, Bruchlos G and Kirsch K 2001 *Supercond. Sci. Technol.* **14** 200

[36] Van Harlingen D J 1995 *Rev. Mod. Phys.* **67** 515

[37] Damascelli A, Hussain Z, Shen Zhi-Xun 2003 *Rev. Mod. Phys.* **75** 473

[38] Tsuei C C and Kirtley J R 2000 *Rev. Mod. Phys.* **72** 969

[39] Mathai A, Gim Y, Black R C, Amar A and Wellstood F C 1995 *Phys. Rev. Lett.* **74** 4523; Kouznetsov K A, Sun A G, Chen B, Katz A S, Bahcall S R, Clarke J, Dynes R C, Gajewski D A, Han S H, Maple M B, Giapintzakis J, Kim J -T and Ginsberg D M 1997 *Phys. Rev. Lett.* **79** 3050; Tsuei C C, Kirtley J R, Hammerl G, Mannhart J, Raffy H, Li Z Z 1999 *Nature* **387** 481

[40] Zhao Guo-meng 2001 *Phys. Rev. B* **64** 024503; Brandow B H 2002 *Phys. Rev. B* **65** 054503

[41] Li Q, Tasy Y N, Suenaga M, Klemm R A, Gu G D and Koshizuka N 1999 *Phys. Rev. Lett.* **83** 4160

[42] Klemm R A 2003 *J. Supercond.* **16** 529

[43] Nuss M C, Mankiewich P M, O'Malley M L and Westerwick E H 1991 *Phys. Rev. Lett.* **66** 3305

[44] Bonn D A, Kamal S, Zhang K, Liang R, Baar D J, Klein E and Hardy W N 1994 *Phys. Rev. B* **50** 4051

[45] Bulut N and Scalapino D J 1992 *Phys. Rev. Lett.* **68** 706

[46] Hebel L C and Slichter C P 1957 *Phys. Rev.* **107** 901; 1959 *Phys. Rev.* **113** 1504; Hebel L C 1959 *Phys. Rev.* **116** 79

[47] Hensen S, Müller G, Rieck C T and Scharnberg K 1997 *Phys. Rev. B* **56** 6237

[48] Annett J, Goldenfeld N and Renn S R 1991 *Phys. Rev. B* **43** 2778

[49] Hirschfeld P J and Goldenfeld N 1993 *Phys. Rev. B* **48** 4219

[50] Jacobs T, Shridar S, Rieck C T, Scharnberg K, Wolf T and Halbritter 1995 *J. Phys. Chem. Solids* **56** 1945

[51] Hettler M H and Hirchfeld P J 2000 *Phys. Rev. B* **61** 11313

[52] Abrikosov A A 1957 *Zh. Eksperim. i. Teor. Fiz.* **32** 1442 [1957 *Soviet Phys.–JETP* **5** 1174]

[53] Gilardi R, Mesot J, Drew A, Divakar U, Lee S L, Forgan E M, Zaharko O, Conder K, Aswal V K, Dewhurst C D, Cubitt R, Momono N and Oda M 2002 *Phys. Rev. Lett.* **88** 217003

[54] Traüble H and Essmann U 1968 *Phys. Status Solidi* **25** 395

[55] Aegerter C M, Keller H, Lloyd S H, Kealey P G, Forgan E M, Johnson S T, Riseman T M, Cubitt R, Lee S L, Ager C, Paul D McKm, Savić I M Yethiraj M, Tajima S and Rykov A 2003 *cond-mat/* 0305593

[56] Blatter G, Feigel'man M V, Geshkenbein V B, Larkin A I and Vinokur V M 1994 *Rev. Mod. Phys.* **66** 1125

[57] Brandt E H 1995 *Rep. Prog. Phys.* **58** 1465

[58] Gammel P 2001 *Nature* **411** 434

[59] Crabtree G W and Nelson D R 1997 *Phys. Today* 38

[60] Fisher D S, Fisher M P A and Huse D A 1991 *Phys. Rev. B* **43** 130

[61] Nelson D R 1988 *Phys. Rev. Lett.* **60** 1973

[62] Anderson P W 1966 *Rev. Mod. Phys.* **38** 298

[63] Kopnin N B 2002 *Rep. Prog. Phys.* **65** 1678

[64] Golosovsky M, Tsindlekht and Davidov D 1996 *Supercond. Sci. Technol.* **9** 1

[65] Tsuchiya Y, Iwaya K, Kinoshita K, Hanaguri T, Kitano H, Maeda A, Shibata K, Nishizaki T and Kobayashi N 2001 *Phys. Rev. B* **63** 184517

[66] Drew H D 1995 *Phys. Rev. B* **52** 9178; Koulakov A A and Larkin A I 1999 *Phys. Rev. B* **59** 12021; Koulakov A A and Larkin A I 1999 *Phys. Rev. B* **60** 14597; Kopnin N B and Vinokur V M 2001 *Phys. Rev. Lett.* **87** 017003

[67] Bardeen J and Stephen M J 1965 *Phys. Rev.* **140** A1197

[68] Caroli C, de Gennes P G and Matricon J 1964 *Phys. Lett.* **9** 307

[69] Kopnin N B and Volovik G E 1997 *Phys. Rev. Lett.* **79** 1377

[70] Kopnin N B 1998 *Phys. Rev. Lett.* **57** 11775

[71] Wördenweber R 1999 *Rep. Prog. Phys.* **62** 187

[72] Anderson P W and Kim Y B 1964 *Rev. Mod. Phys.* **36** 39

[73] Yeh N C 1991 *Phys. Rev. B* **43** 523

[74] Wu D H, Booth J C and Anlage S M 1995 *Phys. Rev. Lett.* **75** 525

[75] Suhl H 1965 *Phys. Rev. Lett.* **14** 226

[76] Matsuda Y, Ong N P, Yang Y F, Harris J M and Peterson J B 1994 *Phys. Rev. B* **49** 4380

[77] Kopnin N B and Vinokur V M 1998 *Phys. Rev. Lett.* **81** 3952

[78] Sonin E B *Phys. Rev. B* 2001 **63** 054527

[79] Han J H, Kim J S, Kim M J and Ao P 2005 *Phys. Rev. B* **71** 125108

[80] Tomasch W J, Blackstead H A, Ruggiero S T, McGinn P J, Clem J R, Shen K, Weber W and Boyne D 1988 *Phys. Rev. B* **37** 9864

[81] Gittleman J I and Rosenblum B 1996 *Phys. Rev. Lett.* **16** 734

[82] Volovik G E 1993 *JETP Lett.* **58** 469

[83] Won and Maki *Phys. Rev. B* 1996 **53** 5927

[84] Chiao M, Hill R W, Lupien C, Taillefer L, Lambert P, Gagnon R and Fournier P 2000 *Phys. Rev. B* **62** 3554; Sharapov S G, Gusynin V P and Beck H 2002 *Phys. Rev. B* **66** 012515; Dahm T, Graser S, Iniotakis C and Schopol N 2002 *Phys. Rev. B* **66** 144515; Nakai N, Miranovic P, Ichioka M and Machida K 2004 *Phys. Rev. B* **70** 100503; Laiho R, Lähderanta E, Safonchik M and Traito K B 2004 *Phys. Rev. B* **69** 094508

[85] Jackson J D 1962 *Classical Electrodynamics*, Wiley

[86] Portis A M, Blazey KW, Muller K A and Bednorz J G *Europhys. Lett.* 1988 **5** 467

[87] Sonin E B, Tagantsev A K *Zh. Eksp. Teor. Fiz.* 1989 **95** 994; [*Sov. Phys.-JETP* 1989, **68** 572]

[88] Marcon R, Fastampa R, Giura M and Silva E 1991 *Phys. Rev. B* **43** 2940

[89] Coffey M W and Clem J R 1991 *Phys. Rev. Lett.* **67** 386

[90] Brandt E H 1991 *Phys. Rev. Lett.* 1991 **67** 2219

[91] Sonin E B, Tagantsev A K and Traito K B 1992 *Phys. Rev. B* **46** R5830

[92] Plaçais B, Mathieu P, Simon Y, Sonin E B, Traito K B 1996 *Phys. Rev. B* **54** 13083

[93] Ong N P and Wu H 1997 *Phys. Rev. B* **56** 458

[94] Coffey M W and Clem J R 1992 *Phys. Rev. B* **45** 10527

[95] Coffey M W and Clem J R 1992 *Phys. Rev. B* **46** 11757

[96] Coffey M W and Clem J R 1993 *Phys. Rev. B* **48** 342

[97] Collin R E 1992 *Foundation for Microwave Engineering*, McGraw-Hill International Editions

[98] Maeda A, Kitano H and Inoue R 2005 *J. Phys.: Condens. Matter* **17** R143

[99] Kenneth L and Mazierska J 2002 *IEEE Trans. Microwave Theory Tech.* **50** 2115

[100] Ho W, Hood P J, Hall W F, Kobrin P, Harker A B and DeWames R E 1988 *Phys. Rev. B* **38** 7029

[101] Nichols C S, Shiren N S, Laibowitz R B and Kazyaka T G 1988 *Phys. Rev. B* **38** 11970; Golosovsky M, Davidov D, Rettori C and Stern A 1989 *Phys. Rev. B* **40** 9299; Miranda F A, Gordon W L, Bhasin K B, Heinen V O, Warner J D 1991 *J. Appl. Phys.* **70** 5450; Moser E K, Tomasch W J, McClorey M J, Furdyna J K, Coffey M W, Pettiette-Hall C L and Schwarzbeck S M 1993 *Phys. Rev. B* **49** 4199

[102] Booth J, Wu D H and Anlage SM 1996 *Rev. Sci. Instrum.* **65** 2082

[103] Peligrad D -N, Mehring M, Dulčić A 2004 *Phys. Rev. B* **69** 144516

[104] Silva E, Giura M, Marcon R, Fastampa R, Balestrino G, Marinelli M and Milani E 1992 *Phys. Rev. B* **45** 12566; Marcon R, Silva E, Fastampa R, Giura M and Sarti S 1994 *Phys. Rev. B* **50** 13684

[105] Hong S, Kim J, Park W and Lee K 2002 *Appl. Phys. Lett.* **80** 524

[106] Klein N, Chaloupka H, Müller G, Orbach S, Piel H, Roas B, Schultz L, Klein U and Peiniger M 1990 *J. Appl. Phys.* **67** 6940; Hein A M, Strupp M, Piel H, Portis A M and Gross R 1994 *J. Appl. Phys.* **75** 4581

[107] Shridar S 1988 *J. Appl. Phys.* **63** 159

[108] Donovan S, Klein O, Dressel M, Holczer and Grüner G 1993 *Int. J. Infrared Millim. Waves* **14** 2459; Dressel M, Klein O, Donovan S and Grüner G 1993 *Int. J. Infrared Millim. Waves* **14** 2489

[109] Silva E, Lezzerini A, Lanucara M, Sarti S and Marcon R 1998 *Meas. Sci. Technol.* **9** 275

[110] Srikanth H, Zhai Z, Sridhar S and Erb A 1998 *J. Phys. Chem. Solids* **59** 2105

[111] Klein O, Donovan S, Dressel M and Grüner G *Int. J. Infrared Millim. Waves* 1993 **14** 2423

[112] Donovan S, Klein O, Dressel M, Holczer K and Grüner G *Int. J. Infrared Millim. Waves* 1993 **14** 2450;

[113] Peligrad D N, Nebendahl B, Kessler C, Mehring M, Dulčić A, Požek M and Paar D 1998 *Phys. Rev. B* **58** 11652

[114] Trunin M R 1998 *J. Supercond.* **11** 381

[115] Sridhar S and Kenneth W L 1988 *Rev. Sci. Instrum.* **59** 531; Rubin D L, Green K, Gruschus J, Kirchgessner J, Moffat D, Padamsee H, Sears J and Shu Q S 1988 *Phys. Rev. B* **38** 6538

[116] Hakki B W and Coleman P D 1960 *IEEE Trans. Microwave Theory Tech.* **8** 402

[117] Cohn B *IEEE Trans. Microwave Theory Tech.* **16** 218; Courtney W E 1970 *IEEE Trans. Microwave Theory Tech.* **18** 476

[118] Krupka J, Derzakowski K, Tobar M, Hartnett J and Geyger R G 1999 *Meas. Sci. Technol.* **10** 387

[119] Tobar M E, Krupka J, Ivanov E N and Woode R A 1997 *J. Appl. Phys.* **83** 1604

[120] Kajfez D 1984 *IEEE Trans. Microwave Theory Tech.* **MIT-32** 941

[121] Kajfez D and Guillon P, Editors *Dielectric Resonators* 1986, Artech House, Inc.

[122] Shen Z -Y, Wilker C H, Pang Ph, Holstein W L, Face D and Kountz D J 1992 *IEEE Trans. Microwave Theory Tech.* **40** 2424

[123] Krupka J, Klinger M, Kuhn M, Baranyak A, Stiller M, Hinken J and Modelski J 1993 *IEEE Trans. Microwave Appl. Supercond.* **3** 3043; Tellmann N, Klein N, Dähne U, Scholen A, Schulz H and Chaloupka H 1994 *IEEE Trans. Microwave Appl. Supercond.* **4** 143; Lee S Y, Soh B J, Ahn J W, Cho J Y, Park B H, Jung C S, Fedorov V B, Denisov A G, Kim Y H, Hahn T S, Choi S S, Oh B and Moon S H 1997 *IEEE Trans. Microwave Appl. Supercond.* **7** 2013; Parker N J, Kharel A P, Powell J R, Smith P A, Evans P D and Porch A 1999 *IEEE Trans. Microwave Appl. Supercond.* **9** 1928; Klein N, Zuccaro C, Dähne U, Schulz H, Tellmann N, Kutzner R, Zaitsev A G and Wördenweber R 1995 *J. Appl. Phys.* **78** 6683; Hashimoto T and Kobayashi Y 2003 *IEICE Trans. Electron.* **E86-C** 30; Lee S Y and Oh B 2003 *J. Supercond.* **16** 823

[124] Kobayashi Y, Imai T and Kayano H 1990 *IEEE MTT-S Digest* **I-4** 281; Klein N, Jin B B, Wördenweber R, Lahl P, Kang W N, Kim H -J, Choi E -M, Lee S -I, Dahm T and Maki K 2003 *IEEE Trans. Microwave Appl. Supercond.* **13** 3253; Kobayashi Y and Yoshikawa H 1998 *IEEE Trans. Microwave Theory Tech.* **46** 2524; Jin B B, Klein N, Kang W N, Kim H -J, Choi E -M, Lee S -I, Dahm T, Maki K 2002 *Phys. Rev. B* **66** 104521; Chen L J and Lue J T 1998 *IEEE Trans. Microwave Theory Tech.* **46** 1251; Andreone A, Cassinese A, Gianni L, Iavarone M, Palomba F and Vaglio R 2001 *Phys. Rev. B* **64** 100505(R); Lee J H, Yang W I, Kim M J, Booth J C, Loeng K, Schima S, Rudman D and Lee S Y 2004 **5MJ09** 1

[125] Wilker C, Zhi-Yuan S, Pang P, Face D W, Holstein W L, Matthews A L and Laubacher D B 1991 *IEEE Trans. Microwave Theory Tech.* **39** 1462

[126] Oates D E, Anderson A C and Mankiewich P M 1990 *J. Supercond.* **3** 251

[127] Porch A, Lancaster M J and Humphreys R G 1995 *IEEE Trans. Microwave Theory Tech.* **43** 306

[128] Ghigo G, Botta D, Chiodoni A, Gerbaldo R, Gozzelino L, Laviano F, Minetti B, Mezzetti E and Andreone D 2004 *Supercond. Sci. Technol.* **17** 977

[129] Lahl P and Wördenweber R 2002 *Appl. Phys. Lett.* **81** 505

[130] Barra M, Cassinese A and Vaglio R 2005 *Supercond. Sci. Technol.* **18** 271

[131] Corbino O M 1911 *Nuovo Cimento* **1** 397

[132] Tosoratti N, Fastampa R, Giura M, Lenzi V, Sarti S, Silva E 2000 *Int. J. Mod. Phys. B* **14** 2926

[133] Kitano H, Ohashi T, Ryuzaki H, Maeda A and Tsukada I *Physica C* **412-414** 130

[134] Sarti S, Amabile C and Silva E 2004 *cond-mat/* 0406313

[135] Ceremuga-Mazierska J 1991 *Supercond. Sci. Technol.* **5** 391

[136] Biondi M A and Garfunkel M P 1959 *Phys. Rev.* **116** 853

[137] Turner P J, Broun D M, Kamal S, Hayden M E, Bobowski J S, Harris R, Morga D C, Preston J S, Bonn D A and Hardy W N 2004 *Rev. Sci. Instrum.* **75** 124

[138] Kusko C, Zhai Z, Hakim N, Markiewicz R S, Sridhar S, Colson D, Viallet-Guillen V, Forget A, Nefyodov Yu A, Trunin M R, Kolesnikov N N, Maignan A, Daignere A, Erb A 2002 *Phys. Rev. B* **65** 132501

[139] Peligrad D -N, Nebendahl B, Mehring M, Dulčić *Phys. Rev. B* **64** 224505

[140] Silva E, Lezzerini A, Lanucara M, Sarti S and Marcon R 1998 *Meas. Sci. Technol.* **9** 275

[141] Ceremuga J, Krupka J, Kosciuk T 1995 *J. Supercond.* **8** 681

[142] Mazierska J 1997 *J. Supercond.* **10** 73

[143] Fastampa R, Giura M, Marcon R and Silva E *Meas. Sci. Technol.* **1** 1172

[144] Mazierska J and Wilker C 2001 *IEEE Trans. Microwave Appl. Supercond.* **11** 3127; Mazierska J 1997 *Asian Pacific Microwave Conference* **2P01-7** 125; Krupka J and Mazierska J 1998 *IEEE Trans. Microwave Appl. Supercond.* **8** 164

[145] Kobayashi Y and Tanaka S 1980 *IEEE Trans. Microwave Theory Tech.* **28** 1077; Kobayashi Y and Tomohiro S 1993 *IEEE Trans. Microwave Theory Tech.* **41** 2198

[146] Luiten A N, Mann A G and Blair D G 1996 *J. Phys. D: Appl. Phys.* **29** 2082; Shelby R, Fontanella J and Andeen C 1980 *J. Phys. Chem. Solids* **41** 69

[147] Ceremuga J, Barton M, Miranda F *Supercond. Sci. Technol.* 1994 **7** 855

[148] Silva E, Lanucara M and Marcon R 1996 *Supercond. Sci. Technol.* **9** 934

[149] Pompeo N, Marcon R and Silva In *Applied Superconductivity 2003 - Proc. of VI European Conference on Applied Superconductivity, Sorrento, Italy, 14-18 September 2003*; Editors: Andreone A, Pepe G P, Cristiano R, Masullo G; 2004 Institute of Physics, Conference Series **181** 2629

[150] Sridhar S 1988 *J. Appl. Phys.* **63** 159

[151] Hartemann P 1992 *IEEE Trans. Appl. Supercond* **2** 228

[152] Silva E, Lanucara M and Marcon R 1997 *Physica C* **276** 84

[153] Beeli P 2000 *Physica C* **333** 65 and references therein

[154] Lauder A, Myers K E and Face D W 1998 *Adv. Mater.* **10** 1249; Kroger H, Hilbert C, Gibson D A, Ghoshal U and Smith L N 1989 *Proc. IEEE* **77** 1287; Qiao J and Yang C Y 1995 *Mater. Sci. Eng.* **R14** 157; Méchin L, Huot G and Bloyet D 2004 *Appl. Phys. Lett.* **85** 3154

[155] Salje EKH, Wruck B and Marais S 1991 *Ferroelectrics* **124** 185

[156] Jaekel C, Kyas G, Roskos H G, Kurz H, Kabius B, Meertens D, Prusseit W and Utz B 1996 *J. Appl. Phys.* **80** 3488

[157] Pompeo N, Marcon R, Méchin L and Silva E 2005 *Supercond. Sci. Technol.* **18** 531

[158] Morin J and Maita J P 1954 *Phys. Rev.* **96** 28

[159] Méchin L, Villégier J C, Rolland G, Laugier F 1996 *Physica C* **269** 124

[160] Silva E, Marcon R, Sarti S, Fastampa R, Giura M, Boffa M and Cucolo A M 2004 *Eur. J. Phys. B* **37** 277

[161] Neri D, Marcon R, Rogai R, Silva E, Fastampa R, Giura M, Sarti S, Cucolo A M, Beneduce C, Bobba F, Boffa M and Cucolo MC 2000 *Physica C* **341-348** 2679

[162] Beneduce C, Bobba F, Boffa M, Cucolo A M, Cucolo M C, Andreone A, Aruta C, Iavarone M, Palomba F, Pica G, Salluzzo M and Vaglio R 1999 *Int. J. Mod. Phys. B* **13** 1333

[163] Camerlingo C, Lissitski M P, Russo M and Salvato M presented at *INFMeeting June 2002 Bari Italy* (unpublished)

[164] Boffa M A, Bobba F, Cucolo A M and Monaco R 2003 *Int. J. Mod. Phys. B* **17** 768

[165] Boffa M, Cucolo M C, Monaco R and Cucolo A M 2003 *Physica C* **384** 419

[166] Boffa M, Cucolo A M, private communication

[167] Silva E, Lanucara M and Marcon R 1996 *Supercond. Sci. Technol.* **9** 934

[168] Xinw W, Heinrich B, ZHou H, Fife A and Cragg A R 1994 *J. Appl. Phys.* **76** 4244

[169] Matsuda Y, Shibata A, Izawa K, Ikuta H, Hasegawa M and Kato Y *Phys. Rev. B* 2002 **66** 014527

[170] M. Ausloos 1999 *Supercond. Sci. Technol.* **12** 11

[171] Nagashima T, Hangyo M, Nakashima S, Murakami Y In *Adv. in Superconductivity VI*; Editors: Fujita T, Shiohara Y; Springer-Verlag, Tokyo, Japan, 1994; pp 209-212.

[172] Srikanth H, Willemsen B A, Jacobs T, Sridhar S, Erb A, Walker E and Flükiger R 1997 *Phys. Rev. B* **55** R14733; Srikanth H, Zhai Z, Sridhar S, Erb A and Walker E 1998 *Phys. Rev. B* **57** 7986

[173] Bonn D A, Dosanjh P, Liang R and Hardy W N 1992 *Phys. Rev. Lett.* **68** 2390

[174] Silva E 2002 *Eur. Phys. J. B* **27** 497

[175] Silva E, Pompeo N, Sarti S, Amabile C, chapter *Vortex state microwave response in superconducting cuprates and MgB_2*, to be published by Nova Publishers

[176] Marcon R, Fastampa R, Giura M and Matacotta 1989 *Phys. Rev. B* **39** 2796; Giura M, Marcon R and Fastampa R 1989 *Phys. Rev. B* **40** 4437

[177] Wosik J, Kranenburg R A, Wolfe J C, Selvamanickam V and Salama K 1991 *J. Appl. Phys.* **69** 874

[178] Silva E in *Superconducting Materials: Advances in Technology and Applications*; Editors: Tampieri A and Celotti G; World Scientific, 2000, pp 279-306

[179] Hallbritter J 1995 *J. Supercond.* **8** 691; Hallbritter J 1999 *Supercond. Sci. Technol.* **12** 883; Hallbritter J 2001 *J. Supercond.* **14** 9;

[180] Gaganidze E, Heidenger R, Hallbritter J, Shevcun A, Trunin M, Schneidewind H 2003 *J. Appl. Phys.* **93** 4049

[181] Gurevich A 2002 *Phys. Rev. B* **65** 214531

[182] Gurevich A, Rzchowski M S, Daniels G, Patnaik S, Hinaus B M, Carillo F, Tafuri F and Larbalestier D C 2002 *Phys. Rev. Lett.* **88** 097001

[183] Gurevich A 1992 *Phys. Rev. B* **48** 12857

[184] Ammor L, Soret J C, Smina A, Ta Phuoc V, Ruyter A, Wahl A, Martinie B, Lecomte J and Simon Ch *Physica C* 1997 **282** 1983

[185] Glazman K I and Koshelev A E 1991 *Phys. Rev. B* **43** 2835

[186] Poole C P Jr *Electron Spin Resonance*, Interscience Publishers, New York, 1967

[187] Staelin D H, Morgenthaler A W, Kong J A 1994 *Electromagnetic waves*, Prentice Hall International Editions

[188] Kobayashi Y, Aoki Y and Kabe Y 1985 *IEEE Trans. Microwave Theory Tech.* **MTT-33** 1361

[189] Kobayashi Y and Senju T 1993 *IEEE Trans. Microwave Theory Tech.* **41** 2198

[190] Likharev K K *Rev. Mod. Phys.* 1979 **51** 101

List of Publications

1. Pompeo N, Marcon R and Silva E 2004 *Applied Superconductivity 2003 - Proc. of VI European Conference on Applied Superconductivity, Sorrento, Italy, 14-18 September 2003 - ed. by A.Andreone, G.P.Pepe, R.Cristiano and G.Masullo - IOP Conference Series* **181** 2629 "Effective surface resistance of YBCO/Si structures"

2. Silva E, Marcon R, Muzzi L, Pompeo N, Amabile C, Fastampa R, Giura M, Sarti S, Boffa M, Cucolo M C and Cucolo A M 2004 *Applied Superconductivity 2003 - Proc. of VI European Conference on Applied Superconductivity, Sorrento, Italy, 14-18 September 2003 - ed. by A.Andreone, G.P.Pepe, R.Cristiano and G.Masullo - IOP Conference Series* **181** 2622 "Field, temperature and frequency dependence of the microwave resistivity in REBa2Cu3O7 thin films"

3. Pompeo N, Marcon R, Muzzi L, Silva E, Portesi C, Gandini C, Monticone E, Rajteri M and Sarti S 2004 *Applied Superconductivity 2003 - Proc. of VI European Conference on Applied Superconductivity, Sorrento, Italy, 14-18 September 2003 - ed. by A.Andreone, G.P.Pepe, R.Cristiano and G.Masullo - IOP Conference Series* **181** 1339 "Microwave fluctuation conductivity of MgB2 thin films on sapphire and SiN substrates"

4. Silva E, Marcon R, Muzzi L, Pompeo N, Fastampa R, Giura M, Sarti S and Boffa M 2004 *Physica C* **404** 350-353 "Mixed-state microwave resistivity in RE-BaCuO film"

5. Pompeo N, Marcon R, Méchin L and Silva E 2005 *Supercond. Sci. Technol.* **18** 531 "Effective surface impedance of YBaCuO films on Silicon substrates"

6. Pompeo N, Muzzi L, Sarti S, Marcon R, Fastampa R, Giura M, Boffa M, Cucolo M C, Cucolo A M, Camerlingo C and Silva E 2005 *J. Phys. Chem. Solids* (doi:10.1016/j.jpcs.2005.10.014) "Mixed state microwave resistivity of cuprate superconductors"

7. Pompeo N, Marcon R and Silva E "Substrate contribution to the surface impedance of HTS films on Si", accepted for the publication on *J. Supercond.*

8. Silva E, Pompeo N, Marcon R, Fastampa R, Giura M, Sarti S and Camerlingo C "Mixed-state microwave response in superconducting cuprates", accepted for the publication on *J. Supercond.*

9. Silva E, Pompeo N, Muzzi L, Marcon R, S. Sarti, M. Boffa, A. M. Cucolo, "Field dependence of the microwave resistivity in SmBa2Cu3O7 thin films", submitted to *Phys. Rev. B* , *cond-mat/* 0405324 v3 (19/05/2004)

10. Silva E, Pompeo N, Sarti S and Amabile C "Vortex state microwave response in superconducting cuprates and MgB2", chapter of the book "New Topics in Superconductivity Research" - ed. by Barry P. Martins, to be published by *Nova Publishers*